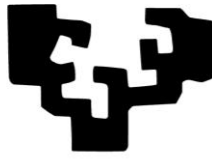eman ta zabal zazu

Universidad del País Vasco
Euskal Herriko Unibertsitatea

Applications of Laser-Spot Thermography to thermal diffusivity and crack measurements on static and moving samples

by

Mateu Colom Serra

Supervisors: Agustín Salazar Hernández and María Aranzazu Mendioroz Astigarraga

Thesis presented for the degree of

Doctor in Physics

At the Department of Applied Physics, Faculty of Engineering, UPV/EHU

Bilbao, May 2021

Acknowledgements

Me gustaría expresar mi más sincero agradecimiento a todas las personas que han contribuido de un modo u otro a la realización de esta tesis.

A mis dos directores, Dr. Agustín Salazar y Dra. Arantza Mendioroz, por su dedicación, esfuerzo y paciencia, que han sido de gran ayuda para llevar a cabo este trabajo, y sobre todo por sus ánimos, que fueron fuente de motivación en estos tiempos de pandemia. ¡Muchas gracias! También quiero agradecer la colaboración del Dr. Javier Rodríguez Aseguinolaza por su contribución y su ayuda en los códigos de elementos finitos, como también la colaboración con el departamento de Ingeniería Mecánica.

Además, agradezco al Gobierno Vasco y a la UPV/EHU el contrato predoctoral concedido sin el cual esta tesis no hubiera sido posible.

A toda la gente del departamento de Física Aplicada, sobre todo al Dr. Alberto Oleaga, siempre dispuesto a ofrecer su ayuda, y a Ibon, Asun y José Félix, por su colaboración, apoyo y ayuda en las prácticas de laboratorio de estudiantes. Al resto del departamento, y en especial a los compis de la hora de comer: Asier, Naiara, Peio, Itziar, Hao, Jorge, Iñaki… por hacer el día a día más ameno. También a mi parcerito Adrián, por todas las horas de laboratorio que compartimos, y a Laura por su ayuda los primeros meses.

A mi compañero de despacho y buen amigo Aritz, con quien más horas he pasado frente a frente durante estos años. Eskerrik asko!

A mis amigas y amigos de Euskadi de la cuadrilla KatxiKlan. Ha sido un auténtico placer haberos conocido, en especial a la Ru, a Iratxe, y al resto… no quiero dejarme a nadie! Eskerrik asko denoi!

Als amics i amigues catalans: als quatre amors de Can Pixa, a la colla de Girona party jordan, als free's, i a tota la resta de gent de Tona i voltants. Cada visita i cada tornada durant les vacances ha set vital i imprescindible. Gràcies!

I ja per acabar, només em queda el millor dels agraïments a la meva família: pare, mare, Aleix, gràcies per tot, per ser-hi, tot i la distància.

Abstract

In recent years there has been a growing interest in non-destructive and non-invasive methods to study the physical properties of materials and to detect and evaluate hidden defects. Photothermal techniques have proven to be suitable for studying the propagation of heat in materials, and, specifically, infrared thermography has been applied in science and engineering environments since the development of infrared cameras. Currently, it is considered an effective and efficient tool for non-destructive testing of materials, and it is a good alternative for tests that use ultrasounds, eddy currents or dye penetrants, for example.

This thesis is focused on the development of infrared thermography applications for the characterization of material's thermal properties and defects. In particular, the laser-spot technique (focused laser illumination) has been used to measure the thermal diffusivity of materials both at rest and in motion, in a quick and precise manner, as well as to quantify cracks, both calibrated and real fissures, determining different parameters, namely, the inclination with respect to the surface, the width or the depth.

The first chapter introduces the fundamentals of heat transfer, and describes both the mechanisms of heat flow and the heat diffusion equation, which governs the dynamics of heat transfer in a body in non-stationary phenomena. In addition, infrared radiation and how it is captured by an infrared camera are described.

The second chapter describes the experimental setups developed in this work, detailing the characteristics of the camera, the optics of the system and the type of illumination. The particular cases of the sample at rest or in motion are specified, as well as the differentiation between continuous and modulated laser illumination.

The third chapter includes three procedures for determining in-plane thermal diffusivity. First, continuous illumination is used to measure the thermal diffusivity of samples at rest. It is demonstrated that the instruments used (laser and camera) can be low cost equipments, and, furthermore, it is only necessary to apply a simple processing on the acquired data to obtain the diffusivity with precision and accuracy similar to more sophisticated lock-in thermography. Diffusivity has also been measured in moving samples, which is a common situation in industrial processes, using both continuous and modulated illumination. Regarding the continuous excitation case, it has been applied to anisotropic samples, proving the ability of discerning its principal axes when the orientation is unknown.

Finally, the fourth chapter includes the characterization of cracks using modulated illumination, where lock-in post processing is applied for the significantly reduction of noise. In the first place, a procedure already studied in our research group to measure the width of infinite vertical cracks is adapted to determine the thermal conductivity of fluids filling in the crack separation. On the other hand, finite element methods are applied to determine the width and angle of inclination in tilted artificial cracks of infinite depth. In addition, these same methods are also applied to determine the width and depth of real vertical fatigue cracks of finite penetration, originated in a real metallic part.

Resumen

En los últimos años ha habido un creciente interés en los métodos no destructivos y no invasivos para estudiar propiedades físicas de materiales y para detectar y evaluar defectos presentes en ellos. Se ha demostrado que las técnicas fototérmicas son métodos de gran utilidad para estudiar la propagación del calor en materiales y, en concreto, la termografía infrarroja se ha aplicado en diferentes ámbitos de la ciencia y la ingeniería desde la aparición de las cámaras infrarrojas. En la actualidad, es considerada como una herramienta efectiva y eficiente para ensayos no destructivos en materiales, y es una buena alternativa para los ensayos que usan ultrasonidos, corrientes inducidas o líquidos penetrantes, por ejemplo.

Esta tesis recoge el trabajo desarrollado basado en la aplicación de la termografía infrarroja para la caracterización de propiedades térmicas de materiales y defectos. En particular, se ha usado la técnica de "laser-spot" (iluminación con láser puntual o enfocado) para medir la difusividad térmica de materiales tanto en estático como en movimiento de forma rápida y precisa, así como también para cuantificar grietas, tanto grietas artificiales calibradas como fisuras reales de forma general, determinando su inclinación respecto la superficie, su anchura o su profundidad.

En el primer capítulo se introducen los fundamentos de la transferencia de calor, y se describen tanto los mecanismos de flujo de calor como la ecuación de difusión de calor, que gobierna la dinámica de transferencia de calor en un cuerpo en fenómenos no estacionarios. Además, se describe la radiación infrarroja y cómo es captada por una cámara infrarroja.

En el segundo capítulo se describe el montaje experimental usado, detallando las características de la cámara, la óptica del sistema y el tipo de iluminación. Se especifican los casos particulares de muestra en reposo o en movimiento, y también la diferenciación entre iluminación láser continua y modulada.

En el tercer capítulo se engloban tres procedimientos para determinar la difusividad térmica *en el plano*. En primer lugar, se utiliza iluminación continua para medir la difusividad térmica de muestras en reposo. Se demuestra que los dispositivos utilizados (láser y cámara) pueden ser de bajo coste, y, además, sólo es necesario aplicar un simple procesado en los datos adquiridos para obtener la difusividad, con una precisión similar a la que se consigue utilizando técnicas más sofisticadas como la termografía "lock-in" También se ha medido la difusividad en muestras en movimiento, situación habitual en cadenas de montaje de procesos industriales, utilizando tanto iluminación continua como modulada.

Finalmente, el cuarto capítulo engloba la caracterización de grietas utilizando iluminación modulada, aplicando procesado "lock-in" para reducir significativamente el ruido. En primer lugar, se hace uso de un procedimiento ya estudiado en nuestro grupo de investigación para la anchura de grietas infinitas, adaptándolo para ser utilizado como método de medida de la conductividad térmica de fluidos que llenan la separación de grieta. Por otro lado, se aplican métodos de elementos finitos para determinar la anchura y ángulo de inclinación con la superficie en grietas artificiales de profundidad infinita. Además, estos mismos métodos también se aplican para determinar la anchura y profundidad de grietas reales con penetración finita, presentes en piezas metálicas sometidas a fatiga.

Contents

1. Introduction

In this first chapter, the foundations of this thesis will be settled. First of all, we will begin introducing the concept of infrared radiation. Next, the issue of thermal imaging will be addressed, explaining how infrared radiation is captured by a thermal camera. Finally, in Section 1.3, we will present the theoretical background of heat conduction and heat transfer.

1.1. Infrared radiation

Infrared radiation (IR) is the electromagnetic radiation in the wavelength region longer than visible light wavelengths, and it ranges from 0.75 to 1000 μm. The first time when it was showed that the electromagnetic spectrum is wider than the visible light was in 1800. The astronomer William Herschel proposed an experiment which consisted in measuring the temperature of different colors to prove that there exist radiation invisible to the naked eye [1]. In order to do this, he set up an experiment in which the Sun's light was passed through a glass prism to split it into the different wavelength components, forming a spectrum on the table with the rainbow's colors as thought at that time. Then, he placed thermometers to measure the temperature of various colors in the split spectrum, and found that the temperature would increase from blue to red, so he decided to place another thermometer beyond the red color, where apparently no sunlight fell on, but unexpectedly the measured temperature was higher than the obtained for the visible spectrum. Therefore, he concluded that there must be another type of light beyond the red, which is invisible to the naked eye. This light was named "invisible thermo-metrical spectrum", and now it is known as the infrared radiation.

The electromagnetic radiation emitted by a body as a consequence of its temperature T is called thermal radiation. In thermal equilibrium, this radiation covers the whole electromagnetic spectrum and the energy emitted at a wavelength per unit time and per unit area, $W(\lambda, T)$, is a universal function for black bodies.

A black body is an object which completely absorbs radiation from any direction or wavelength, and is able to emit it in the same way until reaching the thermodynamic equilibrium. Thus, the intensity of the emitted radiation depends on the black body temperature and on the wavelength, being the same for all directions.

The power per unit area at a given wavelength emitted by a black body, the so-called spectral radiance, is given by Planck's law:

$$W(\lambda, T) = \frac{2hc^2}{\lambda^5}\left(\frac{1}{e^{\frac{hc}{\lambda k_B T}} - 1}\right), \qquad (1.1)$$

where $h = 6.63\times10^{-34}$ Ws^2 is the Planck's constant, $c = 3\times10^8$ m/s is the speed of light in vacuum and $k_B = 1.38\times10^{-23}$ JK^{-1} is the Boltzmann constant, λ is the wavelength in m and the temperature T is measured in K.

In Figure 1.1 the spectral radiance of a black body at different temperatures is shown. As Planck's Law states, the infrared radiation is not uniformly distributed, but it shows a maximum for a specific wavelength and then it is reduced at both sides of the wavelength spectrum. A logarithm representation in both axes has been chosen for clarity in the presentation, also the visible range of the electromagnetic spectrum is indicated.
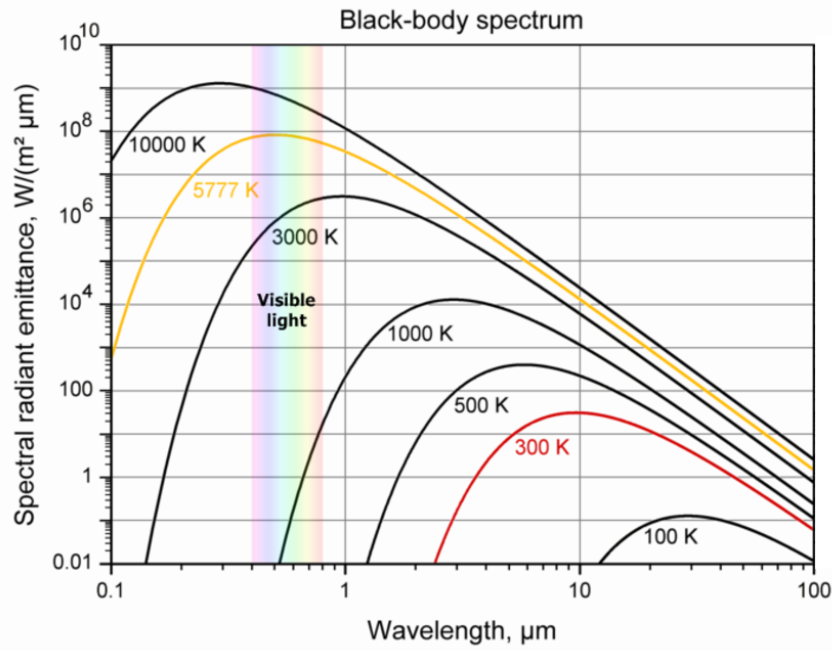
Figure 1.1: Spectral radiance of a black body at different temperatures.

In certain situations, Planck's Law can be simplified. Wien's Law is the approximation of Planck's Law for short wavelengths, $\lambda T \ll \frac{hc}{k_B}$, so that the spectral radiance becomes:

$$W(\lambda, T) = \frac{2hc^2}{\lambda^5} \, e^{-\frac{hc}{\lambda k_B T}} .$$ (1.2)

On the other hand, Planck's law retrieves the Rayleigh-Jeans law for long wavelengths $\lambda T \gg \frac{hc}{k_B}$:

$$W(\lambda, T) = \frac{2hck_B T}{\lambda^4} .$$ (1.3)

It becomes useful determining the λ_{max}, for which the radiance of a black body at a temperature T reaches a maximum. Maximizing Planck's Law with respect to the wavelength, Wien's Displacement Law is obtained:

$$\lambda_{max} = \frac{2898 \ \mu m \cdot K}{T} .$$ (1.4)

Moreover, integrating Planck's law over all wavelengths ranging from zero to infinity, the Stefan-Boltzmann's Law of radiation for black bodies can be deduced, which gives the total power emitted per unit area by a black body at a given temperature:

$$W(T) = \sigma_0 T^4 \,, \tag{1.5}$$

where $\sigma_0 = 5.67 \times 10^{-8}$ Wm^{-2}K^{-4} is the Stefan-Boltzmann constant.

The theory of the blackbody radiation is very important, in particular, for thermography science, since these equations represent the physical principles that relate infrared thermography to the measurement of a real object's surface temperature.

Even when real bodies do not completely follow Planck's radiation law, their radiative properties are described in relation with the corresponding ones of a perfect blackbody. In this way, let W be the total power emitted by an object surface at a given temperature, and W_b the total power emitted by a blackbody surface at the same temperature. The ratio between these two quantities is called the total emissivity ε:

$$\varepsilon = \frac{W}{W_b} \,, \tag{1.6}$$

which is a measure of the efficiency of a real body to emit thermal radiation with respect to a perfect blackbody at the same temperature. Thus, the emissivity is a dimensionless value between 0 and 1.

As we may note, in Infrared Thermography (IRT), where a detector records the radiation emitted by the sample surface to obtain the temperature field of the sample, the uncertainty about the emissivity of the sample could be problematic. However, for small changes of temperature, which is a common case in an IRT experiment, the emissivity value can be considered constant. Besides, in the IRT experiments carried out in this work, the information of interest is the relative variation of temperature, regardless of the absolute temperature values.

1.2.   Thermal imaging

Infrared thermography is a non-destructive testing (NDT) technique, which was introduced a few decades ago and keeps attracting the attention of both scientific and industrial environments, because of its versatility for diagnostics, monitoring, measurement of thermal maps on the surface of bodies and because in general it is a non-invasive technique [2,3].

Practical applications involving infrared technology date from the XIX century. However, it was not until the 1930s when many ideas of IR applications started to emerge, like its use for the detection of icebergs, monitoring forest fires, analysis of hot rolled metals, etc. In 1937, Pierre Vernotte pioneered the idea of the measurement of thermal properties of materials from single-sided measurements [4] and he also introduced the notion of a thermal transport property, which is currently known as thermal effusivity.

However, it was not until 1958 when Hardy achieved the first single-sided and non-contact thermal characterization using pulsed infrared radiometry [5]. That experiment consisted in measuring the thermal effusivity of the living skin of the forehead of a person. This work, along with that of Cowan using modulated heating radiometry [6] as well as that of Parker, of the non-contact, double sided, rear-face measurement of thermal diffusivity by active IR pulsed radiometry [7] are considered as the milestone works paving the way for active infrared thermography for non-destructive testing and evaluation (NDT&E) [8].

In the 1960s, the interest in infrared thermography for NDT&E grew because of the space race and IRT attracted the attention of researchers for the inspection of aerospace materials. However, by the end of the 1970s, the NDT studies performed with IRT were practically qualitative and hence IRT was hardly competitive with other nondestructive tests. Nevertheless, a new level on the understanding of IRT has been achieved after the wider use of heat conduction theory, the introduction of inverse problems for NDT&E, the implementation of efficient numerical algorithms, as well as extensions of IRT to several fields such as, civil engineering, medicine, maintenance, environment, thermo-fluid dynamics, conservation of cultural heritage, among many others [9]. A typical

classification of IRT is shown in Figure 1.3. Notice the possible configurations available for this kind of imaging. In this work, however, we have studied just a few of all the possible combinations for active thermography, which are the ones colored in green.
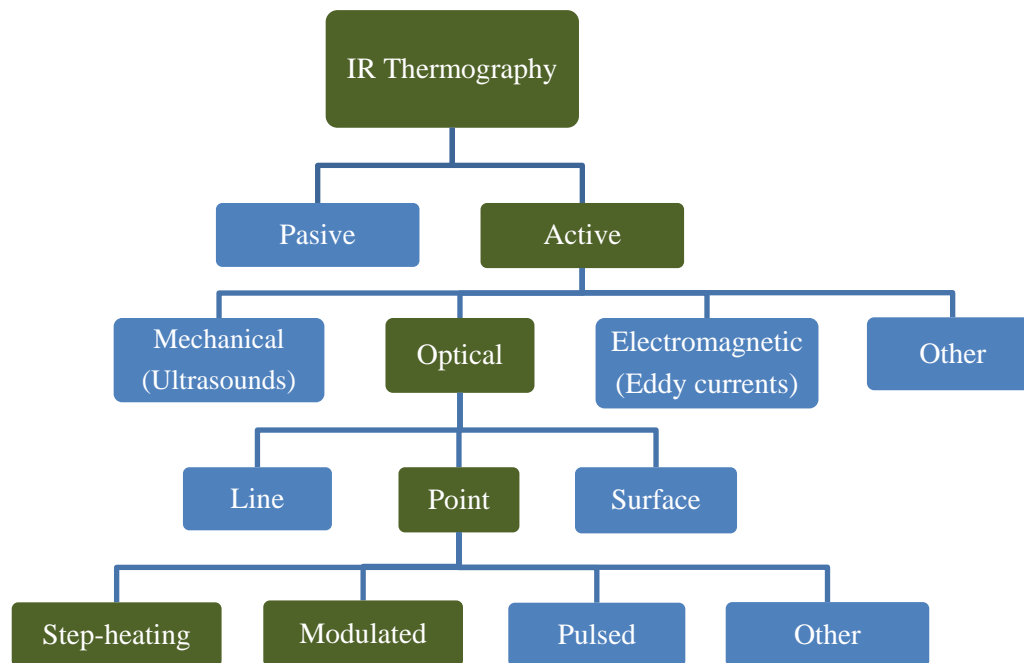
Figure 1.2: Schematic classification of infrared thermography.

IRT can be either passive or active. Passive stands for the simple recording of the emitted infrared radiation, without previous on-purpose artificial excitation of the object to be examined. For its simplicity, it was the first to arise, with applications in civil engineering (building maintenance), military field (night vision) or medicine (body temperature mapping), among others. Active Thermography, on the other hand, studies previously excited samples, to retrieve information out of the temperature variations.

Active IRT requires an external source of energy to induce temperature differences. A wide variety of energy sources are available and can be divided into optical, mechanical, electromagnetic, or other excitation forms. In optical excitation, the energy is delivered to the surface by means of optical devices such as photographic flashes, halogen lamps or lasers, which is our case. In mechanical excitation, the energy is injected into the specimen by means of mechanical oscillations, using for example an

ultrasonic transducer, which generally requires contact with the part. In electromagnetic excitation, the energy is delivered by electromagnetic pulses that excite eddy currents in electrically conductive materials. The eddy currents generate heat by resistive losses. Moreover, there exist more sources, like hot air convection or microwave radiation, among others.

Focusing on optical excitation, the spatial distribution of the excitation can be punctual, when the illumination is focused on a small region; linear, when the excitation source has the shape of a straight line; or flat, when the intensity is constant in a plane at a given time.

Finally, different temporal scheme of excitation can be applied. The most popular are pulsed and modulated illuminations, although other temporal configurations such as step-heating (continuous) or coded excitation are also applied. Pulsed excitation consists of heating briefly the sample and then recording the temperature evolution. In modulated illumination, samples are excited by means of an intensity modulated light beam, so that the periodic energy deposition on the material surface generates thermal waves inside the samples and the resulting oscillating temperature field is recorded. In step-heating illumination, the delivered energy is constant through time. In coded excitation, the source is modulated with a non-constant frequency (modulated frequency) [10-12].

Essentially, IRT consists in sensing the IR emission of a body and using this information to build a visible image of its surface temperature field. Infrared camera enables this kind of imaging. The principal components of an IR camera are: the optics (lens), the IR detectors, a cooling system for the detectors (in the case of photon-detector based cameras), and electronic and software management for the images.

We present below a brief description of some concepts in IR thermography to be taken into account for accurate measurements with an IR camera. In Chapter 2, the specifications of the IR camera used in the experiments will be addressed.

Atmospheric windows

It is well known that the atmosphere attenuates the radiation due to absorption by the gases, and also due to Rayleigh scattering with suspended particles. This attenuation depends on the wavelength of the radiation [13,14]. It is worth noting that Infrared Thermography is a non-contact technique. In that sense, one should consider that infrared radiation emitted from the sample surface must travel to the detector through the atmosphere, and in that way, a fraction of the radiation could be absorbed by the atmosphere. Moreover, thermal radiation from objects in the room could contribute to the radiation reaching the detector, causing the detector to observe an apparent temperature of the sample different from the real one.

It is true that remote sensing devices are equipped with detector materials coincident with the so-called "atmospheric windows". Infrared radiation corresponds to vibrational and rotational energy of molecules, so the ones composing the atmosphere are able to absorb part of the infrared radiation from the sample in the way to the detector.

Typically, three atmospheric windows, i.e., the range of wavelengths with high transmittance, are used in IR cameras: covering from 1 to about 2.5 μm is the shortwave (SW) window; from 3 to about 5.6 μm, the mid-wave (MW) window and from 8 to about 14 μm is the long-wave (LW) window (see Figure 1.3). These LW windows are particularly useful where strong atmospheric attenuation is involved, since atmosphere behaves as a high-pass filter for wavelengths larger than 7.5 μm. On the other hand, mid-wave windows (3 - 5 μm) in combination with highly sensitive detectors have proven to be very useful for research, while short-wave windows are commonly used for military applications [15].
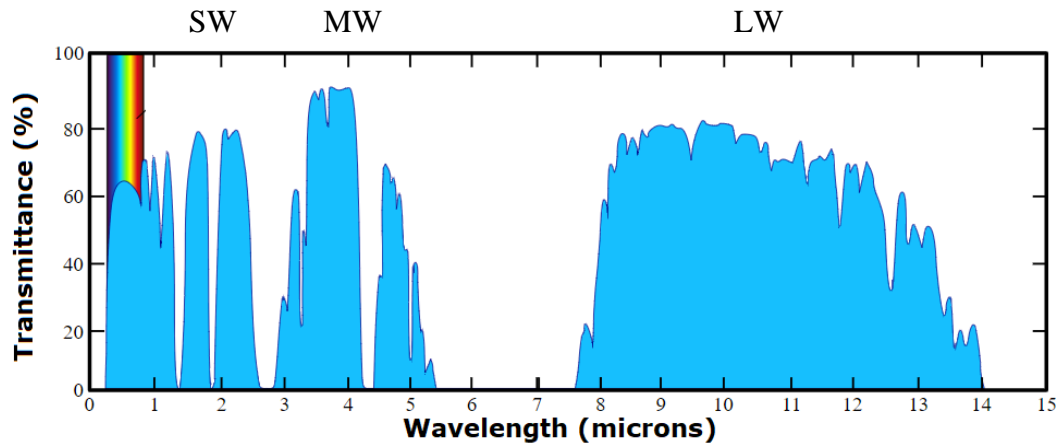
Figure 1.3: Transmittance IR spectrum of the atmosphere.

In addition to this good transmission in the detection wavelength, it is worth remembering that in some applications, as the work developed in this thesis, absolute temperatures were not needed, but only changes of temperatures. Hence, it is not a problem that the atmosphere absorbs some of the radiation.

IR detectors

IR detectors can be classified as: single detectors, linear and focal plane array (FPA) detectors, based on the detector's construction in an IR camera. Nowadays, IR cameras are mostly provided with FPA detectors, which consist of a two-dimensional pixel matrix, being each pixel a detector of micrometer size. In this kind of cameras, there are no mechanical scanning devices, but the matrix looks at an object through the camera optics, as depicted in Figure 1.5. Moreover, in modern infrared systems, it is possible to record several hundreds of thermograms per second.

There are two kinds of commercial IR detectors used in modern IR cameras: microbolometer (thermal) detectors and intrinsic (photon) detectors.

Microbolometer type detectors are widely used in IR cameras because they do not require cooling (in general), which allows compact camera designs and consequently relatively low production costs. FPA detectors can be manufactured of metals or

semiconductor materials and they operate by the bolometer effect, i.e., the incident radiation changes the electrical resistance of the bulk material (bolometric detector). Microbolometers have a flat response curve as a function of wavelength. However, one of their main drawbacks consists in their relatively low detectivity, which is the main parameter characterizing normalized signal to noise performance of detectors, and they usually have slow response time.
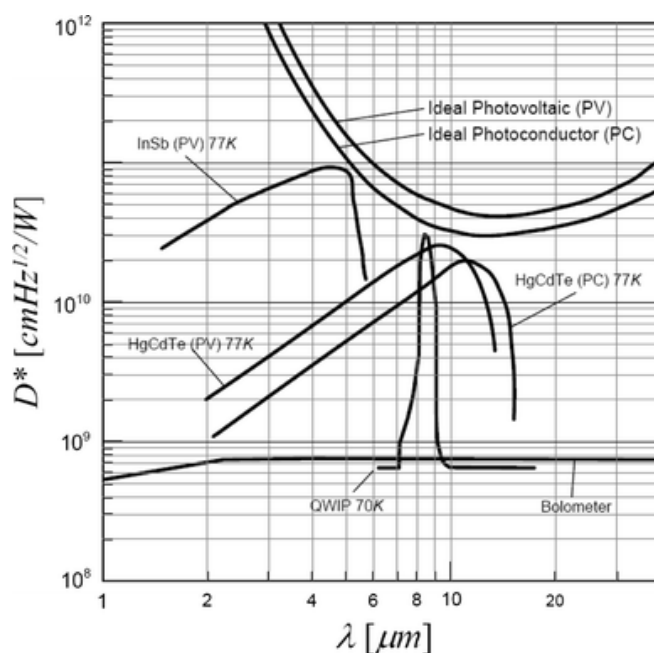
Figure 1.4: Detectivity (D*) curves for different detector materials. Bolometer detectivity is flat, while it features a strong dependence with wavelength for photon detectors.

Intrinsic detectors operate on the basis of an intrinsic photoconductive effect. When the materials these detectors are made of are at room temperature, there are some electrons in the conduction band, while most of them are in the valence band. However, this configuration cannot be useful for detection of IR radiation, because the electrons already present in the conduction band can carry an electrical current.

Nevertheless, when the material is cooled at a certain operating temperature (for instance, 173 K for InSb detectors), the thermal energy is low enough so that all the electrons are found in the valence band. Under this condition, if the material is exposed to IR radiation and the incident photons have enough energy, the electrons in the

valence band can be promoted to the conduction band. In this way, the material can carry a photocurrent which is proportional to the incident IR radiation. Therefore, it can be used as an IR detector as long as the incident photon energy (inverse wavelength) is sufficient to overcome the band gap energy ΔE.

The band gap energy is directly related to a certain cutoff wavelength: for detectors in SW or MW windows, the band gap is higher than for detectors in LW windows. Consequently, the operating temperatures are lower for LW detectors than for SW or MW ones [16].

It is important to remark that cooling this kind of detectors to cryogenic temperatures allow them to be very sensitive to the incident IR radiation. Furthermore, these detectors respond very quickly to temperature changes. Therefore, intrinsic detectors are quite good for studying fast transient thermal phenomena and they are used with great success in fast thermography. However, the detectivity must be taken into account when selecting a photon detector for certain application, since it has a strong dependence on wavelength, as it is shown in Figure 1.4.

Cooling methods

The output signal of a detector is so small that at ordinary temperatures it is masked by the thermal noise. In order to minimize the noise, photon detectors must be cooled. The method of cooling varies according to the operating temperature and the system's logistical requirements [17]. Most 8-14 μm detectors operate at about 77 K and can be cooled by liquid nitrogen. However, usually it is more convenient to use compressed air and a Joule-Thompson minicooler (Figure1.5a). Specially designed Joule-Thompson coolers using argon are suitable for ultra-fast cool-down.

The use of cooling engines has increased recently due to their efficiency, reliability and cost reduction, in particular the engines employing the Stirling cycle. A Stirling engine requires several minutes cool-down time. In this case, the Stirling motor removes the heat from the cold finger, cooling the detector attached to the cold side, as shown in Figure 1.5b. The removed heat is dissipated at the warm side. Even though this cooling method has low efficiency, it is enough for cooling the detector of an IR camera.

Both Joule-Thompson and engine-cooled detectors are housed in dewars into which the cooling device is inserted, as can be seen in Figure 1.5. The detector is located just behind an IR window. It is mounted in a vacuum chamber at the end of the inner wall of the dewar, and it is surrounded by a cooled radiation shield.

Many detectors in the 3–5-µm waveband are thermoelectrically cooled. In this case, detectors are usually mounted in a hermetic encapsulation with a base designed to make good contact with a heat sink.
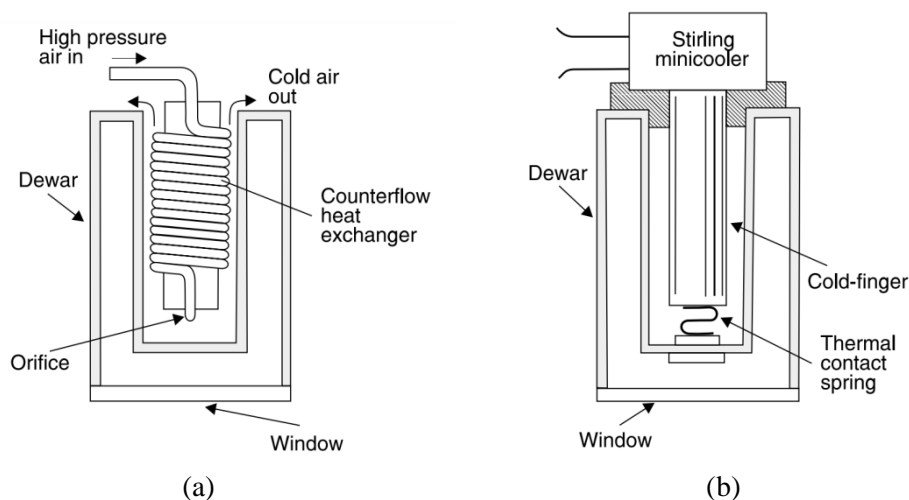
Figure 1.5: (a) Joule-Thompson cooler and (b) Stirling-cycle engine.

1.3.   Heat transfer and heat equation

The study of heat transfer in materials allows the possibility of measuring thermal properties (thermal diffusivity) and detecting and characterizing cracks. Heat transfer can be defined as energy in transit due to a temperature difference. This process always occurs from the hottest to the coldest region and stops when both reach an equilibrium temperature. Heat transfer can be classified in three different mechanisms: conduction, convection, and radiation [18]. Conduction is described by Fourier's law, convection by Newton's cooling law, and radiation by and Stefan-Boltzman's law.

Heat conduction

Heat can be transmitted through solids mainly by electrical carriers, by means of electrons and holes movement, and also due to the vibration of atoms and molecules in the crystalline network. The energy transfer occurs from the more energetic to the less energetic particles in a substance due to interactions between them. Conduction takes place in solids, liquids and gases and is usually the most important form of thermal transport within a solid or solid objects in thermal contact [19]. Fourier's Law governs the steady state heat conduction through the opposite surfaces of a sample [20]. Fourier's Law states that the heat flux density q (which is the heat flux per unit area) resulting from thermal conduction is proportional to the temperature gradient and opposite to it in sign:

$$\vec{q}_{cond} = -K\vec{\nabla}T \,, \tag{1.7}$$

where K is the thermal conductivity, it has units of $Wm^{-1}K^{-1}$, and it measures a material's ability to conduct heat. It is important to note that Fourier's law is applicable to non-time varying temperature gradients. For one-dimensional steady state conduction in extended samples of homogeneous and isotropic materials and small temperature gradients, Fourier's law can be integrated:

$$q_{cond} = -K\frac{dT}{dx} = -K\frac{T_2 - T_1}{x_2 - x_1} = -K\frac{\Delta T}{L} \tag{1.8}$$

where L is the distance between x_2 and x_1. Equation 1.8 can be rewritten as:

$$q_{cond} = -h_{cond}\Delta T = -\frac{\Delta T}{R_{th}}, \tag{1.9}$$

where $h_{cond} = K/L$ is the conduction heat transfer coefficient and $R_{th} = 1 \, / \, h_{cond}$ is defined as the thermal resistance.

Heat convection

Convection is the transfer of thermal energy between a surface and an adjacent moving liquid or gas. The fluid receives the thermal energy through contact with a hot body or surface through conduction, and then drags it away through the motion of the fluid. The faster the flow, the larger the convective heat transfer.

In 1701, Isaac Newton considered the convective process and suggested that the cooling would be proportional to the temperature difference between the body temperature, T_b, and the fluid temperature, T_∞:

$$Q \propto T_b - T_\infty \ . \tag{1.10}$$

This equation can be rewritten in terms of heat flux per unit area, $q = Q/A$, and introducing the parameter h_{conv}, known as the convection heat transfer coefficient.

$$q_{conv} = h_{conv}(T_b - T_\infty). \tag{1.11}$$

h_{conv} depends on the conditions found at the boundary layer between the hot surface or body and the fluid, and it is influenced by surface geometry and fluid properties.

Heat radiation

We start recalling Stefan-Boltzmann law (equation 1.5), together with the definition of emissivity (equation 1.5). The heat flux density emitted by a real surface is less than that emitted by a black body at the same temperature, and it is given by:

$$q_{rad} = \varepsilon \sigma T^4 \ . \tag{1.12}$$

Now, let us suppose a continuous energy exchange between a body of emissivity ε and temperature T_b, and an isothermal surface that surrounds it with temperature T_0. The radiation heat flow density is

$$q_{rad} = \varepsilon \sigma \left(T_b^4 - T_0^{\ 4} \right) . \tag{1.13}$$

Therefore, if small differences are assumed between the body and the medium, a Taylor series expansion around the temperature of the surrounding allows obtaining the following linear relationship:

$$q_{rad} = 4\varepsilon\sigma T_0^3 (T_b - T_0) = h_{rad}\Delta T , \qquad (1.14)$$

where $h_{rad} = 4\varepsilon\sigma T_0^3$ is defined as the radiation heat transfer coefficient. For $\varepsilon = 1$, it has typical values of 6 - 8 $Wm^{-2}K^{-1}$ ($h_{rad} = 6.12$ $Wm^{-2}K^{-1}$ for $T_0 = 300$ K, for instance).

Heat diffusion equation and thermal waves

Fourier's law only describes stationary heat conduction phenomena, so in order to describe the temperature depending on both space and the time coordinates it must be combined with the Law of conservation of energy leading to the so-called heat diffusion equation. Therefore, considering a homogeneous and isotropic medium, the heat diffusion equation [21,22] can be written as:

$$\nabla^2 T(\vec{r}, t) - \frac{1}{D} \frac{\partial T(\vec{r}, t)}{\partial t} = - \frac{Q(\vec{r}, t)}{K} . \qquad (1.15)$$

where Q is the rate of energy generation per unit volume, and D is the thermal diffusivity, which is defined as the rate of heat propagation through the body. The thermal diffusivity can be expressed in terms of the thermal conductivity, the material density and its specific heat ($D = K/\rho c$), and it has units of m^2s^{-1}.

If the source of the heating is periodically modulated with frequency f (and $\omega = 2\pi f$), which is a situation widely used in this thesis, then:

$$Q(\vec{r}, t) = \frac{Q_0(\vec{r})}{2} \left(1 + e^{i\omega t}\right) . \qquad (1.16)$$

The temperature field in the sample after reaching the steady state is the result of the following contributions: the ambient temperature T_{amb}, a stationary heating of the sample T_{dc} and a periodically varying component $T_{ac.}$

$$T(\vec{r}, t) = T_{amb} + T_{dc}(\vec{r}) + T_{ac}(\vec{r}, t). \tag{1.17}$$

The time dependent component will show the same time dependence as the source:

$$T_{ac}(\vec{r}, t) = T_{ac}(\vec{r})e^{i\omega t} \tag{1.18}$$

If the expression of the temperature in equation 1.18 is substituted into equation 1.15, two equations are obtained: a stationary heating component and the time dependent contribution, which is the one of our interest:

$$\nabla^2 T_{ac}(\vec{r}, t) - \frac{1}{D}\frac{\partial T_{ac}(\vec{r}, t)}{\partial t} = -\frac{Q_0(\vec{r})e^{i\omega t}}{2K}. \tag{1.19}$$

Equation 1.19 can be simplified, applying the derivative with respect to t to the second term so the exponential term $e^{i\omega t}$ can be omitted, obtaining a spatial dependence equation:

$$\nabla^2 T_{ac}(\vec{r}) - \sigma^2\, T_{ac}(\vec{r}) = -\frac{Q_0(\vec{r})}{2K}, \tag{1.20}$$

where

$$\sigma = \sqrt{\frac{i\omega}{D}}. \tag{1.21}$$

For the sake of simplicity, from now on T_{ac} will be named *temperature*. We will start considering a simple case, with an in-depth semi-infinite material excited by flat illumination, and then we will move to the focused illumination case, the beam geometry used in this work. We will consider that the material is opaque to the excitation wavelength and to infrared.

Using flat illumination, the heated surface is taken to occupy the *x-y* plane at *z* = 0 (see Figure1.6), so the temperature distribution within the solid (*z* < 0) can be obtained by solving a one-dimensional heat diffusion equation in *z* and *t*.
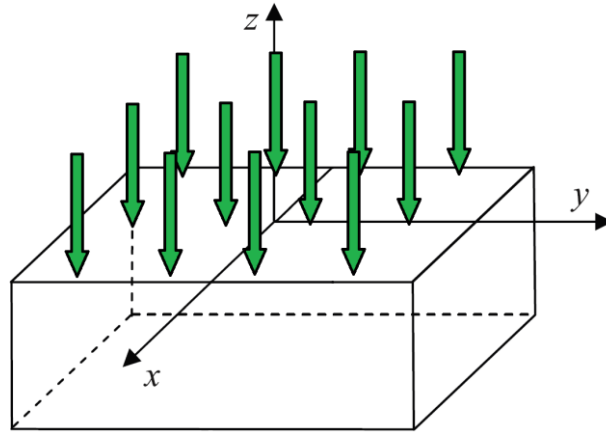
Figure 1.6: Scheme of a semi-infinite sample illuminated by a plane light beam.

In the situation where there is no internal heat generation in the material, $Q = 0$, and equation (1.20) can be written as a homogeneous Helmholtz equation:

$$\frac{d^2 T_{ac}(z)}{dz^2} - \sigma^2 \, T_{ac}(z) = 0 \,. \tag{1.22}$$

The general solution for the spatial dependence of the temperature (equation 1.22), may be written as

$$T_{ac}(z) = Ae^{\sigma z} + Be^{-\sigma z}. \tag{1.23}$$

The heat diffusion equation is subjected to the boundary condition. Neglecting heat losses at the sample surface by convection and radiation, and considering the periodic thermal energy applied to the surface, the boundary condition writes:

$$-K \frac{dT_{ac}}{dz}\bigg|_{z=0} = \frac{\eta I_0}{2} \tag{1.24}$$

where η is the fraction of intensity absorbed by the sample and I_0 is the intensity of the plane beam.

In the current case of a semi-infinite material, constant B is zero, as the temperature would tend to infinity and it has no physical meaning. The constant A is evaluated by applying the flux continuity boundary condition at the sample surface (equation 1.24),

$$-K\frac{dT_{ac}(z)}{dz}\bigg|_{z=0} = K\sigma A e^{\sigma z}\big|_{z=0} = K\sigma A = \frac{\eta I_0}{2}, \qquad (1.25)$$

obtaining $A = \frac{I_0}{2K\sigma}$. Therefore, the full solution is written as:

$$T_{ac}(z,t) = \frac{\eta I_0}{2K\sigma}e^{-\sigma z}e^{i\omega t}, \qquad \text{or}$$

$$T_{ac}(z,t) = \frac{\eta I_0}{2\sqrt{\rho c K\omega}}e^{-\frac{z}{\mu}}e^{i\left(\omega t - \frac{z}{\mu} - \frac{\pi}{4}\right)},$$

$$(1.26)$$

in which $\mu = \sqrt{\frac{D}{\pi f}}$ is the thermal diffusion length, the distance at which the temperature decays a factor of e from its value on the surface. Note that μ increases with the thermal diffusivity of the sample and decreases with the modulation frequency. Equation (1.26) is often called a thermal wave.

When steady state is reached, the oscillating dependence of the temperature can be left aside, and the equation depends only on the spatial coordinate. If we consider the temperature as a phasor, it can be separated as amplitude and phase:

$$Amplitude\,[\,T_{ac}(z)] = \frac{\eta I_0}{2e\sqrt{\omega}}e^{-\frac{z}{\mu}}, \qquad (1.27)$$

$$Phase\,[\,T_{ac}(z)] = -\frac{z}{\mu} - \frac{\pi}{4} \qquad (1.28)$$

where $e = \sqrt{\rho c K} = K/\sqrt{D}$ is the thermal effusivity, which describes a body's ability to exchange heat or energy with the environment [23,24]. Note that at the surface there is a phase lag of -45° between the heat source and the resulting temperature oscillation (equation 1.28).

The wavelength of the thermal wave is $2\pi\mu$, and therefore the thermal wave is fully damped within one thermal wavelength. In Figure 1.7 we show the calculations of the amplitude and phase of the temperature T_{ac} as a function of z for a frequency $f = 1$ Hz, calculated for a semi-infinite sample made of AISI-304 stainless, with $\eta = 1$, $I_0 = 0.2$

Wm^{-2}, $D = 4 \times 10^{-6}$ m^{2}s^{-1} and $K = 15$ Wm^{-1}K^{-1}. The amplitude is normalized for the sake of clarity.
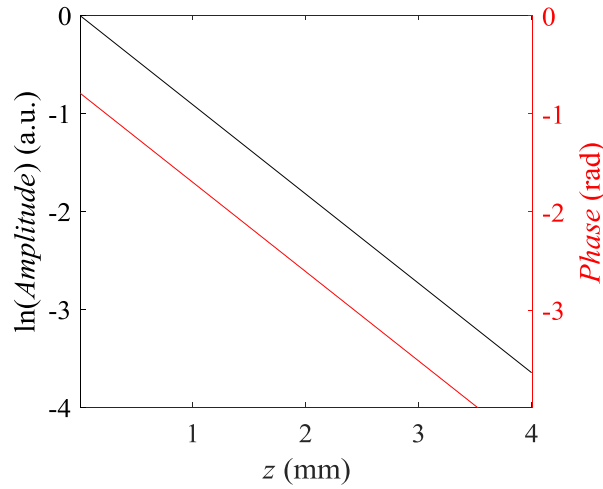
Figure 1.7: Phase and natural logarithm of the amplitude (normalized) of a semi-infinite sample ($D = 4 \times 10^{-6}$ m^{2}s^{-1}, $K = 15$ Wm^{-1}K^{-1}) illuminated by a plane light beam, modulated at f = 1 Hz, as a function of the distance z.

Now, let us suppose the same previous sample is illuminated by a focused light beam (Figure 1.8), whose power is P_0 and features a Gaussian profile of radius a at $1/e^2$ of the maximum intensity. The absorbed flux produced at $z = 0$ is

$$\Phi(r) = \frac{\eta P_0}{\pi a^2} e^{-\frac{2r^2}{a^2}} . \tag{1.29}$$

where $r = \sqrt{x^2 + y^2}$.
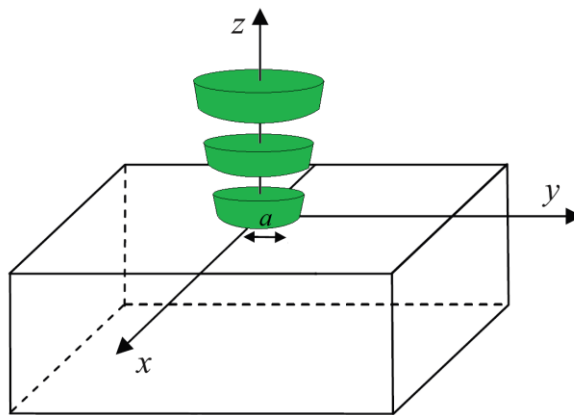
Figure 1.8: Scheme of a semi-infinite sample illuminated by a focused light beam.

Due to the cylindrical symmetry of the problem, it is useful to work in the Hankel space [25], where the Helmholtz equation reduces to:

$$\frac{\partial^2 \bar{T}_{ac}(\delta, z)}{\partial z^2} - (\sigma^2 + \delta^2)\bar{T}_{ac}(\delta, z) = 0, \tag{1.30}$$

where δ is the conjugate variable of the radial coordinate r in the Hankel space, and $\bar{T}_{ac}$ is the Hankel transform of the temperature T_{ac}. The Hankel transform of the Gaussian profile, given by equation (1.29), is

$$\bar{\Phi}(r) = \frac{\eta P_0}{4\pi} e^{-\frac{(\delta a)^2}{8}}, \tag{1.31}$$

and therefore, the boundary condition, also in the Hankel space, is

$$-K\frac{d\bar{T}_{ac}}{dz}\bigg|_{z=0} = \frac{\eta P_0}{4\pi} e^{-\frac{(\delta a)^2}{8}}. \tag{1.32}$$

We will apply the same procedure as the plane beam case, obtaining

$$\bar{T}_{ac}(\delta, z) = \frac{\eta P_o}{4\pi K}\frac{e^{\beta z}}{\beta} e^{-\frac{(\delta a)^2}{8}}. \tag{1.33}$$

where $\beta^2 = \sigma^2 + \delta^2$. Finally, by performing the inverse Hankel transform to equation (1.33), we obtain the sample temperature

$$T_{ac}(r, z) = \frac{\eta P_o}{4\pi K} \int_0^\infty \frac{e^{\beta z}}{\beta} e^{-\frac{(\delta a)^2}{8}} J_o(\delta r)\delta \ d\delta. \tag{1.34}$$

It is still possible to get an analytical solution to this equation if we consider an ideal focusing of the laser beam, with an infinitely small laser spot ($a = 0$). Equation (1.34), therefore, reduces to

$$T_{ac}(R, z, a = 0) = \frac{\eta P_o}{4\pi K} \int_0^\infty \frac{e^{\beta z}}{\beta} J_o(\delta r)\delta \ d\delta = \frac{P_o}{4\pi K}\frac{1}{R}e^{-\sigma R}, \tag{1.35}$$

where $R = \sqrt{r^2 + z^2}$. This equation represents a spherical thermal wave. As it has been done before, it can be split into the amplitude ($|T|$) and phase (φ) contributions:

$$T_{ac}(R, a = 0) = \frac{\eta P_o}{4\pi K} \frac{1}{R} e^{-\frac{1}{\mu}R} e^{-i\frac{1}{\mu}R} = |T| e^{-i\varphi}, \qquad (1.36)$$

where the thermal diffusion length μ has the same expression as for flat illumination. As we may see, both the phase φ and the natural logarithm of the amplitude multiplied by the distance to the laser spot, $ln(|T|R)$, behave linearly as a function of the distance to the excitation point, with the same slope

$$m_\varphi = m_{ln(|T|R)} = -\frac{1}{\mu} = -\sqrt{\frac{\pi f}{D}}. \qquad (1.37)$$

These linearities provide a simple method, based on a linear fit, to measure the in-plane thermal diffusivity of solids [26,27]. By performing calculations using equation (1.34), it can be seen that a finite laser spot size does not modify the above mentioned slopes, except for positions close to the excitation beam. This result is shown in Figure 1.9. Calculations have been performed for the surface temperature of AISI-304 stainless steel ($D = 4$ mm^2/s, $K = 15$ W m^{-1}K^{-1}) with $\eta = 1$, $P_0 = 0.2$ W, $f = 1$ Hz and $a = 0.5$ mm.
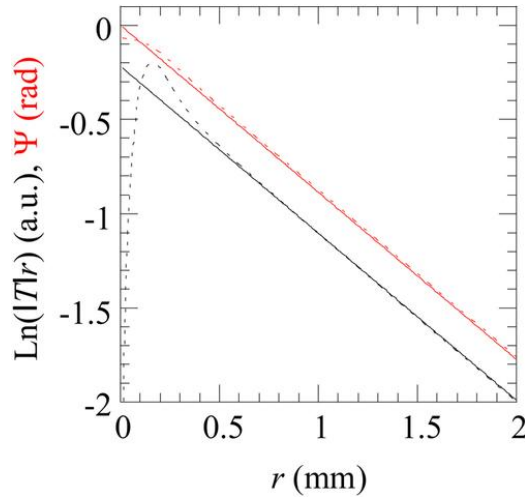
Figure 1.9: Phase (red) and natural logarithm of the amplitude multiplied by the distance (black) of the surface temperature of a semi-infinite sample ($D = 4$ mm^{2}s^{-1}, $K = 15$ Wm^{-1}K^{-1}) illuminated by a modulated focused light beam ($f = 1$ Hz) as a function of the distance to the heating spot. Continuous lines represent an ideal focusing ($a=0$) of the light beam, while dashed lines account for the effect of a real beam focusing of radius $a = 0.5$ mm.

IRT with focused modulated illumination will be applied widely in this work to measure thermal diffusivity of materials and to detect and characterize cracks. In that sense, equations 1.35 (or 1.36) are the starting point for most of the work in this thesis. These equations represent the (almost) spherical thermal wave that one encounters in isotropic homogeneous media at rest. As shown above, these equations lead to linear relationships of amplitude and phase with the distance to the exciting spot, which provide a simple and convenient way to measure the thermal diffusivity.

After introducing the experimental details in Chapter 2, in Chapter 3, we will present three methods to measure the thermal diffusivity in samples that are either at rest or moving at constant velocity. In all three cases, we will seek simple linear relationships to measure the thermal diffusivity, as can be seen in Figure 1.9 and equation (1.37). Moreover, we will analyze how the spherical waves represented by equations (1.35) and (1.36) are distorted when the sample is in motion.

In Chapter 4 we will deal with different cases of cracked materials. We will show how the spherical thermal waves are modified by the presence of a fissure or crack. The analysis of the resulting thermal field will lead us to find methods to determine the width, penetration and orientation of cracks, and to measure the thermal conductivity of a fluid filling the gap produced by an infinite vertical crack.

Finally, we present our conclusions and future trends.

2. Experimental techniques

2.1. Experimental setup description

All the experiments shown in this work have been carried out at the Photothermal Techniques Laboratory at UPV/EHU, using a laser device as the source of illumination and an Infrared Camera as a detector. The main experimental configuration is shown in Figure 2.1.
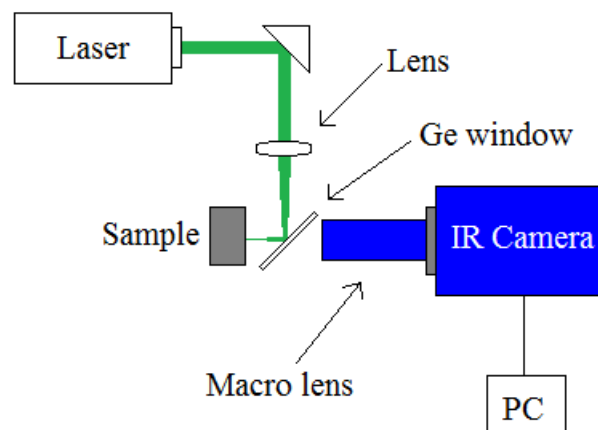
Figure 2.1: Basic experimental setup

<u>Laser</u>

The laser used is a Coherent Verdi V6 (frequency-doubled) Nd:YAG laser, which is a continuous wave laser emitting at 532 nm, with a power range of 0.01 W to 6 W. The minimum power is usually used for thermal insulators, and the maximum power is never used in this work. Only for some metallic samples the power is increased up to 1-2 W. The laser beam features a Gaussian profile with a radius $a = 1$ mm, which is the distance from the center where the intensity decays by a factor e^2.

Convex lens

The laser beam is focused using a 10 cm focal length biconvex lens. When the lens position is adjusted, the radius *a* can be increased or reduced. The typical beam radius at the sample surface has approximately 200 μm, although for some experiments it has been reduced to 50 μm. When small radius is used, the energy density at the center of the spot is increased, so the laser power has to be readjusted to obtain the desired temperature increase on the sample surface.

Germanium Window

Following the beam path, just after the lens, a germanium window is placed in front of the camera objective at 45º with respect to the laser direction to redirect the beam to the sample, so the beam reaches the sample surface perpendicularly. The germanium window is only transparent to wavelengths longer than 2 μm, so it prevents visible radiation from reaching the camera. An antireflection coating provides high IR transmission, decreasing the average reflection. Using this window any radiation with a wavelength outside the range 2 - 12 μm is blocked.

IR Camera

An infrared camera FLIR, model SC7000, is used to record the temperature field at the surface of the samples. The detector is composed by InSb sensors, providing the camera a spectral band from 3 to 5 μm, which corresponds to the Mid-Infrared region, with a 30 μm pitch.

In all measurements, the camera is equipped with a 1:1 macro lens, so each pixel of the detector senses the average temperature over a 30 μm square of the sample. The maximum window has a size of 320 x 256 pixels (9.60 mm x 7.68 mm with the macro lens), but it can be customized at smaller sizes, selecting a Window of Interest (WOI).

The reduction of the window is useful if we only want to focus on a certain region, so the camera does not record sample areas which do not provide information – e.g., there is no temperature variation in that region or the variation is not of interest.

Reducing the window also allows increasing the maximum Frame Rate (FR). The FR is defined as the inverse of the sum of the integration time (IT) and the read out time (time spent reading the integrated signal: number of pixels/pixel clock), so FR = 1/(IT + readout time).

The maximum FR value available at full window is 383 Hz, which is a value limited by the readout time, but it can be increased to values over 28000 Hz in the particular conditions of small integration time and reducing the window to the minimum (4 x 64 px). However, a most common window resizing, used in some experiments in this work, is 320 x 140 px, which allows a maximum FR of 691 Hz.

Integration time

The integration time IT is the period of time during which the detectors collect the signal. It is a parameter that can be set by the user, within a range from 10 μs to 2.2 ms. The higher the temperature, the lower the needed IT, and vice versa. For example, for room temperature measurements a typical value is ~1 ms, but if the temperature reaches values around 300 - 400 °C, the IT can be reduced down to 10 μs.

Nevertheless, there are some limitations. If the IT is set too long, the signal can be saturated. On the other hand, if it is set too small, fewer photons will be detected and the signal will be noisier.

Many combinations of the FR, the IT and window size are possible. In this work, the IT has been kept fixed because we work at room temperature and the temperature elevations are always of the same order (5 – 15 K), so the FR can be increased decreasing the window size.

NETD

The NETD (Noise Equivalent Temperature Difference) is the measure for how well the thermal detector is capable of distinguishing between very small differences of temperature in the image. It is often taken as the temperature resolution of the camera, as it is the temperature that produces a signal that is equal to the noise of the sensor. The NETD is a property of the camera evaluated in specific conditions of IT, temperature of the scene and frame rate. In the case of this study it is approximately 20 mK [28].

Non – Uniformity Correction

The individual pixel response differs considerably across an array, so pixel correction has to be done. The Non-Uniformity Correction (NUC) adjusts the small drifts on the detector. It adjusts the offset for each pixel in order to enhance the quality and to obtain a more accurate image. It is needed to place a dark object (in order to emulate a blackbody) in front of the objective, like a black cardboard. In Figure 2.2 this procedure is shown when it is performed incorrectly (a) (the cardboard is placed wrongly), and correctly (b). As it can be seen, this adjustment homogenizes the image, fixing the horizontal temperature drift that appears in Figure 2.2a.
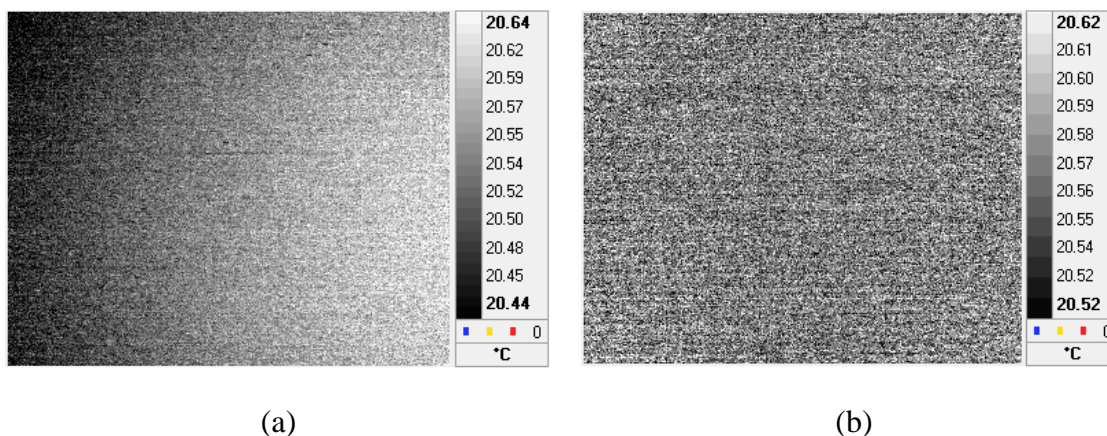

(a)   (b)

Figure 2.2: NUC performed on the camera. In (a) the NUC is not done properly, and in (b) the thermogram is homogenized applying correctly the NUC.

Narcissus effect

The Narcissus effect appears when the sensor detects sources at temperatures different from the background ambient temperature, originated by reflections of the detector on the sample surface. It is usually described as the detector seeing its own radiation, hence the name Narcissus.

It commonly appears as a disk at the center of the thermogram, as it can be seen in Figure 2.3a. The center of the image appears as a low temperature zone, and the effect vanishes radially towards the edges. The sample, however, has a uniform temperature distribution, so it is an artefact that has to be eliminated.

The Narcissus effect can be erased easily when a Lock-in measurement is performed. When this technique is applied, only the oscillations of temperature at a reference frequency with respect to ambient temperature are taken into account, so any other contribution, like the Narcissus, disappears.

When the illumination is continuous, the Narcissus effect can be overcome by subtracting a reference image/s from the measurement recording, so the resulting recording only takes into account any temperature difference from the background (Figure 2.3b).
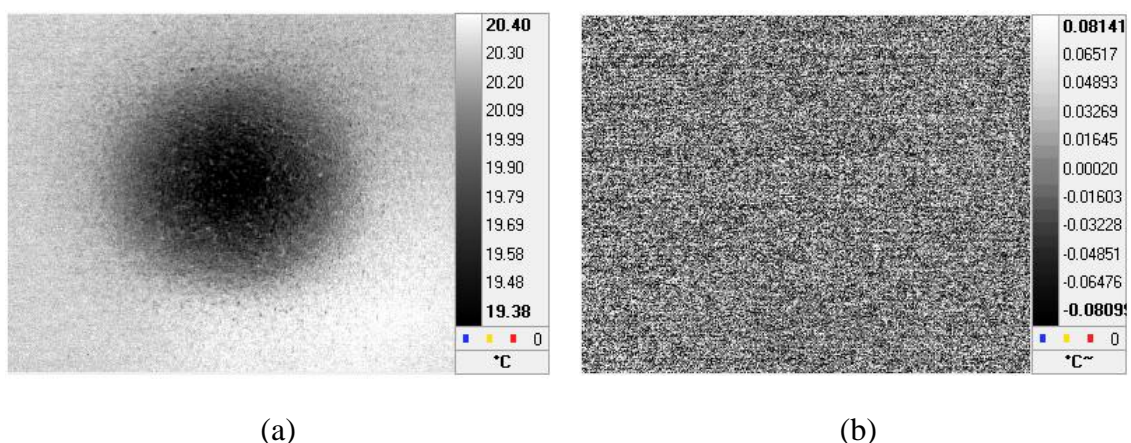

(a)   (b)

Figure 2.3: Narcissus effect (a) and its correction using reference subtraction (b). Thermogram (b) is obtained subtracting two different frames at different times, with no excitation.

<u>Sample treatment</u>

Usually, typically in metals, the sample surface is not perfectly homogeneous, it is too bright or polished (introducing unwanted reflections) or it has low emissivity.

To overcome these issues, first we must ensure that the surface is completely flat and free of dust, so it is cleaned up using acetone or some alcohol like propanol.

Opaque samples that have low IR emissivity are usually painted with a thin layer of sprayed graphite. This layer helps to homogenize and increase the emissivity, and it enhances absorption to the laser wavelength, so the signal to noise ratio (SNR) is enhanced. The graphite layer, which is expected not to have an effect on the measurements, has a typical thickness of 3 - 5 μm.

Once the sample is prepared, it has to be placed at the plane imaged by the camera optics on the detector, with the surface perpendicular to the objective axis. As the camera and objective are fixed, the sample has to be focused manually, using a holder with submilimetric forward-backward moving system.

2.2. Experimental setup: particular cases

The setup shown until now is the basic configuration. For each different type of measurement, the initial experimental setup has to be modified adding new elements: an optical chopper at the middle of the beam path and/or a moving cart on a track holding the sample (see Figure 2.4).
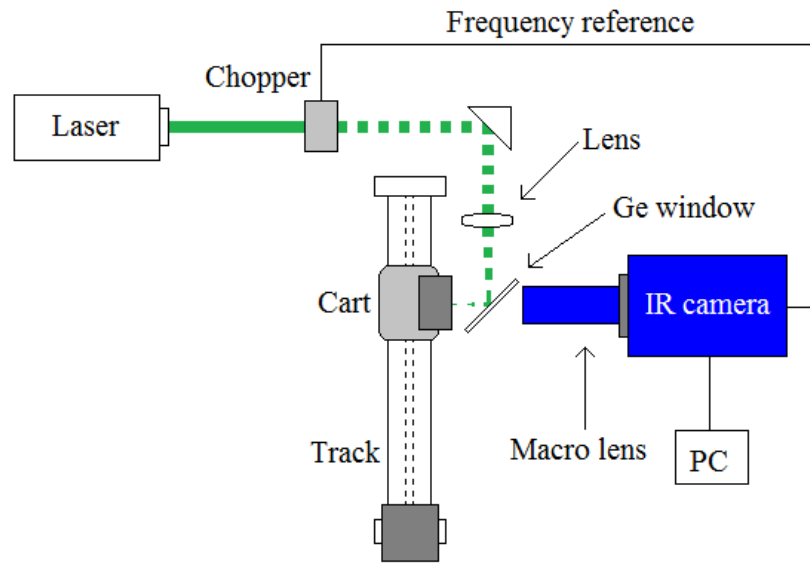
Figure 2.4: Complete experimental setup.

According to the scheme, these are the different setup options:

- Continuous illumination and sample at rest: the cart remains static and the chopper is set to an open position.
- Continuous illumination and moving sample: the cart is moving and the chopper is set to an open position.
- Modulated illumination and static sample: the cart remains static and the chopper is turned on.
- Modulated illumination and moving sample: the cart is moving and the chopper is turned on.

2.2.1. From Continuous to Modulated illumination

The simplest configuration is mounted when the experiment takes place with continuous illumination and placing the sample at rest, which is the case that we have seen. If an optical chopper is added, modulated illumination measurements can be

performed. This device is used to modulate the laser beam at a desired frequency, so the light is interrupted periodically following a square signal, although it is only measured its fundamental frequency (first harmonic).

It consists of a circular disk with several blades spread periodically. Different kind of disks can be used to obtain a wide range of frequencies: for example, a 2-blade chopper is used for low frequencies ($0.2 - 15$ Hz) and a 20-blade chopper is used for high frequencies (2 - 150 Hz)).

The disk is screwed to an engine, so the modulation frequency is controlled by the rotation speed. A sensor located at the base of the chopper detects the frequency and the chopper controller displays an approximate value of it. A connection between the chopper and the camera provides the required synchronization.

The camera software Altair-LI is able to analyze a modulated signal and split into its amplitude and phase using Lock-in Amplification [29]. A block diagram of this procedure is shown in Figure 2.5.

Figure 2.5: Scheme of Lock-in Amplification
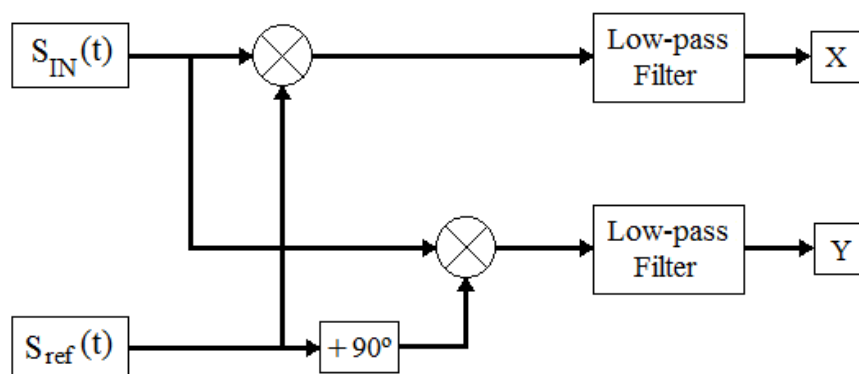
The process starts with input signal to be processed,

$$S_{IN}(t) = A \sin(2\pi f t + \phi) + n(t) \tag{2.2}$$

where A is the signal amplitude, f is the frequency, ϕ is the phase (with respect to a sinusoidal reference signal) and n is the contribution of random noise, the other harmonics of the fundamental frequency and any other signal which is not modulated at

the fundamental frequency, like the Narcissus effect. The input signal is correlated, on one hand, with the reference sinusoidal signal sent from the chopper,

$$S_{ref}(t) = \sin(2\pi ft) \tag{2.3}$$

and, on the other hand, with the same reference shifted by 90º,

$$S_{ref'}(t) = \sin(2\pi ft + 90) = \cos(2\pi ft) \tag{2.4}$$

obtaining the following signals:

$$P_X = S_{IN} \times S_{ref} \tag{2.5}$$

$$P_Y = S_{IN} \times S_{ref'} \tag{2.6}$$

Where × means correlation. In the time domain, these correlations are written as:

$$P_X(t) = \frac{1}{2}(A\cos(\phi) - A\cos(4\pi ft + \phi)) + S_{ref'}(t)n(t) \tag{2.7}$$

$$P_Y(t) = \frac{1}{2}(A\sin(\phi) + A\sin(4\pi ft + \phi)) + S_{ref}(t)n(t) \tag{2.8}$$

When the signal passes through the Low-pass filters, the sinusoidal and the noisy components are filtered and only the non-oscillatory components are left (they are not oscillatory because the input signal and reference signal have the same frequency). The output signals are:

$$X = \frac{A}{2}\cos(\phi) \tag{2.8}$$

$$Y = \frac{A}{2}\sin(\phi) \tag{2.9}$$

Consequently, the amplitude and phase can be retrieved solving the 2 variable set of 2 equations, obtaining

$$A = \frac{1}{2}\sqrt{X^2 + Y^2} \tag{2.10}$$

$$\phi = \tan^{-1}\left(\frac{Y}{X}\right) \tag{2.11}$$

A remarkable advantage of using the Lock-in technique is the reduction of noise. When the lock-in averaging is not carried out, the noise in the data is given (at least) by the NETD. However, when the signal is modulated (as a result of the modulated illumination) the lock-in analysis described above results in a final pair of thermograms

(Amplitude and Phase). The noise in amplitude and phase depends on the NETD of the camera and the number of images analyzed in the lock-in process, according to Equation (2.12) [30]:

$$\langle\, Noise_T \rangle \;=\; \frac{2}{\sqrt{N_{Images}}}\; NETD\,, \tag{2.12}$$

where N_{Images} is the number of frames acquired by the camera. Accordingly, the average noise in data can be reduced by analyzing a high number of images. For instance, using a FR of 350 Hz and recording during 5 seconds, the resulting number of frames is 1750, and therefore, the average noise is smaller than 1 mK.

In Figure 2.6 three thermograms are shown. They correspond to amplitude thermograms resulting from a lock-in correlation on a steel sample at rest, with no excitation. The FR is 383 Hz, and the analysis was performed on the images acquired during 5 s (a), 10 s (b) and 20 s (b). The average noise decreases from 1.17 mK to 0.46 mK as it is expected from Equation (2.12).

When the fundamental frequency is low, the lock-in analysis filters worse the continuous signals, because a low frequency signal is closer to the continuous than a high frequency signal. As a consequence, some effects (like the Narcissus effect) may remain present in the image. This is solved increasing the number of images, so more recording time is needed.

(a)

(b)

(c)
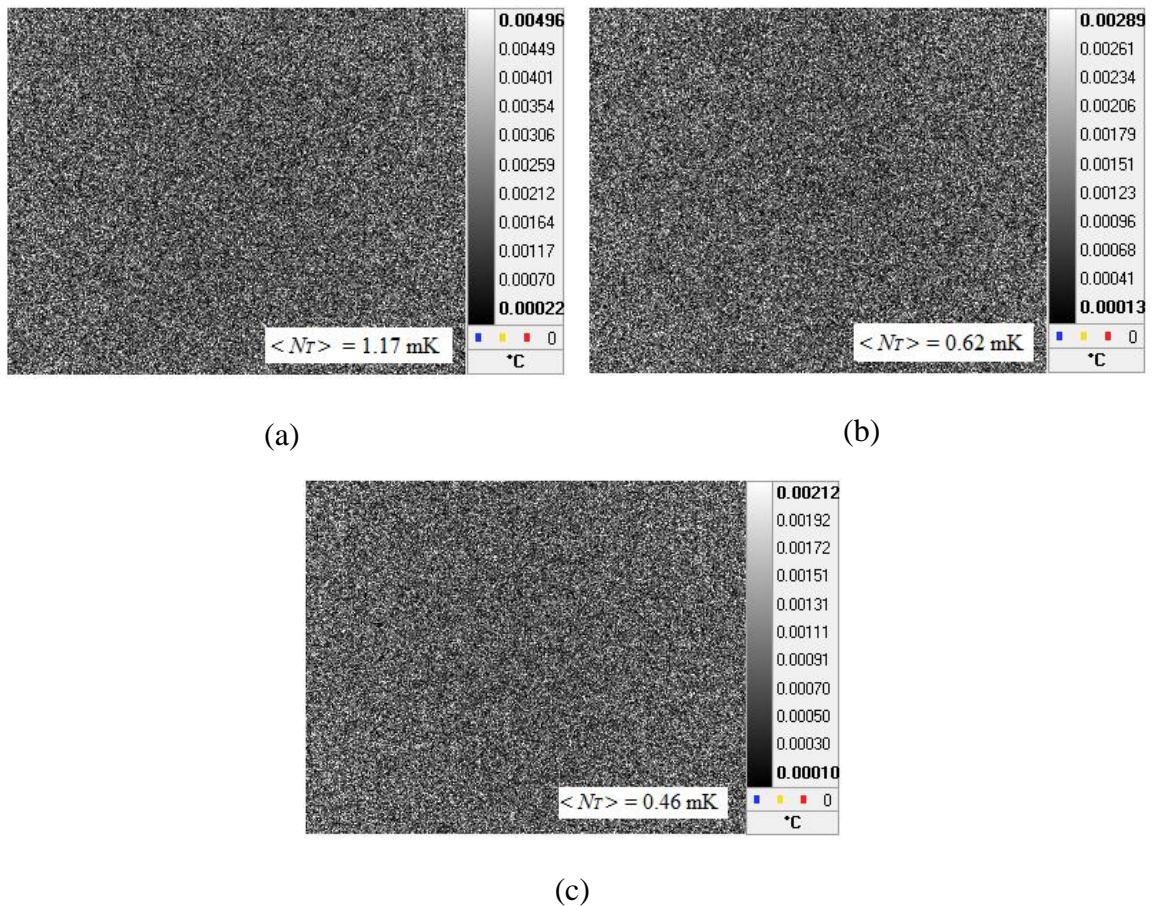
Figure 2.6: Evolution of the average temperature noise using lock-in processing. Amplitude images after acquisition periods of (a) 5 s, (b) 10 s and (c) 20 s.

2.2.2.   From static to moving samples

For the in-motion measurements, the samples are mounted on a moving cart. The cart moves freely over a carbon fiber slider system. It is connected to a motor, so as the motor rotates, the cart slides in one direction of the track.

The cart can move in a wide range of velocities, form less than 0.1 mm/s to 150 mm/s, and it can move from left to right or from right to left. The velocity is specified introducing in the controller the desired initial and final positions and the time interval in which the cart will be moving. The track that guides the cart can be lined perpendicular to the beam axis and to the camera axis using a pair of 3-axis supports, located at both ends of the track. This alignment is crucial: the sample has to be on

focus along its whole length and move parallel to the horizontal direction of the focal plane array of the camera.

The measurement process is the following:

1. Preparation of the video recording in Altair software: setting up of the frame rate, integration time and recording time.
2. Preparation of the sample velocity through the cart controller.
3. Starting up the cart and starting the recording just before the sample enters the field of view of the camera
4. Recording of a "reference" video, that is, a video of the sample with no laser excitation.
5. Repeat the same procedure as in 3, but with the laser switched on.

Once these measurements are done, the reference video is subtracted from the excited video. Before the subtraction is done, it is necessary that both videos have the same length (they must be trimmed to have the same number of frames) and that they correspond exactly to the same part of the sample.

3. Thermal diffusivity measurement: new configurations.

The following sections will cover the contributions on in-plane thermal diffusivity measurement. Firstly, in Section 3.1, a step-heating procedure is presented. Section 3.2 presents a moving sample with continuous illumination configuration. Finally, Section 3.3 will cover the diffusivity measurements on moving samples using modulated illumination and lock-in processing.

3.1. Continuous excitation and static sample. Laser-spot Step-heating thermography.

3.1.1. Introduction

A useful technique to measure the in-plane thermal diffusivity of solids is the Laser-Spot Infrared Thermography. This technique uses a focused laser beam to heat the sample and an infrared camera to record the surface temperature of this sample. Depending on the time profile of the laser excitation, there are, basically, three possible configurations: harmonically modulated illumination, pulsed excitation and step-heating illumination.

Regarding the first case, the use of modulated excitation results in low-noise thermograms thanks to the lock-in process. As the number of acquired frames increase, the noise level decreases. The thermal diffusivity is retrieved from linear dependences of the amplitude and phase thermograms with the distance to the center of the spot. This technique has been used on thermal diffusivity measurements of bulk samples [27,31-40] and thin films and filaments [26,41-51]. Regarding the laser-spot pulsed excitation, this type of infrared thermography has been used to measure the diffusivity of solids using a very brief laser pulse [35,52-56]. Both the lock-in and the pulsed excitation allow accurate measurements of thermal diffusivity, although the lock-in configuration requires more sophistication. Moreover, the pulsed excitation is less used than the lock-in procedure, because high energy lasers are used to perform the experiments and they can be dangerous, besides its cost and the possibility of damaging the sample.

The third configuration, which is the one proposed in this Section, consists in switching on the laser at a given instant and recording the evolution of the surface temperature of the sample using an infrared camera. So far, laser-spot step-heating has not been used to measure thermal diffusivity, possibly because a poor signal to noise ratio (SNR) was expected. Our purpose is to evaluate whether a low-cost laser-spot step-heating thermography system provides accurate enough diffusivity values for reliable implementation in both R&D departments and industrial environments, without the need of a sophisticated signal processing.

3.1.2.   Objectives

The main objectives of this study are:

- To design a new method to measure in-plane thermal diffusivity using laser-spot step-heating illumination.

- To apply the method on a large variety of calibrated samples: from insulators to good heat conductors, on thick and thin samples, and on opaque or transparent materials.

- To corroborate that this procedure can be implemented in a low-cost setup consisting of non-expensive laser and camera.

3.1.3. Theoretical analysis

First of all, an isotropic and homogeneous material of thickness L is considered. The continuous wave laser is focused on the sample surface (see Figure 3.1) at the spatial point ($r = 0$, $z = 0$), where the center of spot is located. The power density of the laser has a Gaussian profile as it follows:

$$P(r) = \frac{P_o}{\pi a^2} e^{-\frac{2r^2}{a^2}},$$ (3.1)

where P_o is the laser power and a is the beam radius at $1/e^2$. The illumination as a function of time follows a Heaviside function. The laser is switched on at $t = 0$ s, so for $t > 0$ s the power of the laser is P_o, and for $t < 0$ s the power is 0.
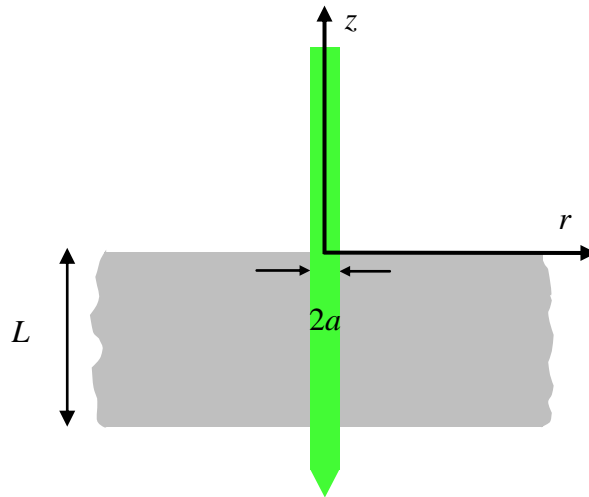

Figure 3.1: Cross section of the sample, with the surface being illuminated perpendicularly by the focused laser beam of radius a.

In order to derive the equations that will allow us to measure the diffusivity, the Heat Diffusion equation has to be solved,

$$\nabla^2 T(r,z,t) - \frac{1}{D}\frac{\partial T(r,z,t)}{\partial t} = -\frac{Q(r,z,t)}{K}, \tag{3.2}$$

where T is the temperature elevation above room temperature at any position (r, z) and at any time t, Q is the energy absorbed by the sample per unit time and unit volume, K is the thermal conductivity and D is the thermal diffusivity of the material.

The energy is absorbed by the sample and decays exponentially through z following the Beer-Lambert law,

$$Q(r,z,t) = \eta P(r)u(t)\alpha e^{\alpha z}, \tag{3.3}$$

where η is the fraction of power that is absorbed by the sample, $u(t)$ is the Heaviside function and α is the optical absorption coefficient at the laser wavelength. As we are using cylindrical coordinates, we can easily perform a double transformation on equation (3.2) to solve it. First, a Laplace transform is applied:

$$\nabla^2 \bar{T}(r,z,s) - \frac{s}{D}\frac{\partial \bar{T}(r,z,s)}{\partial t} = -\frac{1}{K}\eta P(r)\frac{1}{s}\alpha e^{\alpha z}, \tag{3.4}$$

where $\bar{T}$ is the Laplace transform of T and s is the conjugate variable of time. We can now apply the Hankel transform on equation (3.4) [25]

$$\frac{d^2\widehat{\bar{T}}(\delta,z,s)}{dz^2} - \beta^2\widehat{\bar{T}}(\delta,z,s) = -\frac{1}{K}\frac{\eta P_0}{2\pi}e^{-\frac{(\delta a)^2}{8}}\frac{1}{s}\alpha e^{\alpha z}, \tag{3.5}$$

where $\widehat{\bar{T}}$ is the Hankel transform of $\bar{T}$, δ is the conjugate variable of r and $\beta^2 = \frac{s}{D} + \delta^2$. The Hankel transform of $P(r)$ (equation 3.1) is equal to $\frac{P_0}{2\pi}e^{-\frac{(\delta a)^2}{8}}$.

Equation (3.5) has a general solution of the form

$$\widehat{\bar{T}}(\delta,z,s) = Ae^{-\beta z} + Be^{\beta z} + Ce^{\alpha z}, \tag{3.6}$$

where $C = \frac{1}{K}\frac{\eta P_0}{2\pi}e^{-\frac{(\delta a)^2}{8}}\frac{1}{s}\frac{\alpha}{\beta^2-\alpha^2}$. The boundary conditions of the problem allow us to obtain the factors A and B. If the heat losses coefficient h is introduced (which contains the contribution of radiation and convection), the flux continuity equations at the front

and rear surfaces in the Laplace-Hankel space write as $-K\frac{d\hat{\bar{T}}}{dz}\Big|_{z=0} = h\hat{\bar{T}}(z=0)$ and

$-K\frac{d\hat{\bar{T}}}{dz}\Big|_{z=-L} = -h\hat{\bar{T}}(z=-L).$

Finally, if we substitute equation (3.6) into the boundary conditions, we obtain the general expression for the temperature,

$$\hat{\bar{T}}(\delta, z, s) = C\left[\frac{Ee^{-\beta z} + Fe^{\beta z}}{(1+H)^2 e^{\beta L} - (1-H)^2 e^{-\beta L}} + e^{\alpha z}\right], \qquad (3.7)$$

where

$$E = \left(\frac{\alpha}{\beta} - H\right)(1+H)e^{-\alpha L} - \left(\frac{\alpha}{\beta} + H\right)(1-H)e^{-\beta L}, \qquad (3.8)$$

$$F = \left(\frac{\alpha}{\beta} - H\right)(1-H)\,e^{-\alpha L} - \left(\frac{\alpha}{\beta} + H\right)(1+H)e^{\beta L}, \qquad (3.9)$$

and the heat losses factor $H = h / K\beta$. Now, to obtain the temperature in the real space, the inverse Hankel and Laplace transforms have to be performed on equation (3.7), but there is no analytical solution for it. However, we can obtain analytical expressions of the surface temperature if we focus on three cases of interest that cover the vast majority of materials: the thick and opaque case, the thin and opaque case and the transparent case.

A.   Thermally thick and opaque sample

A material is considered opaque when α tends to ∞, so the term $e^{-\alpha L}$ can be neglected. Moreover, a sample is considered thick if its thickness L is much greater than the thermal diffusion length (μ). In this step-heating configuration, $\mu = \sqrt{Dt}$ [57], and therefore, if $L \gg \mu$, then the term $e^{-\beta L}$ can also be neglected. Finally, the surface temperature ($z = 0$) under these conditions in the Laplace-Hankel space is

$$\hat{\bar{T}}(\delta, 0, s) \approx \frac{1}{s} \frac{\eta P_0}{2\pi K} e^{-\frac{(\delta a)^2}{8}} \frac{1}{\beta + \frac{h}{K}}.$$
(3.10)

And applying the double inverse Laplace and Hankel transforms, we obtain

$$T(r, 0, t) \approx \frac{\eta P_0}{2\pi K} \int_0^\infty \delta J_0(\delta r)\, e^{-\frac{(\delta a)^2}{8}} \times$$

$$\times \frac{\frac{h}{K}\left[e^{-Dt\left(\delta^2 - \frac{h^2}{K^2}\right)} - 1\right] - \frac{h}{K} e^{-Dt\left(\delta^2 - \frac{h^2}{K^2}\right)} erf\left(\frac{h\sqrt{Dt}}{K}\right) + \delta erf\left(\delta\sqrt{Dt}\right)}{\delta^2 - \frac{h^2}{K^2}} d\delta,$$
(3.11)

where J_o is the order zero Bessel function and *erf* is the error function. If the effect of heat losses is negligible, the surface temperature is significantly simplified:

$$T(r, 0, t) \approx \frac{\eta P_0}{2\pi K} \int_0^\infty J_0(\delta r)\, erf\left(\delta\sqrt{Dt}\right) e^{-\frac{(\delta a)^2}{8}} d\delta.$$
(3.12)

B.   Thermally thin and opaque sample

In the case of $L \ll \mu$ (the sample is considered thermally thin) the following exponential term can be approximated: $e^{\pm \beta L} \approx 1 \pm \beta L$, and, therefore, equation (3.7) simplifies to:

$$\hat{\bar{T}}(\delta, 0, s) \approx \frac{1}{s} \frac{\eta P_0}{2\pi KL} e^{-\frac{(\delta a)^2}{8}} \frac{1}{\beta^2 + \frac{2h}{KL}}.$$
(3.13)

Applying the inverse transforms, the surface temperature is obtained:

$$T(r, 0, t) \approx \frac{\eta P_0}{2\pi KL} \int_0^\infty \delta J_0(\delta r)\, e^{-\frac{(\delta a)^2}{8}} \frac{1 - e^{-Dt\left(\delta^2 - \frac{2h}{KL}\right)}}{\delta^2 - \frac{2h}{KL}} d\delta.$$
(3.14)

C.   Highly transparent sample

A highly transparent material has very poor absorption, so $\alpha \to 0$, and consequently $e^{-\alpha L} \approx 1$. Equation (3.7) can be written as:

$$\hat{\bar{T}}(\delta, 0, s) \approx \frac{1}{s} \frac{\eta P_0}{2\pi K} e^{-\frac{(\delta a)^2}{8}} \frac{\alpha}{\beta^2 + \frac{2h}{KL}} . \tag{3.15}$$

Once the inverse double transform is applied, the surface temperature is obtained:

$$T(r, 0, t) \approx \frac{\eta P_0 \alpha}{2\pi K} \int_0^\infty \delta J_0(\delta r) \, e^{-\frac{(\delta a)^2}{8}} \frac{1 - e^{-Dt\left(\delta^2 - \frac{2h}{KL}\right)}}{\delta^2 - \frac{2h}{KL}} \, d\delta . \tag{3.16}$$

3.1.4.   Numerical calculations

A.   Opaque and thermally thick material

Equation (3.11) is used to calculate the temperature profiles of a thick and opaque sample when it is illuminated by the laser beam switched on at a time $t = 0$ s. In the next figures we will plot the natural logarithm of T rather than the temperature to enhance the low temperature differences at long distances from the laser spot position.

In Figure 3.2a four temperature profiles are plotted, using the following parameters: $D = 0.2$ mm^2/s, $K = 0.4$ Wm^{-1}K^{-1}, $a = 0.2$ mm and $\eta P_o = 0.01$ W. Two different instants of time are considered: 1 s (black lines) and 5 s (red lines). The solid lines correspond to a heat loss coefficient $h = 0$ Wm^{-2}K^{-1} (adiabatic boundaries) and the dashed lines correspond to a heat loss coefficient $h = 10$ Wm^{-2}K^{-1} (realistic value at room temperature [46]). In Figure 3.2b we also show the profiles at 1 s and 5 s for the same parameters except for the thermal diffusivity: in one case, $D = 0.2$ mm^2/s (solid lines) and in the other case, $D = 0.4$ mm^2/s (dashed lines), without heat losses, in order to see how the profiles are changed.

It can be seen that heat propagates at longer radial distances as time goes by. The temperature at the position of the laser spot, however, remains almost unchanged. Moreover, an increase of thermal diffusivity produces a rise in the profile branches, as it is shown in Figure 3.2b. It is important to notice that we have checked that the effect of heat losses is negligible (even though we performed the calculations for a low-conductivity material), as the profiles with and without heat losses are indistinguishable. In that sense, the effect of heat losses can be neglected in room temperature measurements.

According to this conclusion, equation (3.12) (instead of equation (3.11)) will be fitted to experimental temperature profiles. Moreover, the profiles obtained at different instants of time will be fitted simultaneously in order to obtain a more consistent diffusivity value than if the fit is only performed at one instant. Two free parameters will be fitted: $\eta P_o / K$ and D.

Figure 3.2: (a) Calculations of the temperature profiles $\ln(T)$ for an opaque and thermally thick sample ($D = 0.2$ mm^2/s, $K = 0.4$ Wm^{-1}K^{-1}) at 1 s (black) and at 5 s (red), with different heat losses coefficients: $h = 0$ (solid lines) and $h = 10$ Wm^{-2}K^{-1} (dashed lines). (b) Calculations of the temperature profiles $\ln(T)$ for an opaque and thermally thick sample at 1 s (black) and at 5 s (red), with no heat losses, with different diffusivities: $D = 0.2$ mm^2/s (solid lines) and $D = 0.4$ mm^2/s (dashed lines).

B. Opaque and thermally thin material / Transparent material

In Figure 3.3a we plot the temperature profiles for the same opaque sample and experimental parameters as in Figure 3.2a, but adding thickness as a new parameter: $L = 50$ μm. We use equation (3.14) to perform the calculations for two instants: 1 s (black line) and 5 s (red line) and for two heat losses coefficients: $h = 0$ (solid lines) and $h = 10$ Wm^{-2}K^{-1} (dashed lines). Figure 3.3b shows the temperature profiles using the same thermal conductivity than Figure 3.2b, taking into account the thickness of the sample, $L = 50$ μm, and neglecting heat losses ($h = 0$), with two different values of diffusivity, showing a similar behavior than the thermally thick case (except for the center).
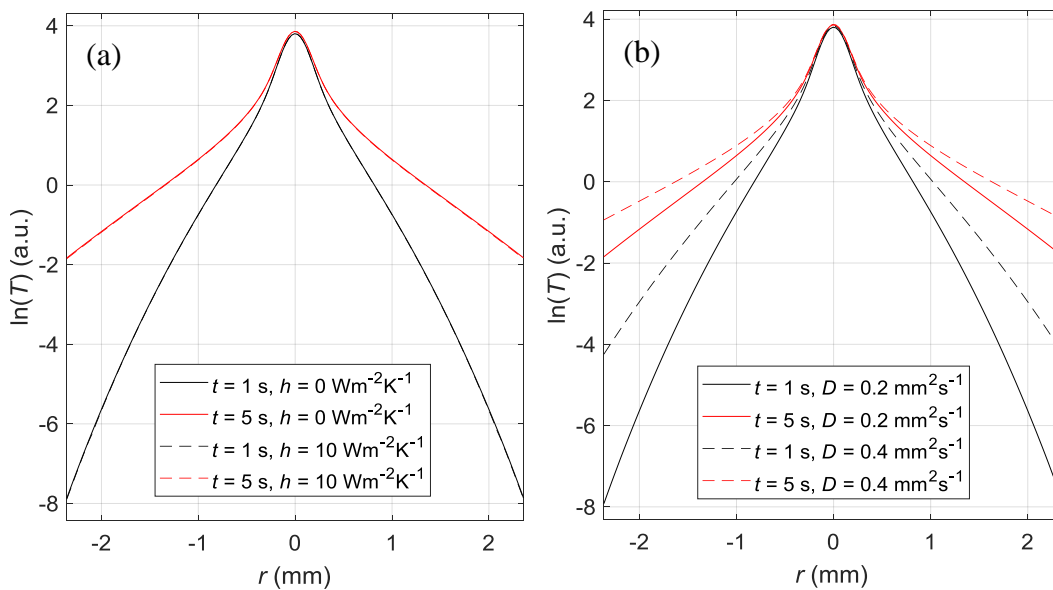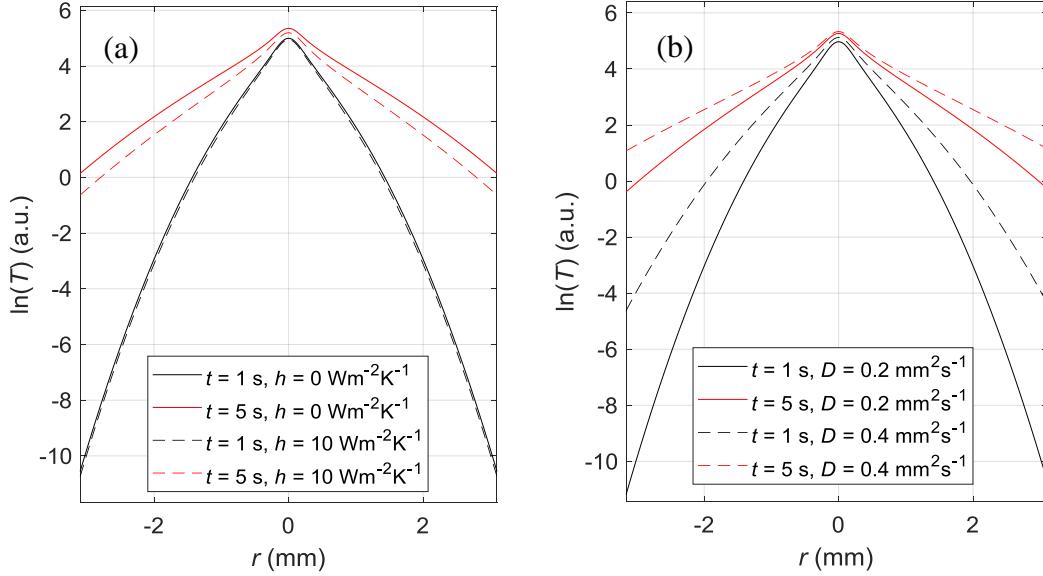

Figure 3.3: (a) Calculations of the temperature profiles ln(T) for an opaque and thermally thin sample ($D = 0.2$ mm^2/s, $K = 0.4$ Wm^{-1}K^{-1}, $L = 50$ μm) at 1 s (black) and at 5 s (red), with different heat losses coefficients: $h = 0$ (solid lines) and $h = 10$ Wm^{-2}K^{-1} (dashed lines). (b) Calculations of the temperature profiles ln(T) for an opaque and thermally thin sample ($K = 0.4$ Wm^{-1}K^{-1}, $L = 50$ μm, h $= 0$ Wm^{-2}K^{-1}) at 1 s (black) and at 5 s (red), with different diffusivities: $D = 0.2$ mm^2/s (solid lines) and $D = 0.4$ mm^2/s (dashed lines).

As we can see in Figure 3.3a, unlike the thick case, the influence of heat losses is important and cannot be neglected, so we will use equation (3.14) to perform the fits on the experimental temperature profiles. The free parameters to fit are, in this case, $\eta P_o/K$,

h/K and D. The first parameter only controls the vertical position of the temperature profile. The other two parameters have an influence in the shape of the curve (the branches, particularly). It is important to know if these two parameters are correlated, or, on the contrary, if they are independent. For this purpose, we define the sensitivity of $\ln(T)$ to a parameter j as

$$S_j = j\, \frac{\partial \ln(|T|)}{\partial j}, \tag{3.17}$$

where j is D or h. The plot of this function illustrates how and where the temperature changes with respect the variation of a parameter. In Figure 3.4 the sensitivities S_D and S_h are plotted for a material with $K = 0.4$ Wm^{-1}K^{-1}, $D = 0.2$ mm^2/s, $L = 50$ μm and $h = 10$ Wm^{-2}K^{-1} at $t = 5$ s. The S_j curves are obtained making small variations on D and h. We changed the sign on S_h so we can compare it to S_D, because the temperature decreases when the heat losses increase. Both sensitivities increase with r but it can be seen that one curve is not proportional to the other, so there is no correlation and when performing the fit we will obtain h and D independently.

Finally, for the highly transparent case, the experimental data will be fitted using equation (3.16) with the same free parameters as in the thin and opaque case but changing α by $1/L$ in the power factor.
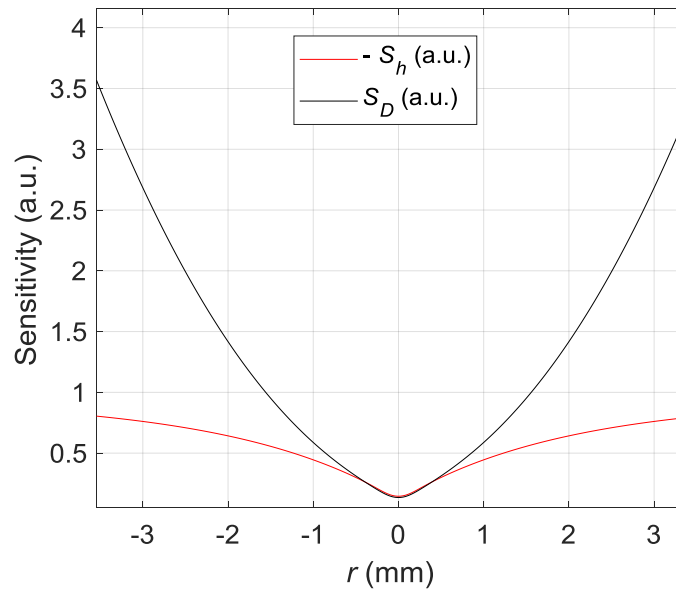
Figure 3.4: Sensitivity of ln(T) to D (black curve) and to h (red curve) for a sample with K = 0.4 Wm^{-1}K$^-$1, D = 0.2 mm^2/s, L = 50 μm and h = 10 Wm^{-2}K^{-1}, at t = 5 s.

3.1.5. Experimental procedure

The experimental setup used in this study is the one described in Chapter 2, Figure 2.1. The laser power that is used varies depending on the sample, and it is always in the range of 10 - 500 mW. The laser is focused onto the sample surface to a radius a = 200 μm. The frame rate is kept constant for all experiments (383 Hz), and the window is set at full frame (320 x 256 px).

The experimental procedure of the step-heating illumination is the following:

- The sample is placed and focused in front of the camera.
- The camera software is prepared and the recording starts before the sample is illuminated.
- The laser is switched on (t = 0 s) and the sample is heated.
- The recording finishes after a sufficient time has passed.

The final result is a movie that contains the evolution of the sample surface temperature as a function of time. However, we are interested in the temperature elevation above the room temperature, so an average of 10 initial frames (that is, frames recorded before the sample is illuminated) is subtracted from the entire sequence. This subtraction is essential because, on one hand, it reduces the effect of emissivity heterogeneities on the surface and, on the other hand, neutralizes the Narcissus effect (see Chapter 2).

In Figure 3.5 four different thermograms are shown, where the $\ln(T)$ is plotted. They correspond to the same sequence: a polymeric sample made of polyether-ether-ketone (PEEK), illuminated with a power $P_o = 10$ mW. Each thermogram corresponds to a different time (1, 2, 5 and 20 s). Note that the color scale on the right of each thermogram has the same limits for all four cases, and therefore, it can be seen that the temperature at the center remains nearly constant, while it rises radially with time on the surroundings of the spot. A natural logarithm representation is used for a better appreciation of low temperature values.
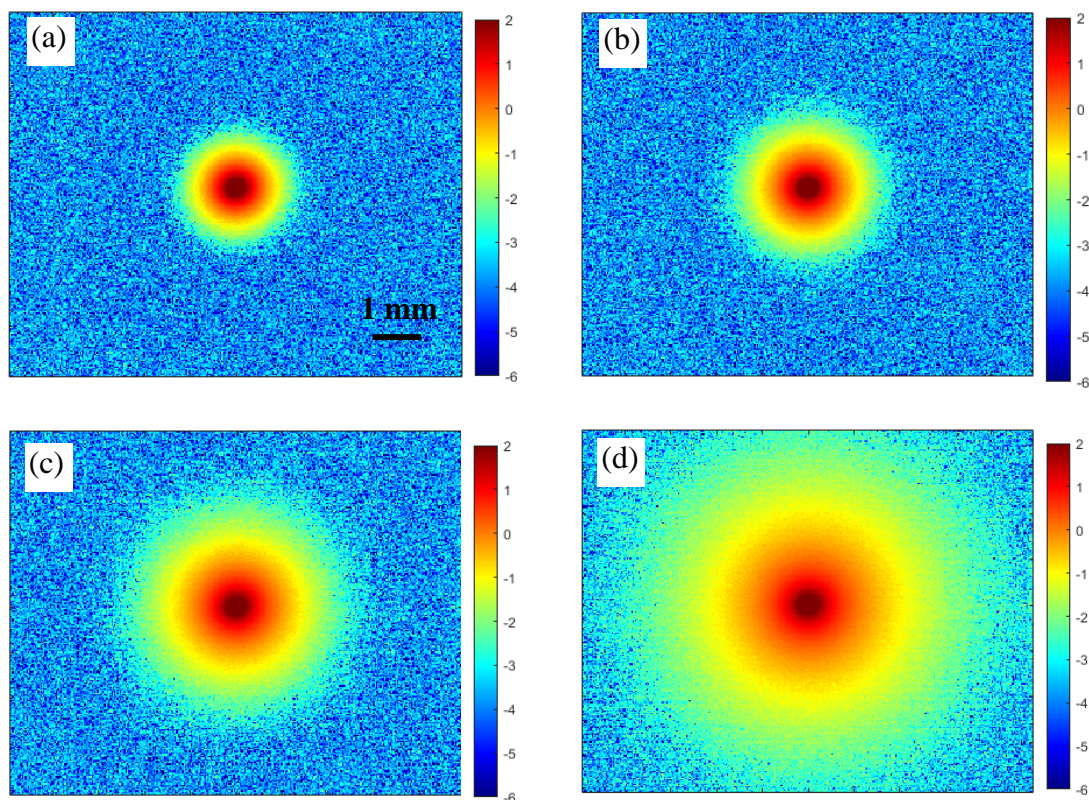

Figure 3.5: Natural logarithm of surface temperature ($\ln(T)$) recorded on a PEEK sample at $t = 1$ s (a), $t = 2$ s (b), $t = 5$ s (c) and $t = 20$ s (d). The scale of the black bar on (a) is 1 mm.

In order to estimate the noise level, the standard deviation of the temperature before $t = 0$ s is calculated, obtaining a value of 29.7 mK, similar to the NETD of the camera (which is 20 mK) as it is expected. If we were performing lock-in measurements, according to equation 2.12 (Chapter 2), using 1500 images in the processing the noise in the amplitude would be approximately 1 mK.

As we are not performing a lock-in analysis in this study, a simple post-processing method that reduces drastically the noise can be applied to the bare thermograms. Taking advantage of the radial symmetry of the problem, a circular average is performed on the thermogram, that is, the pixels that are at a radial distance p are averaged in a single value. A confidence interval of $\pm$ 0.1 pixels is set to avoid intermediate values that could distort the average.

For instance, if a pixel is at a distance $p \pm 0.1$, it is included for the average of the radius p. Let us say we want to average the pixels on the thermogram at radius 30 pixels. Then, all the pixels that are located at a distance 30 ± 0.1 pixels from the center (maximum) are averaged. In Figure 3.6 the image of a thermogram is plotted and, superimposed, four examples of these circles are represented. From the dots in a circle, an average value of T is obtained.

Near the center, the circles are smaller and a small number of pixels are averaged, but it is a region with high SNR, where the temperature is relatively high, so it is not a problem. On the other hand, far away from the center, the temperature is lower and the noise effect is more important, but, as it can be seen, more pixels are averaged.
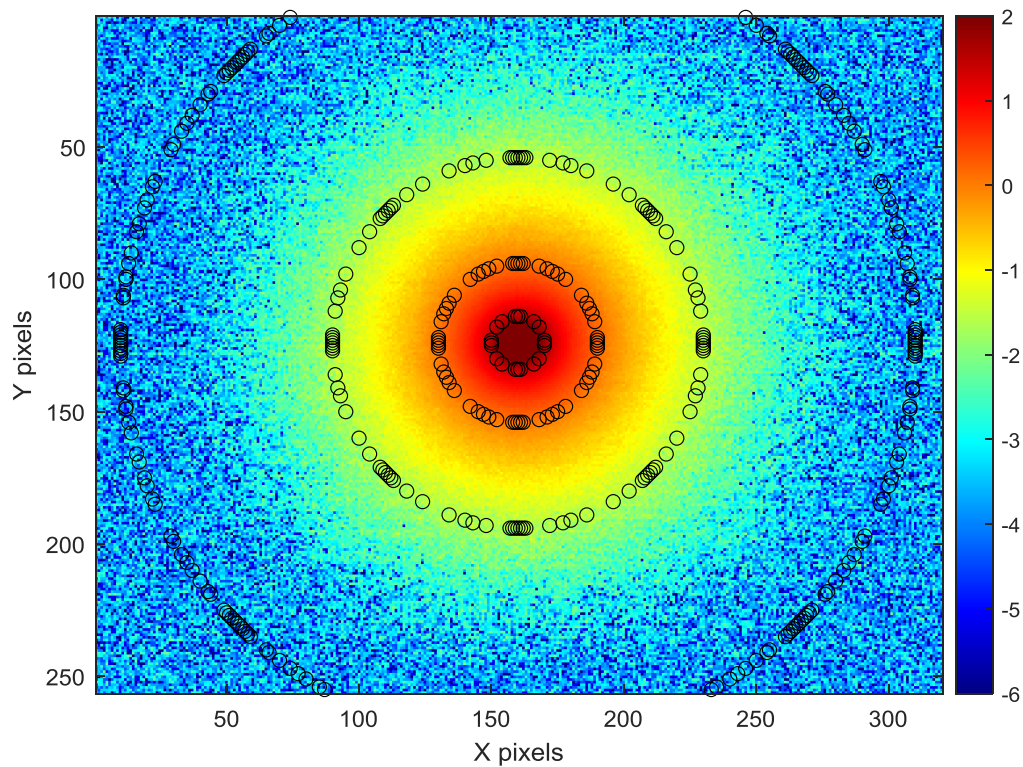
Figure 3.6: Thermogram of Ln(*T*) and selection of pixels for circular average for *t* = 10 s in PEEK. The four circles correspond to radii of 5, 30, 70 and 150 pixels.

In Figure 3.7, using the same PEEK measurement, the horizontal temperature profiles are plotted in red circles for *t* = 2 s and for *t* = 10 s. The black dots represent the averaged profiles for the same instants of time. Although the averaged profiles cover a range of distances starting from *r* = 0 mm, their symmetric reflection is also plotted in order to visualize the comparison.
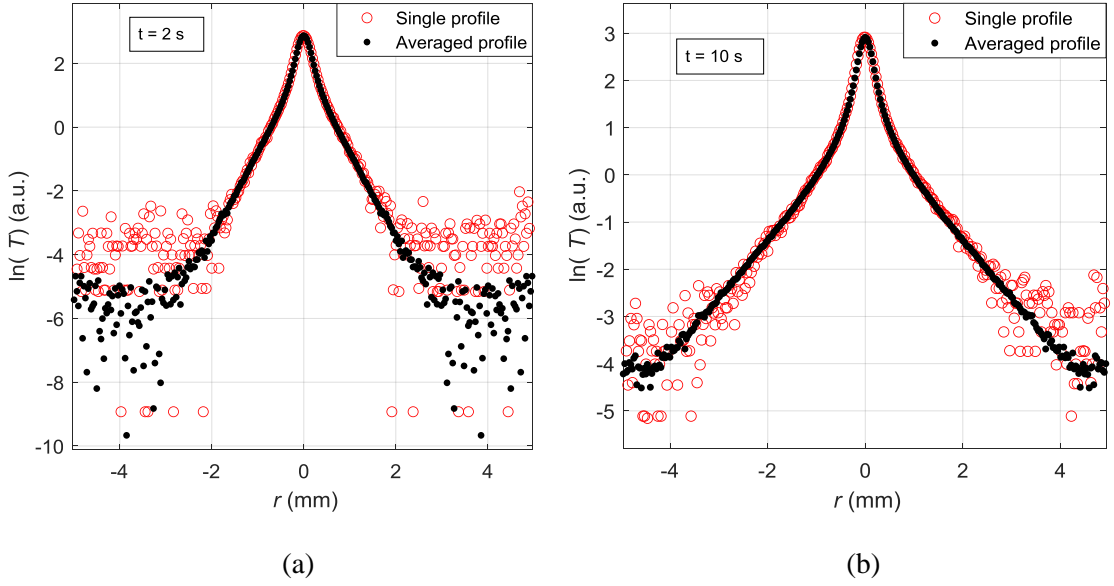
Figure 3.7: Comparison of single and averaged radial profiles of ln(T) obtained at two different times in the PEEK sample. (a) t = 2 s, (b) t = 10 s.

The noise level can be computed as it was done before. Once the circular average is applied we obtain a temperature standard deviation of 3.5 mK for background data, one order of magnitude lower than for the bare thermograms. Furthermore, the lowering of noise can also be seen in Figure 3.7a, where ln(T) ≈ -3 at the non-heated region for the single profile and ln(T) ≈ -5.5 at the same region for the averaged profile.

The averaged radial profiles will be used as the experimental data in the following Section to retrieve the thermal diffusivity of a large variety of samples.

3.1.6. Experimental results and discussion

The samples on which we took data are the following: a PEEK sample (L = 4 mm), two AISI-304 stainless steel plates (one with L = 2 cm and another one with L = 0.2 mm), a vitreous carbon sample (L = 6 mm), a graphite sample (L = 9 mm) and a light blue BK7 glass filter (L = 2 mm). The PEEK sample is covered with a thin graphite layer to enhance the IR emissivity.

The data of the thick and opaque samples (PEEK, vitreous carbon, thick AISI-304, and graphite) are fitted to equation (3.12), having $\eta P_o/K$ and D as the parameters to fit. For the thin AISI-304 plate equation (3.14) will be used, with the fitting parameters being $\eta P_o/K$, D and h/K. Finally, for the transparent filter, the data will be fitted using equation (3.16), having $\eta P_o \alpha/K$, D and h/K as the parameters to fit.

Several averaged profiles at different times are used in the fitting process in order to obtain a reliable value of thermal diffusivity, so it becomes a simultaneous fit of T on the r and t variables. All the profiles are fitted using a least-square fitting function that applies a Levenberg-Marquardt algorithm.

In Figure 3.8 and Figure 3.9 some examples of the simultaneous fits are plotted. In Figure 3.8 we show the thermally thick cases, while in Figure 3.9 the thermally thin and transparent cases are depicted. The figures on the left show the best fit curves for the experimental data from each sample. The lines are the fitted curves and the dots are the experimental data. On the right, the differences between the experimental and fitted data are plotted.

Notice that in the cases of the glassy carbon and the graphite samples, a time $t \approx 0.4$ s was taken as the limit in order to be certain that we are in the thermally thick regime. As it has been explained, a material is considered thick only if $L \gg \mu$, and for times larger than ~0.5 s this condition is not fulfilled for the two samples mentioned above. For the rest of the samples there is no problem with time limitation.
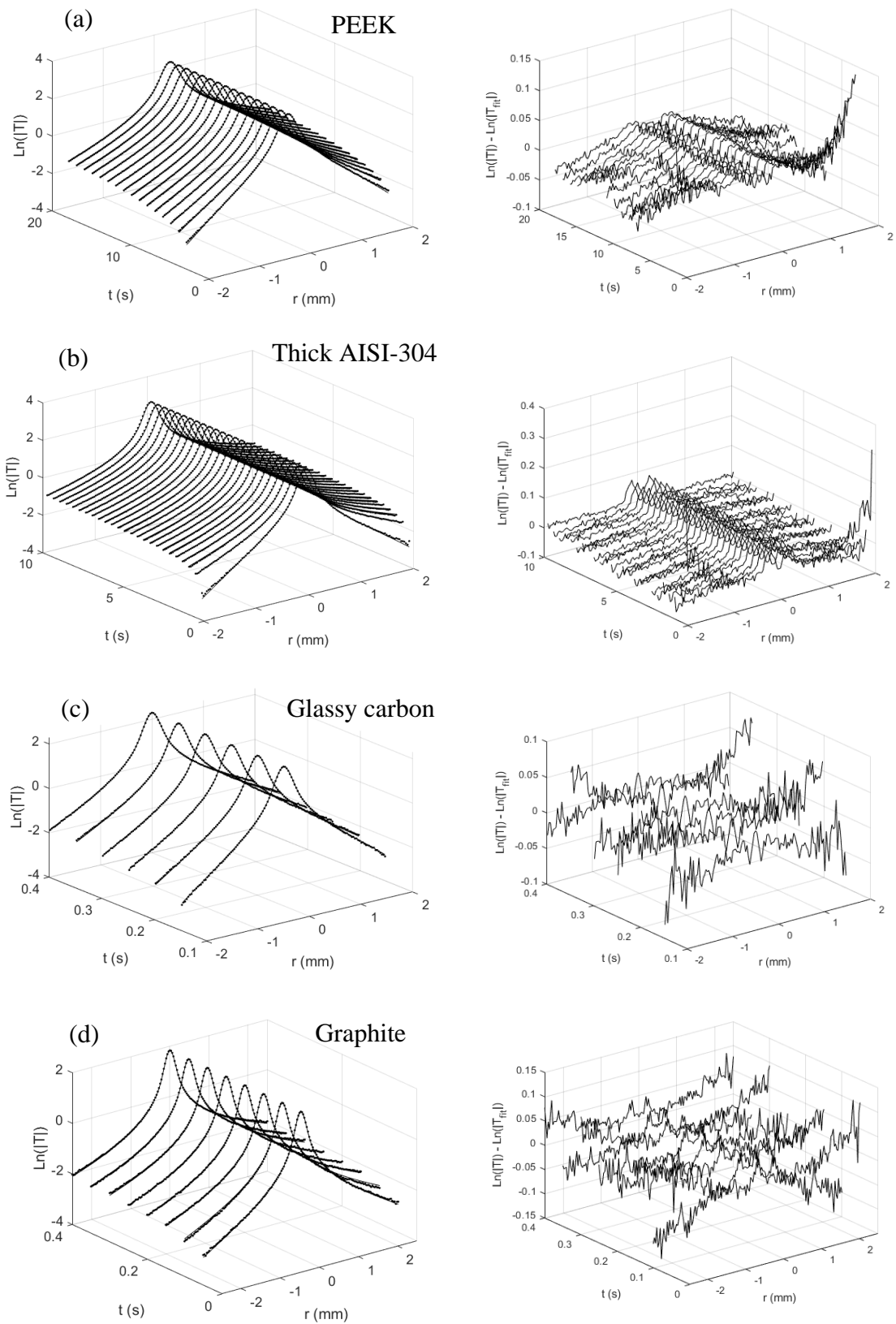
Figure 3.8: Fittings of the temperature profiles and the corresponding residuals for PEEK (a), 2 cm thick AISI-304 (b), glassy carbon (c) and graphite (d).
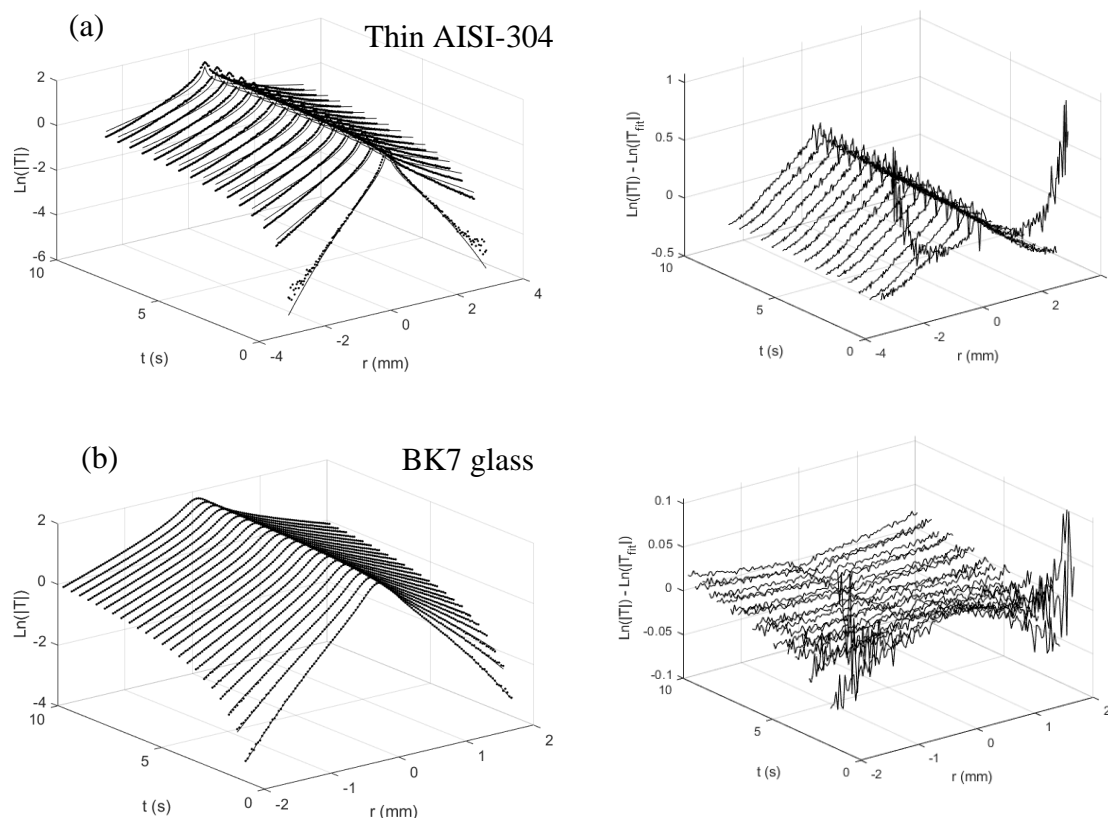
Figure 3.9: Fittings of the temperature profiles and the corresponding residuals for 0.2 mm thick AISI-304 (a) and BK7 glass (b). On the right, the residuals of the fit are plotted.

The parameters obtained for each fitting are shown in Table 3.1. The first four samples are opaque and thermally thick, so the parameter h/K was not included in the fit. The uncertainties on the parameter values obtained for each individual fit are very small (always on the third significant figure), which guaranties an excellent fit quality.

Table 3.1: Results obtained from the multiparametric fits.

Sample	D (mm^2/s)	Power factor (K·m)	h/K (m^{-1})
PEEK	0.207 ± 0.001	$9.79 \times 10^{-3} \pm 2 \times 10^{-5}$	-
AISI-304 ($L = 2$ cm)	3.88 ± 0.02	$6.142 \times 10^{-3} \pm 8 \times 10^{-6}$	-
Glassy carbon	6.16 ± 0.04	$5.11 \times 10^{-3} \pm 2 \times 10^{-5}$	-
Graphite	64.9 ± 0.9	$2.621 \times 10^{-3} \pm 7 \times 10^{-6}$	-
AISI-304 ($L = 0.2$ mm)	3.85 ± 0.06	$9.1 \times 10^{-4} \pm 1 \times 10^{-5}$	1.1 ± 0.2
BK7 glass	0.433 ± 0.001	$1.686 \times 10^{-3} \pm 2 \times 10^{-6}$	5.8 ± 0.5

The measurements were repeated five times at three different sample locations to assess the consistency of the method. The averaged thermal diffusivity values are shown in Table 3.1, along with the respective uncertainties obtained from the different experiments, which in all cases lie between 3-5% approximately. The values are compared with the values found in literature for the same materials, showing a good agreement.

In Table 3.1, the uncertainty (which is around 1% or lower) is associated to only one measurement. On the other hand, the uncertainty obtained in Table 3.2 is statistical, and it is obtained from different measurements, where the sample may have been taken away and placed again to change the measurement region, thus obtaining a higher uncertainty.

Table 3.2: Thermal diffusivity values of the materials measured in this work.

Sample	D (mm^2/s)	D (mm^2/s) Literature [55,58-61]
PEEK	0.20 ± 0.01	0.20
AISI-304 ($L = 2$ cm)	3.9 ± 0.1	4.0
Glassy carbon	6.2 ± 0.2	6.0
Graphite	65 ± 2	60
AISI-304 ($L = 0.2$ mm)	3.9 ± 0.2	4.0
BK7 glass	0.44 ± 0.01	0.4-0.6

3.1.7.   Low-cost equipment viability

The thermal diffusivity of solids has been measured accurately using the step-heating thermography configuration, with the advantage of having a scientific infrared camera and a high-end CW laser. Now, an important question is to check if it is possible to obtain accurate measurements using a low-cost configuration, with a low-end laser and an entry-level camera.

Regarding the laser, the one used in this work can deliver up to 6 W of power, although only a maximum of 0.5 W is used, so a high-end laser is not extremely necessary.

Another concern can be the laser spatial profile. Not all lasers feature a Gaussian profile: low-cost lasers profiles are usually flat-top (equation 3.18), whose Hankel transform is written in equation (3.19) [25].

$$P(r) = \frac{P_0}{\pi a} \Pi \left(\frac{r}{2a} \right) \tag{3.18}$$

$$\hat{P}(\delta) = \frac{P_0}{\pi} \frac{J_1(\delta a)}{\delta a} \tag{3.19}$$

where P_o is the laser power, a is the radius of the top-hat profile, Π is the Heaviside Pi function and J_1 is the first order Bessel function. This new profile can be easily implemented in our model changing the factor $\frac{1}{2} e^{-\frac{(\delta a)^2}{8}}$ by $\frac{J_1(\delta a)}{\delta a}$ in equations (3.11), (3.12), (3.14) and (3.16).

In Figure 3.10 two temperature profiles are compared: one with a Gaussian profile and the other one with a top-hat profile. Both profiles are practically indistinguishable, except at the central region corresponding to the laser spot location. The center is a region of low sensitivity to D and, therefore, the quality of the laser profile does not have an influence in the validity of this method.

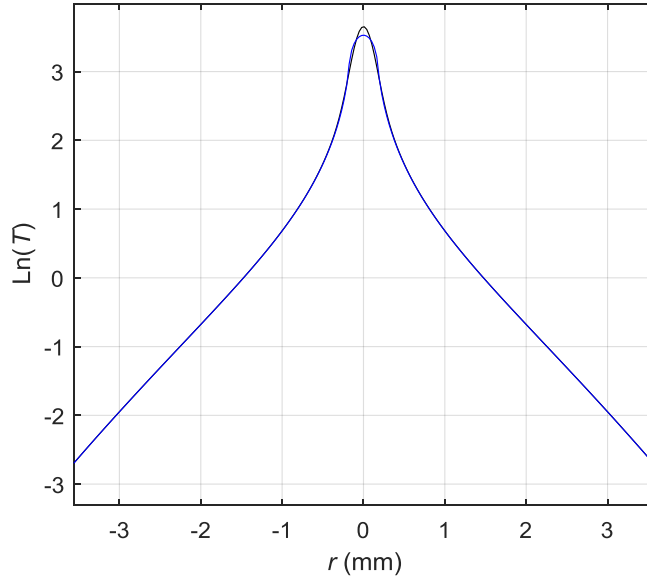**Figure 3.10:** Simulated Ln(T) profiles for a PEEK sample ($D = 0.2$ mm^2/s, $K = 0.25$ Wm^{-1}K^{-1}) with $\eta P_o = 0.05$ W at $t = 10$ s, illuminated by a flat-top (blue) and a Gaussian profile (black) laser spot, both with a radius of $a = 200$ μm.

Concerning the IR camera, several issues need to be discussed. First of all, the noise level of nowadays bolometer cameras, expressed as NETD, is around 50 mK, which is not significantly larger than the NEDT of the used camera (20 mK).

Another important aspect is the spatial resolution, which is worse in low-end cameras, reaching values of 150 μm/px. In order to see how a low spatial resolution would affect the proposed method, a resizing of thermograms is applied to change the resolution by a factor of 5 (from 30 μm/px to 150 μm/px), by performing the temperature average in squares of 5 px × 5 px to simulate a spatial resolution of 150 μm. In Figure 3.11 the averaged profile from a PEEK measurement at $t = 10$ s is plotted in black dots, and the corresponding averaged profile re-processed at 150 μm/px is plotted in blue circles. The change of resolution has no effect on the profiles shape although the reduced resolution one has less experimental data.
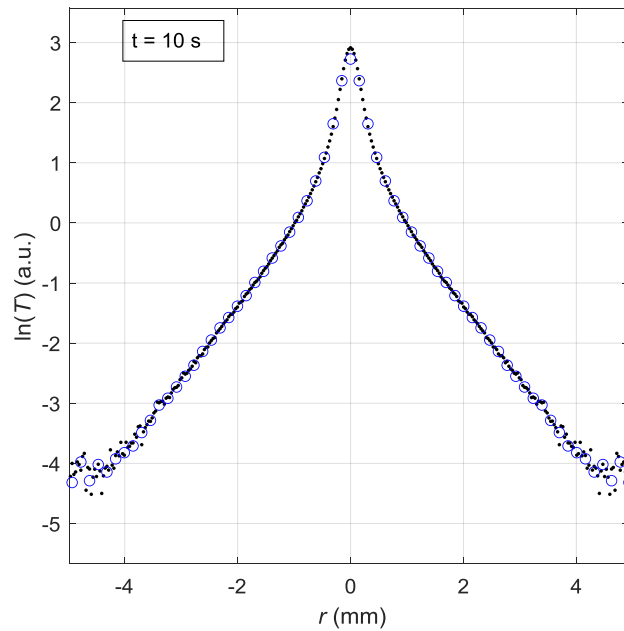
Figure 3.11: Comparison of the averaged profiles of $\ln(T)$ obtained at full spatial resolution (black dots) and at reduced resolution (blue circles).

In Figure 3.12 the fittings of the same temperature profiles as in Figure 3.8a are plotted but with the reduced spatial resolution, and the obtained value of D is 0.207 ± 0.004 mm^2/s, which is consistent with the value obtained in the previous subsection and, although the error is slightly larger, it only corresponds to an uncertainty of 2%. We

have shown the case of a poor thermal conductor as it is the PEEK sample, where the temperature decays faster than in good thermal conductors, to check the viability of the method in a non-expensive camera in a "bad scenario".
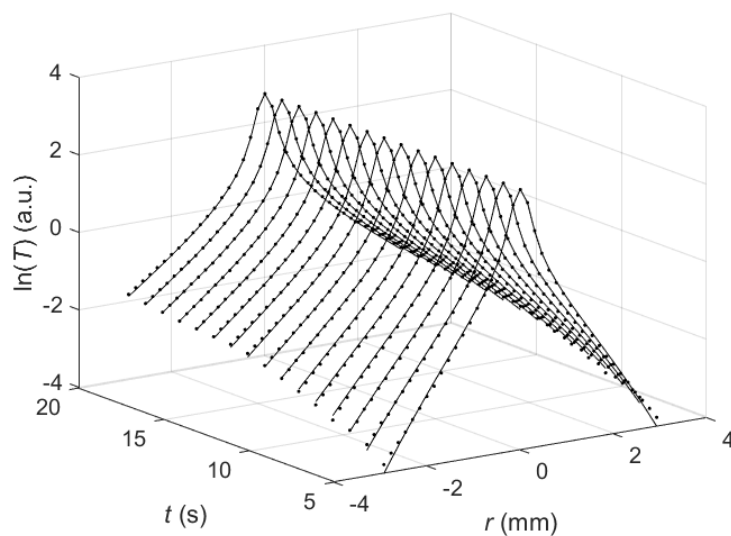
Figure 3.12: Simultaneous fittings of averaged profiles of ln(*T*) with reduced resolution on the PEEK sample.

Finally, another important factor is the uncertainty in the starting time of excitation (our $t = 0$ s). The frame rate used in this work was 383 Hz, so this time uncertainty is less than 3 ms. If the temperature profiles are taken at times longer than 0.1 ms, there is no significant effect ($< 3\%$ in this case, which becomes smaller at longer times). Low-end cameras, however, have a typical frame rate of 50 Hz, so an uncertainty of 20 ms would be introduced. In this situation, only the data taken after 1 s should be used, which is not very restrictive.

In summary, we can conclude that the in-plane thermal diffusivity of solids can be obtained accurately using a low-cost laser-spot step-heating device.

3.1.8.   Conclusions

The objectives of this work have been fulfilled. We have shown that using time domain infrared thermography we can measure the in-plane thermal diffusivity of a large

variety of materials with a laser-spot step-heating configuration. We have obtained very accurate results, with a precision similar to other techniques, like laser-spot lock-in thermography, which is more sophisticated.

The method has been applied on samples with different properties and configurations. We have measured thick and thin samples, and opaque and transparent materials. The evolution of the recorded surface temperature has been fitted to the semi-analytical expressions derived from the heat diffusion equation. The data is pre-processed before the fittings to reduce its noise by averaging the temperature in concentric circles centered on the laser spot. This processing is much simpler than applying a lock-in analysis because there is no need of a modulation device (like a chopper or any other modulator).

In order to gain accuracy and consistency, several averaged profiles obtained at different times are fitted simultaneously. The influence of heat losses by radiation and convection has been analyzed, allowing us to neglect the effect for thick samples and consider its importance on thin materials. The in-plane thermal diffusivity has been measured on materials ranging from poor to good thermal conductors with high accuracy and precision ($< 5\%$).

To conclude, we have shown that a simple laser-spot step-heating configuration, with a low-end IR camera and a low-cost laser, can be used to measure accurately the in-plane thermal diffusivity of materials. This setup does not require sophisticated data processing and can be easily built and used in industrial environments.

3.2. Continuous illumination laser-spot thermography on moving samples

3.2.1. Introduction

A study using laser-spot continuous illumination to measure the in-plane thermal diffusivity on static samples has just been presented. Now we will focus on the case where the sample, to which we want to measure its thermal diffusivity, moves at a certain speed, as it is the case of in-line inspection in factories, where local changes in the thermal properties must be detected without stopping the production chain, in a real time measurement. Laser-spot thermography has been proposed to measure the in-plane thermal diffusivity of samples moving at constant speed [61-64], and an alternative version, where the laser spot scans the static sample (flying-spot thermography), has been used to measure the in-plane thermal diffusivity of big samples that stay at rest [56,65-67].

In the case of continuous illumination of moving samples, it has been demonstrated that there are linear relations between two specific temperature profiles (in the longitudinal and transverse directions with respect to the direction of the sample motion), and the distance to the laser spot [62].The slopes of these straight lines are related to the in-plane thermal diffusivity of the sample, and therefore, this diffusivity can be measured provided the sample speed is known. In the case of anisotropic samples, this method requires not only knowledge of the principal directions but also needs that the sample moves parallel to one of the principal directions. The method was tested by measuring the thermal diffusivity of reference samples. For good thermal conductors this linear

method gave very good results. However, for thermal insulators, no accurate diffusivity values were found (see Table 1 in [62]).

In this section, we will address the problem in a more general form. We will look for an analytical expression for the surface temperature of a sample moving at constant speed when it is illuminated by a tightly focused laser beam, for both isotropic and anisotropic samples. These analytical equations will demonstrate that all radial temperature profiles behave linearly, not just the longitudinal and transverse ones. The slopes of these linear relations satisfy a simple equation that depends on the sample thermal diffusivity and speed, and on the angle of the profile with respect to the direction of the sample motion. Accordingly, we will show that it is possible to obtain the in-plane thermal diffusivity of the sample from a multi-linear fitting of the slopes obtained at several angles, thus reducing systematic errors and achieving better accuracy and precision.

In particular, this method could be especially useful when the material is anisotropic and the directions of the principal axes are unknown. This can be the case in in-line monitoring of industrial anisotropic products in a production chain, for both thermal properties and anisotropy orientation control, when the direction of motion does not necessarily coincide with the direction of the principal axes. In that case, we can obtain the in-plane principal diffusivities together with the orientation of the principal axes.

3.2.2.   Objectives

The main objectives of this work are:

- To improve and generalize a recently introduced method to measure in-plane thermal diffusivity of moving samples using laser-spot continuous illumination.

- To apply this method to a set of calibrated samples: a thermal insulator, a good thermal conductor and an anisotropic composite.

■ To study the capability to retrieve the directions of the principal axes and the values of thermal diffusivity for the case of an anisotropic sample.

3.2.3.   Theoretical analysis

A.   Isotropic samples

Let us start with the case of an isotropic, opaque and semi-infinite in depth material, where the thermal diffusivity is constant in any direction. We will first look for an expression of the surface temperature distribution as a function of time t when a static sample is illuminated by a CW laser beam of radius a, with power P_o, moving at velocity v parallel to the x-axis, as it is depicted in Figure 3.13.
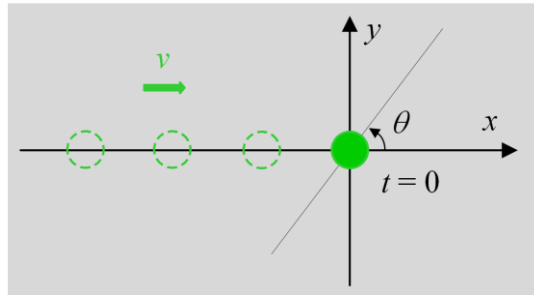
Figure 3.13: Sample surface illuminated by a CW laser spot moving at constant speed v, along the x-axis. The laser is at the origin of coordinates at $t = 0$.

Using this configuration, the surface temperature has the following expression [62]:

$$T(x, y, 0, t) = \frac{2\eta P_o}{e\sqrt{\pi^3}} \int_{t_o}^{t} \frac{1}{\sqrt{t - \tau}} \frac{e^{-\frac{2\left[(x-v\tau)^2 + y^2\right]}{a^2 + 8D(t-\tau)}}}{a^2 + 8D(t - \tau)} \, d\tau \,, \tag{3.20}$$

where η is the power fraction absorbed by the sample, a is the laser-spot radius, D is the thermal diffusivity and e is the thermal effusivity ($e = K/\sqrt{D}$), with K being the thermal conductivity.

If we consider that the laser spot is turned on at $t_o = -\infty$, the steady state is already reached when the laser spot is crossing the origin of coordinates ($t = 0$). We apply these changes on equation (3.20), so we obtain:

$$T(x,y,0,0) = \frac{2\eta P_o}{e\sqrt{\pi^3}}\int_{-\infty}^{0}\frac{1}{\sqrt{-\tau}}\frac{e^{-\frac{2\left[(x-v\tau)^2+y^2\right]}{a^2+8D\tau}}}{a^2-8D\tau}\,d\tau\,. \tag{3.21}$$

If the laser spot size is considered negligible ($a = 0$), the surface temperature expressions is

$$
\begin{aligned}
T(x,y,0,0) &= \frac{2\eta P_o}{e\sqrt{\pi^3}}\int_{-\infty}^{0}\frac{e^{-\frac{(x-v\tau)^2+y^2}{4D\tau}}}{-8D\tau\sqrt{-\tau}}\,d\tau \\
&= \frac{\eta P_o}{2\pi K}\frac{1}{\left|\sqrt{x^2+y^2}\right|}e^{-\frac{v\left(x+\left|\sqrt{x^2+y^2}\right|\right)}{2D}}\,.
\end{aligned}
\tag{3.22}
$$

Changing from Cartesian to polar coordinates, we can obtain the temperature profile along a straight line crossing the origin of coordinates and making an angle θ with respect to the *x*-axis (see Figure 3.13):

$$T(r,\theta,0,0) = \frac{\eta P_o}{2\pi K}\frac{1}{r}e^{-\frac{vr(1+cos\theta)}{2D}}\,. \tag{3.23}$$

According to equation (3.23), the natural logarithm of the product of the temperature and the distance to the laser spot, $\ln(Tr)$, has a linear relation as a function of *r*,

$$ln(Tr) = ln\left(\frac{\eta P_o}{2\pi K}\right) - \frac{v}{2D}(1+cos\theta)r\,, \tag{3.24}$$

and the slope of this linear equation is

$$m_\theta = -\frac{v}{2D}(1+cos\theta)\,. \tag{3.25}$$

The thermal diffusivity can be retrieved accurately by measuring the slope at different angles θ (see Figure 3.13). According to [62], neither the consideration of heat losses by radiation and convection nor the size of the laser spot have any effect on the slope value, so the assumptions of no heat losses and negligible laser spot are totally valid.

According to the relativity principle, the slope equation (3.25) is also valid in the complementary experimental configuration, where the laser is at rest while the sample is moving at constant speed.

B. Anisotropic samples

Now we will consider an anisotropic sample, whose principal axes coincide with the coordinate axes, and a laser beam moving at velocity *v* parallel to the *x* axis. Using the same configuration as before (Figure 3.13), the surface temperature of the sample at time *t* has the following expression:

$$T(x,y,0,t)$$
$$= \frac{2\eta P_o}{e_z \sqrt{\pi^3}} \int_{t_o}^{t} \frac{1}{\sqrt{t-\tau}} \frac{e^{-\frac{2(x-v\tau)^2}{a^2+8D_x(t-\tau)}}}{\sqrt{a^2+8D_x(t-\tau)}} \frac{e^{-\frac{2y^2}{a^2+8D_y(t-\tau)}}}{\sqrt{a^2+8D_y(t-\tau)}} d\tau, \qquad (3.26)$$

where e_z is the thermal effusivity in the *z* direction, and D_x and D_y are the principal diffusivities along the *x*-axis and *y*-axis, respectively. Applying $t_o = -\infty$ and $t = 0$, we get the steady state solution

$$T(x,y,0,0) = \frac{2\eta P_o}{e_z \sqrt{\pi^3}} \int_{-\infty}^{0} \frac{1}{\sqrt{-\tau}} \frac{e^{-\frac{2(x-v\tau)^2}{a^2-8D_x\tau}}}{\sqrt{a^2-8D_x\tau}} \frac{e^{-\frac{2y^2}{a^2-8D_y\tau}}}{\sqrt{a^2-8D_y\tau}} d\tau, \qquad (3.27)$$

and neglecting the laser spot size, we obtain:

$$T(x,y,0,0) = \frac{2\eta P_o}{e_z \sqrt{\pi^3}} \int_{-\infty}^{0} \frac{e^{\frac{(x-v\tau)^2}{4D_x\tau}} e^{\frac{y^2}{4D_y\tau}}}{-8\tau\sqrt{-D_x D_y \tau}} d\tau$$
$$= \frac{\eta P_o}{2\pi e_z} \frac{1}{\sqrt{x^2 D_y + y^2 D_x}} e^{-\frac{v}{2}\left[\frac{x}{D_x} + \sqrt{\frac{x^2 D_y + y^2 D_x}{D_x^2 D_y}}\right]}. \qquad (3.28)$$

The temperature profile along a straight line crossing the origin of coordinates and making an angle θ with respect to the *x*-axis is given by

$$T(r,\theta,0,0) = \frac{\eta P_o}{2\pi e_z} \frac{1}{\sqrt{cos^2\theta D_y + sin^2\theta D_x}} \frac{1}{r} e^{m_\theta r} \,. \tag{3.29}$$

Multiplying this expression by r and applying the natural logarithm, we obtain the linear relation between $\ln(Tr)$ and r

$$ln(Tr) = \ln\left(\frac{\eta P_o}{2\pi e_z} \frac{1}{\sqrt{cos^2\theta D_y + sin^2\theta D_x}}\right) + m_\theta r \,, \tag{3.30}$$

with a slope

$$m_\theta = -\frac{v}{2}\left[\frac{cos\theta}{D_x} + \sqrt{\frac{1}{D_x}\left(\frac{sin^2\theta}{D_y} + \frac{cos^2\theta}{D_x}\right)}\right]. \tag{3.31}$$

As in the case of isotropic samples, if the slope is measured at different angles θ with respect to the direction of movement, the in-plane thermal diffusivities of the sample, D_x and D_y, can be obtained accurately.

Now, let us consider the most general case where the laser spot is moving along a direction making an angle ψ with respect to the principal axis x (Figure 3.14).
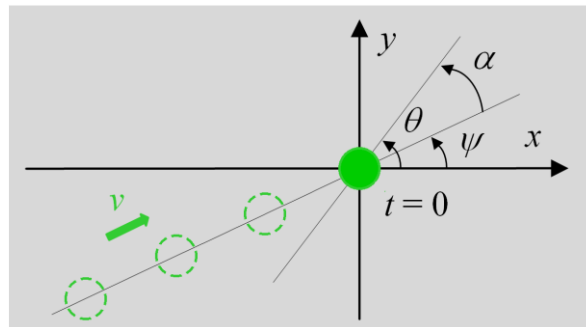

Figure 3.14: Sample surface illuminated by a CW laser spot moving at constant speed v, along a direction making an angle ψ with respect to the x-axis. The laser is at the origin of coordinates at $t = 0$.

In this case, the surface temperature has the following expression:

$$T(x, y, 0, t)$$

$$= \frac{2\eta P_o}{e_z \sqrt{\pi^3}} \int_{t_o}^{t} \frac{1}{\sqrt{t-\tau}} \frac{e^{-\frac{2(x-v\tau cos\psi)^2}{a^2+8D_x(t-\tau)}}}{\sqrt{a^2+8D_x(t-\tau)}} \frac{e^{-\frac{2(y-v\tau sin\psi)^2}{a^2+8D_y(t-\tau)}}}{\sqrt{a^2+8D_y(t-\tau)}} d\tau . \qquad (3.32)$$

Applying $t_o = -\infty$ and $t = 0$, we get

$$T(x, y, 0,0) = \frac{2\eta P_o}{e_z \sqrt{\pi^3}} \int_{-\infty}^{0} \frac{1}{\sqrt{-\tau}} \frac{e^{-\frac{2(x-v\tau cos\psi)^2}{a^2-8D_x\tau}}}{\sqrt{a^2-8D_x\tau}} \frac{e^{-\frac{2(y-v\tau sin\psi)^2}{a^2-8D_y\tau}}}{\sqrt{a^2-8D_y\tau}} d\tau , \qquad (3.33)$$

and neglecting the laser spot size, we obtain:

$$T(x, y, 0,0) = \frac{2\eta P_o}{e_z \sqrt{\pi^3}} \int_{-\infty}^{0} \frac{e^{\frac{(x-v\tau cos\psi)^2}{4D_x\tau}} e^{\frac{(y-v\tau sin\psi)^2}{4D_y\tau}}}{-8\tau \sqrt{-D_x D_y \tau}} d\tau$$

$$= \frac{\eta P_o}{2\pi e_z} \frac{1}{\sqrt{x^2 D_y + y^2 D_x}} e^{-\frac{x D_y v cos\psi + y D_x v sin\psi}{2D_x D_y}} \qquad (3.34)$$

$$\times \, e^{-\frac{\sqrt{v^2(D_x sin^2\psi + D_y cos^2\psi)(x^2 D_x + y^2 D_y)}}{2D_x D_y}} .$$

The temperature profile along an arbitrary line crossing the origin of coordinates and making an angle θ with respect to the *x*-axis is

$$T(r, \theta, 0,0) = \frac{\eta P_o}{2\pi e_z} \frac{1}{r} \frac{1}{\sqrt{cos^2\theta D_y + sin^2\theta D_x}}$$

$$\times \, e^{-\frac{rv}{2}\left(\frac{cos\theta cos\psi}{D_x} + \frac{sin\theta sin\psi}{D_y}\right)} \qquad (3.35)$$

$$\times \, e^{-\frac{rv}{2}\sqrt{\left(\frac{sin^2\psi}{D_y} + \frac{cos^2\psi}{D_x}\right)\left(\frac{sin^2\theta}{D_y} + \frac{cos^2\theta}{D_x}\right)}} .$$

Applying the logarithm at $T \cdot r$ we get the linear expression

$$ln(Tr) = ln\left(\frac{\eta P_o}{2\pi e_z}\frac{1}{\sqrt{cos^2\theta D_y + sin^2\theta D_x}}\right) + m_{\psi,\theta}r, \qquad (3.36)$$

where

$$m_{\psi,\theta} = -\frac{v}{2}\left(\frac{cos\theta cos\psi}{D_x} + \frac{sin\theta sin\psi}{D_y}\right.$$

$$\left. + \sqrt{\left(\frac{sin^2\psi}{D_y} + \frac{cos^2\psi}{D_x}\right)\left(\frac{sin^2\theta}{D_y} + \frac{cos^2\theta}{D_x}\right)}\right). \qquad (3.37)$$

In the case of knowing the orientation of the sample, the angle ψ is known and both thermal diffusivities can be retrieved by measuring the slope of the profiles ln(*Tr*) at different angles θ. A very interesting case, which is of great usefulness, emerges when the directions of the sample principal axes are unknown. In this situation, the angle that will be controlled experimentally as a parameter is α (see Figure 3.14). α is the angle that any selected profile makes with the direction of motion, and by replacing θ by $\psi +$ α, the orientation of the principal axes ψ is measured, along with the diffusivities D_x and D_y.

As in the case of isotropic samples, we have not considered heat losses and a laser spot size as they have no influence on the slopes [62]. Moreover, following the reasoning as in the isotropic case, equations (3.31) and (3.37) are also valid in the configuration where the laser is at rest and the sample is moving at constant speed.

3.2.4.   Numerical calculations

In Figure 3.15 we show the calculations of the isotherms of the natural logarithm of the surface temperature for an isotropic sample ($D = 5$ mm^2/s) when the laser is moving at v $= 5$ mm/s (a), $v = 20$ mm/s (b) and $v = 60$ mm/s (c). The contour plots are symmetric with respect to the *x*-axis. As the velocity increases, the isotherms become more elongated.
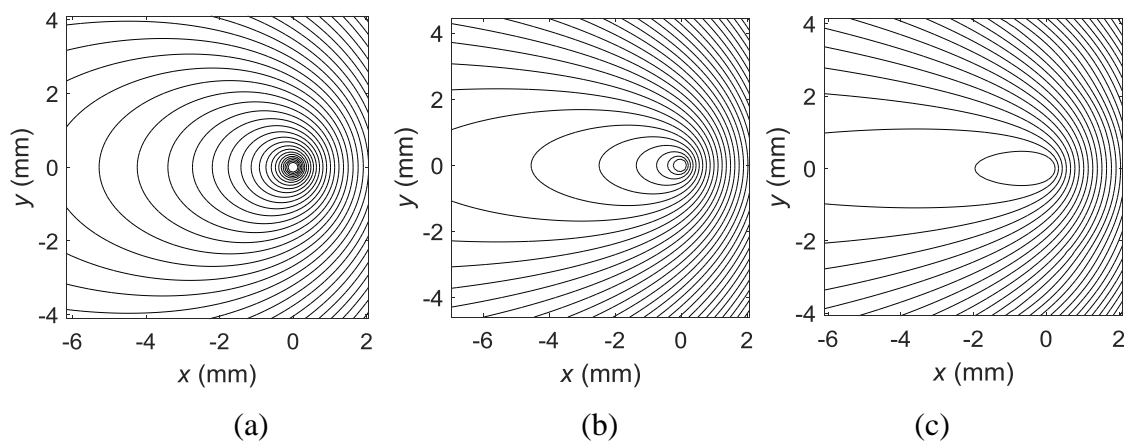
Figure 3.15: Contour plots of ln(T) for an isotropic sample ($D = 5$ mm^2/s), when the laser spot is moving at $v = 5$ mm/s (a), $v = 20$ mm/s (b) and $v = 60$ mm/s (c).

In Figure 3.16 we show the case of an anisotropic sample with the thermal diffusivities in the principal axes being 1 mm^2/s and 5 mm^2/s. In Figure 3.16a the laser is moving along the direction of high diffusivity at $v = 5$ mm/s. In Figure 3.16b the laser is moving along the direction of low diffusivity, at the same speed, and we can see how different the heat diffuses on both cases. As the laser moves parallel to the principal axes, the contour plots are symmetric with respect to this axis.
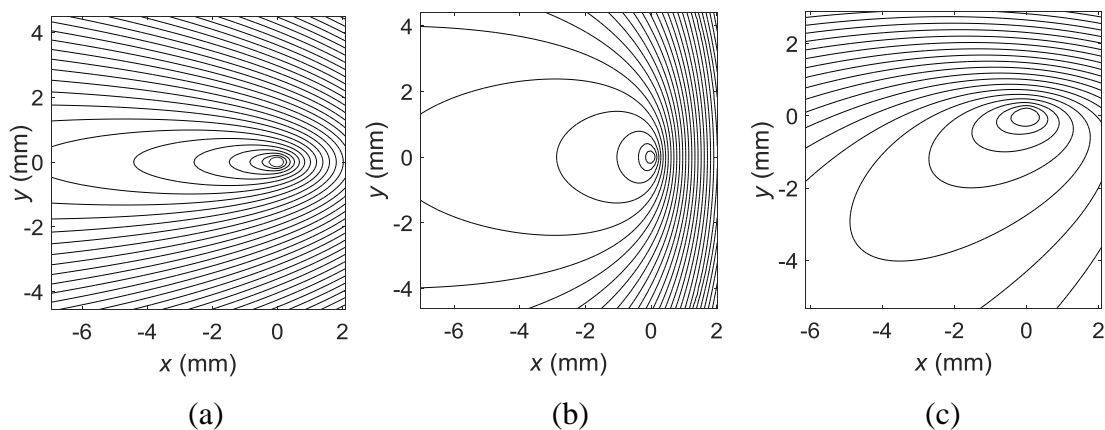
Figure 3.16: Contour plots of ln(T) for a laser velocity $v = 5$ mm/s, with (a) $D_x = 5$ mm^2/s, $D_y = 1$ mm^2/s, laser moving in the direction of high diffusivity, (b) $D_x = 1$ mm^2/s, $D_y = 5$ mm^2/s, laser moving in the direction of low diffusivity, and (c) $D_x = 5$ mm^2/s, $D_y = 1$ mm^2/s and $\psi = 45^{\circ}$.

In Figure 3.16c we show the calculations for the same sample, but now the angle between the laser movement and the *x* principal direction is $\psi = 45°$. As can be observed, the symmetry of the isotherms is broken.

Figure 3.17 shows the behavior of the slope of the temperature profiles for the six cases that have been presented. In Figure 3.17a the curves have been obtained using equation (3.25), and we can see how the absolute value of the slope increases as the velocity rises, although for $\theta = 180°$ it remains constant ($m_\theta = 0$). To calculate the slopes for Figure 3.17b we have used equations (3.31) and (3.37). As it was expected, the symmetry is broken for the case of an angle $\psi \neq 0°$ ($\psi = 45°$ in this case), and the null slope is no longer located at $\theta = 180°$.
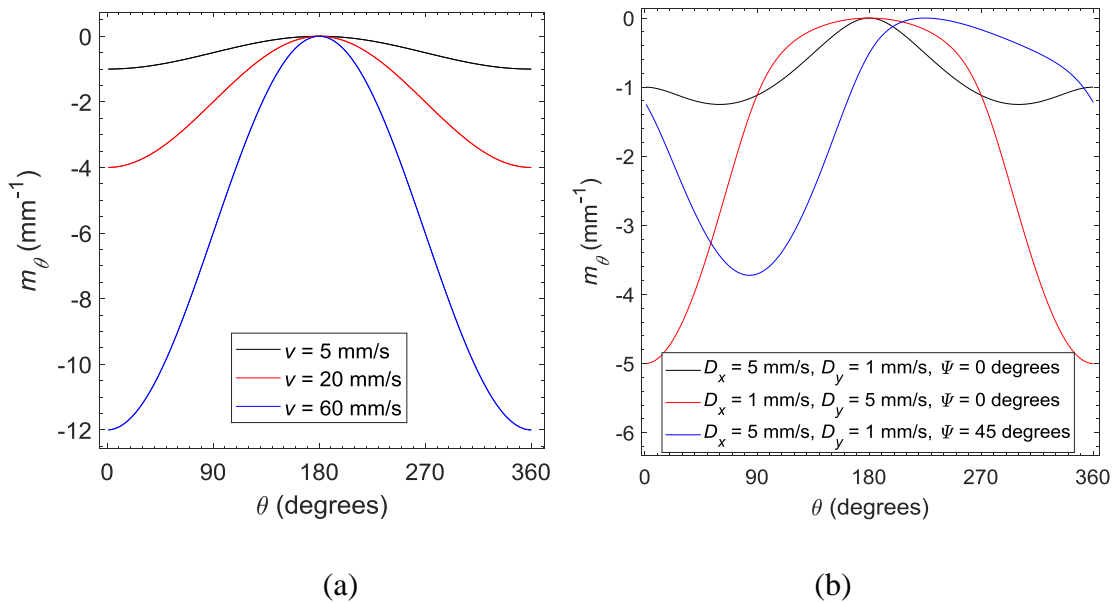
Figure 3.17: (a) Evolution of the slope of ln(*Tr*) for an isotropic sample ($D = 5$ mm/s^2) illuminated by a laser spot moving at $v = 5$ mm/s (black curve), $v = 20$ mm/s (red curve), and $v = 60$ mm/s (blue curve). (b) Evolution of the slope of ln(*Tr*) for an anisotropic sample: $D_x = 5$ mm^2/s, $D_y = 1$ mm^2/s, laser moving in the direction of high diffusivity (black curve); $D_x = 1$ mm^2/s, $D_y = 5$ mm^2/s, laser moving in the direction of low diffusivity (red curve); $D_x = 5$ mm^2/s, $D_y = 1$ mm^2/s and $\psi = 45°$ (blue curve).

3.2.5.   Experimental procedure

The experiments are performed using the setup described in Figure 2.4 (Chapter 2), with no use of an optical chopper, as we need continuous illumination. The CW laser is focused to a radius of about 50 μm. In order to minimize the possible heating of the Ge window by the laser, which would contribute to the observed temperature increase (in addition to the one coming from the sample) the laser remains on for only the few seconds it takes for the sample to cross the field of view (FOV) of the camera. The sample is mounted on the dynamic system, and the procedure explained in Subsection 2.2.2 is followed.

The IR video camera records a film as the sample is moving in front of the camera along the horizontal axis. First, one film is recorded for the moving sample with no excitation (background film), and then another film is recorded for the same movement but with the laser switched on (excited film). The background frames are subtracted from the excited ones, so any background contribution is eliminated (like the Narcissus effect or sample inhomogeneities) and only the temperature rise due to the laser illumination is left. To enhance the signal to noise ratio, we work with a thermogram, which is the average of several hundreds of successive thermograms in the recorded film, after the steady state has been reached. For low velocities, we used a FR of 383 Hz. For high velocities (> 40 mm/s), a window resizing was applied so the FR could be increased.

The sample speed is determined dividing the length of the sample by the time lapse between the entrance and the exit of one end of the sample in the FOV of the camera (number of frames divided by the frame rate of the camera). Proceeding in this way, the sample speed is measured with an uncertainty of less than 0.2%, as the minimum used FR is 383 Hz.

To obtain the ln(*Tr*) profiles at different angles, a simple interpolation has to be performed to the averaged thermogram. In Figure 3.18 we show a simulation of this process. The thermogram is rotated a desired angle, so we only need to pick the temperature values belonging to the black line and multiply them by the distance in order to obtain *Tr*, to which the logarithm is applied. The slope is retrieved from these

profiles performing a linear fit, and the values of the slopes obtained for different profiles are fitted to equations (3.25), (3.31) and (3.37) depending on the case, using a least-square fitting function that applies a Levenberg-Marquardt algorithm. Therefore, the thermal diffusivities can be obtained, as well as the angle ψ if it is the case.
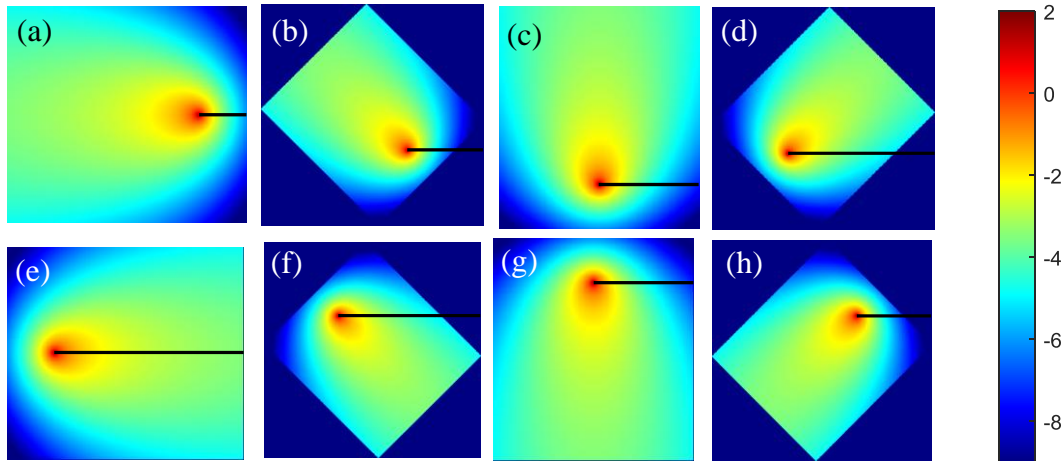

Figure 3.18: Thermogram of Ln(T) for a simulated case (isotropic material, $D = 5$ mm^2/s, $v = 10$ mm/s), original (a) and rotated 45º (b), 90º (c), 135º (d), 180º (e), 225º (f), 270º (g) and 315º (h). The thermograms are plotted at different scales.

3.2.6.   Experimental results and discussion

To test the validity of the method proposed in this work, based on the linear behavior of the temperature profiles, we have performed laser-spot thermography measurements on three samples at several speeds. The first one is an intermediate thermal conductor, stainless steel AISI-304. The second one is a poor thermal conductor, PEEK. The last one is an anisotropic sample, a carbon fiber reinforced polymer (CFRP), which is a composite made of unidirectional carbon fibers embedded in an epoxy matrix. PEEK and AISI-304 samples are covered by a thin graphite layer to enhance both the laser absorption and the emissivity at IR wavelengths.

In the upper row of Figure 3.19 we show the averaged thermograms of ln(T) for an AISI-304 specimen at three sample speeds $v = 5.50$ mm/s, 21.4 mm/s and 81.6 mm/s. As can be observed, the higher the speed, the larger the elongation of the isotherms. In Fig. 3.18a we show the experimental profiles of ln(Tr) versus the distance to the center

of the laser spot for an AISI-304 sample moving at $v = 41.2$ mm/s at several angles θ with respect to the direction of the sample motion. The dots are the experimental data whereas the continuous lines are the best linear fits from which the slopes are obtained. We took data every 10º, i.e. 36 profiles, but for the sake of clarity, only some of them are plotted. Figure 3.19b is the plot of the fitted slopes as a function of the angle θ together with the fitting to equation (3.25). From this fitting a thermal diffusivity value $D = 3.8 \pm 0.2$ mm^2/s is obtained. The errors bars in Figure 3.19b correspond to the standard deviation of the linear fits. We have repeated the same procedure for six sample speeds: 5.50, 10.9, 21.4, 41.2, 60.4 and 81.6 mm/s. The retrieved thermal diffusivity values are summarized in Table 3.3. As can be observed, all of them are consistent and agree very well with the value reported in the literature, within the statistical uncertainty [58]. Note that the uncertainty for the higher speeds is a bit larger due to the lack of spatial resolution of our IR camera. In fact, at high speeds the shape of the thermogram is very elongated and therefore the temperature profiles contain fewer points than at low speeds, which diminish the reliability of the results.
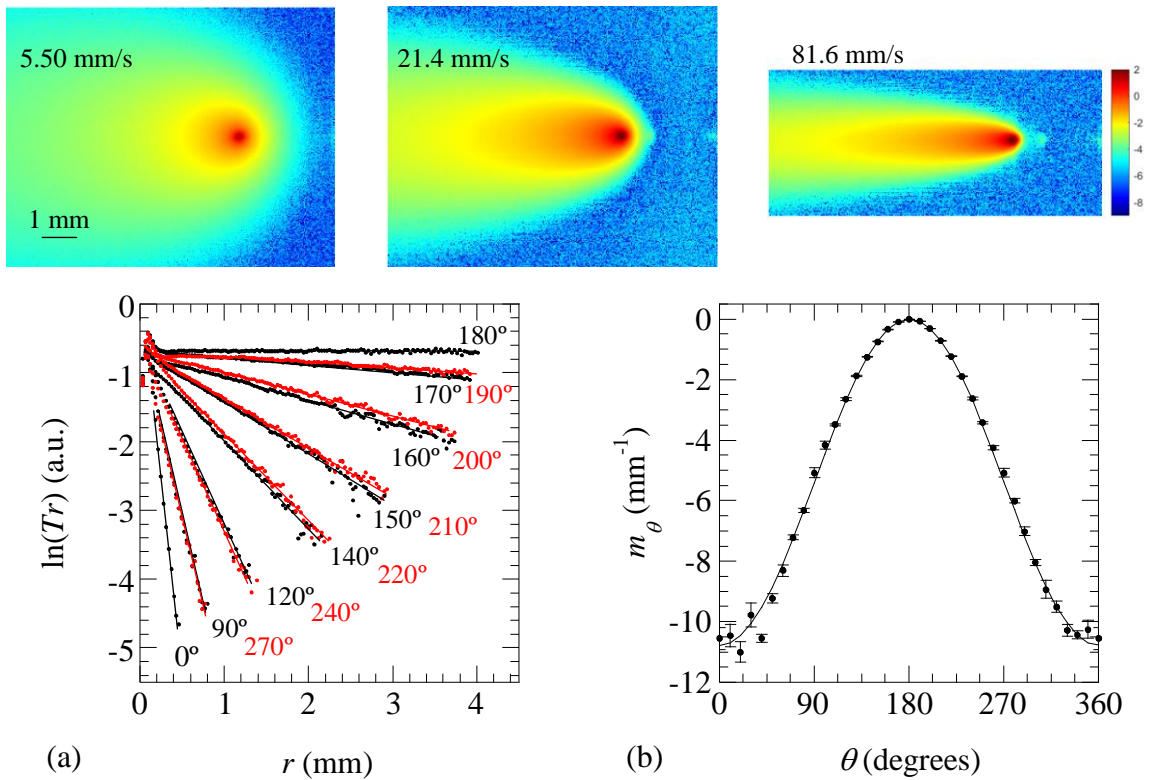
Figure 3.19: Upper row: averaged thermograms of ln(T) for an AISI-304 specimen corresponding to three sample speeds. Lower row: (a) Experimental profiles of ln(Tr) as a function of the distance to the laser spot for AISI-304 at several angles with respect to the direction of the sample motion, for v = 41.2 mm/s. Dots are the experimental data and the straight lines are the linear fits. (b) Experimental slopes versus angle θ corresponding to the linear fits of Figure 3.19a The continuous line is the fit using equation (3.25).

The averaged thermograms of ln(T) for a PEEK plate at v = 0.49 and 4.30 mm/s are plotted in the upper row of Figure 3.20. As the thermal diffusivity of PEEK is about 20 times smaller than that of AISI-304, the PEEK isotherms at 4.30 mm/s are as elongated as AISI-304 at v = 81.6 mm/s. In Figure 3.20a we show the experimental profiles of ln(Tr) as a function of the distance to the laser spot for the PEEK sample moving at v = 1.00 mm/s at several angles θ. The dots are the experimental data and the continuous lines are the linear fits from which the slopes are obtained. Figure 3.20b represents the plot of the fitted slopes as a function of the angle θ together with the fitting to equation (3.25). From this fitting a thermal diffusivity value D = 0.21 ± 0.1 mm^2/s is obtained. The errors bars in Figure 3.20b correspond to the standard deviation of the linear fits.

We have repeated the same procedure for three sample speeds: 0.49, 1.00 and 4.30 mm/s. These results are summarized in Table 3.3. As can be observed, all of them are consistent and agree with the value reported in the literature within the statistical uncertainty [59]. For speeds higher than 5 mm/s the thermogram are so elongated that the temperature profiles contain just a few points, leading to unreliable thermal diffusivity values. Measuring thermal insulators at higher speeds would require a high resolution infrared camera.
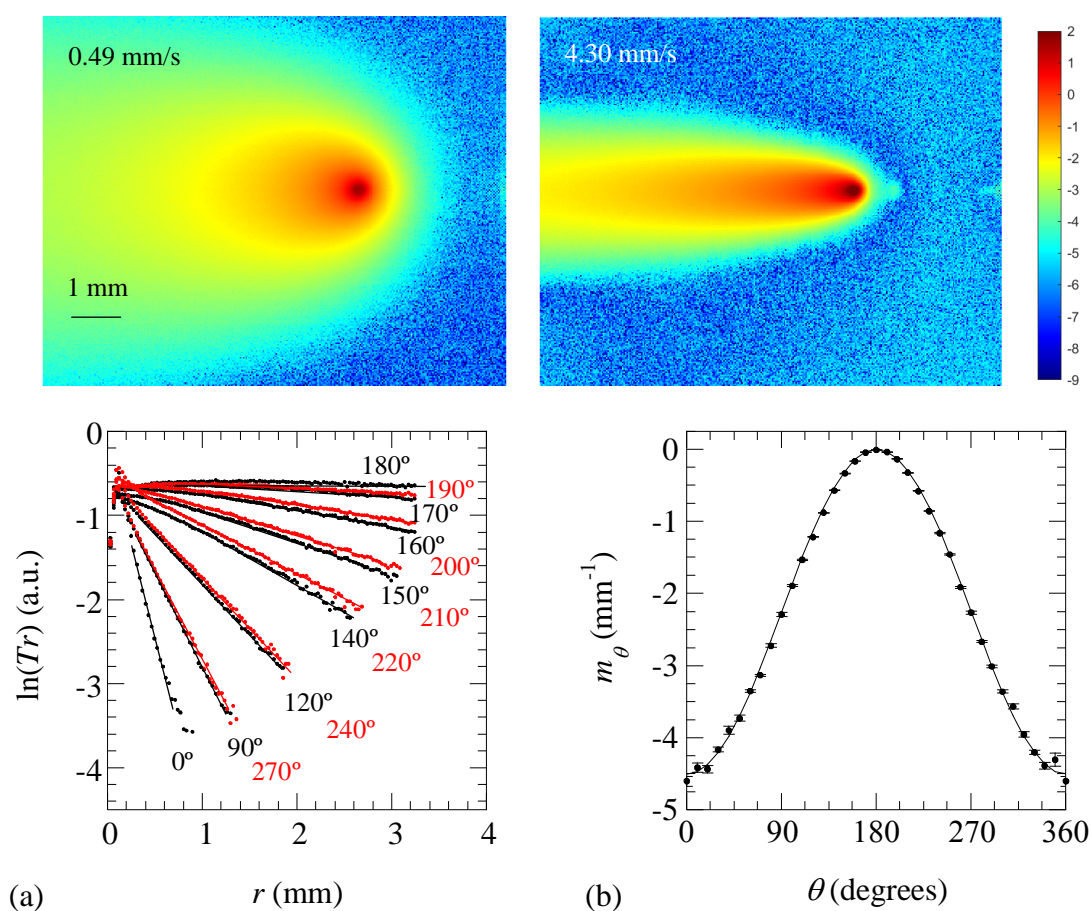
Figure 3.20: Upper row: averaged thermograms of ln(*T*) for a PEEK plate corresponding to two sample speeds. Lower row: (a) Experimental profiles of ln(*Tr*) as a function of the distance to the laser spot for PEEK at several angles with respect to the direction of the sample motion, for *v* = 1.00 mm/s. Dots are the experimental data and the straight lines are the linear fits. (b) Experimental slopes versus angle *θ* corresponding to the linear fits of Figure 3.20a. The continuous line is the fit using equation (3.25).

The results we have obtained for the CFRP are shown in Figure 3.21. In the left column we show the results corresponding to the sample moving in the direction of the fibers and in the right column the results for the sample moving in the direction perpendicular to the fibers. In both configuration the sample is moving at $v = 5.55$ mm/s. In the upper row we plot the averaged thermograms of $\ln(T)$. Note the different shape of the thermograms indicating a high thermal anisotropy. In the middle row we show the experimental profiles of $\ln(Tr)$ as a function of the distance to the laser spot for several angles θ. The dots are the experimental data and the continuous lines are the linear fits from which the slopes are obtained. Finally, in the lower row we plot the fitted slopes as a function of the angle θ together with the fitting using equation (3.31). It is worth mentioning the different shape of both curves, as it was predicted in Figure 3.17b. From each fitting we retrieved the two in-plane principal diffusivities. From Figure 3.21e, we obtained that the diffusivities parallel $D_{//}$ and perpendicular, $D_\perp$ to the fibers are: $D_{//} = 2.8 \pm 0.2$ mm^2/s and $D_\perp = 0.41 \pm 0.04$ mm^2/s, whereas from Figure 3.21f, we got $D_{//} = 2.7 \pm 0.6$ mm^2/s and $D_\perp = 0.49 \pm 0.03$ mm^2/s. These values are consistent and agree with the values obtained using a lock-in laser-spot thermography setup, where the sample remains at rest and is illuminated by a modulated laser beam. Anyway, there is a high uncertainty on the results corresponding to the $D_{//}$ when the sample is moving in the direction perpendicular to the fibers. This drawback is not a limitation of our experimental setup, but it is intrinsic to the linear method as it was confirmed fitting synthetic data with added random noise. We have repeated the same procedure for $v = 2.35$ mm/s. All thermal diffusivity values are summarized in Table 3.3.

Figure 3.21: Upper row: averaged thermograms of ln(T) for a CFRP sample moving at 5.55 mm/s. (a) The sample is moving along the fibers direction, (b) the sample is moving in the perpendicular direction. Middle row: Experimental profiles of ln(Tr) as a function of the distance to the laser spot for CFRP at several angles with respect to the direction of the sample motion. Dots are the experimental data and the straight lines are the linear fits. (c) v is parallel to the fibers, (d) v is perpendicular to the fibers. Lower row: Experimental slopes versus angle θ corresponding to the linear fits of Figure 3.21c and 3.21d. The continuous line is the fit using equation (3.31). (e) v is parallel to the fibers, (f) v is perpendicular to the fibers.

In Figure 3.22 we show the results for the same CFRP plate but moving in two directions not coincident with any principal axis, but making angles $\psi = 30.0 \pm 0.5°$ and $60.0 \pm 0.5°$ between the direction of the sample motion and the fibers. The aim is to obtain simultaneously the two in-plane thermal diffusivities and the angle ψ. In the left column we show the results for $\psi = 30°$ and in the right column the results for $\psi = 60°$. In both orientations the sample is moving at $v = 5.55$ mm/s. In the upper row we plot the averaged thermograms of $\ln(T)$ where the lack of symmetry stands out. In the middle row we show the experimental profiles of $\ln(Tr)$ as a function of the distance to the laser spot for several angles α, which is the angle between the direction of the sample motion and the temperature profile (see Figure 3.14). As in previous plots, dots are the experimental data and the continuous lines are the linear fits from which the slopes are obtained. Finally, in the lower row we plot the fitted slopes as a function of the angle α together with the fitting using equation (3.37). From Figure 3.22e, we obtained $D_{//} = 2.7 \pm 0.2$ mm^2/s, $D_{\perp} = 0.40 \pm 0.04$ mm^2/s and $\psi = 28.6 \pm 1.4°$, whereas from Figure 3.22f, we got $D_{//} = 2.9 \pm 0.4$ mm^2/s, $D_{\perp} = 0.42 \pm 0.03$ mm^2/s and $\psi = 61.0 \pm 1.1°$. The retrieved values of the principal diffusivities are remarkably consistent, and the angles of the fibers directions are measured with very high accuracy.

In Table 3.4 we summarize the results obtained for the principal thermal diffusivities and the orientation of the principal axes for the four orientations of the fibers analyzed in this study, $\psi = 0°$, $30°$, $60°$ and $90°$. The measurements for $\psi = 0°$ and $\psi = 90°$ have been treated in a general way, assuming the orientation is unknown, and the slopes were fitted using equation (3.37), obtaining the diffusivities and the orientation angle.
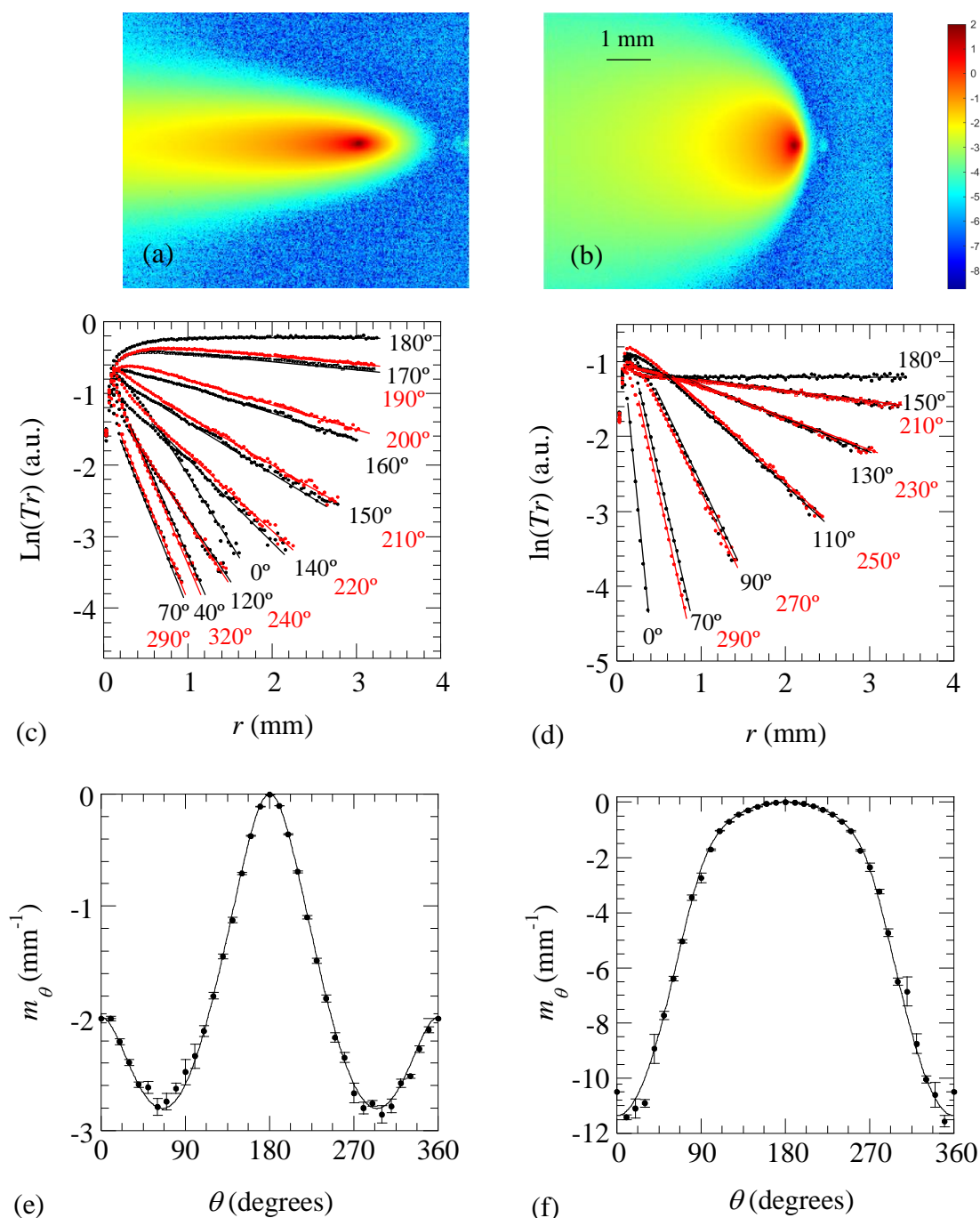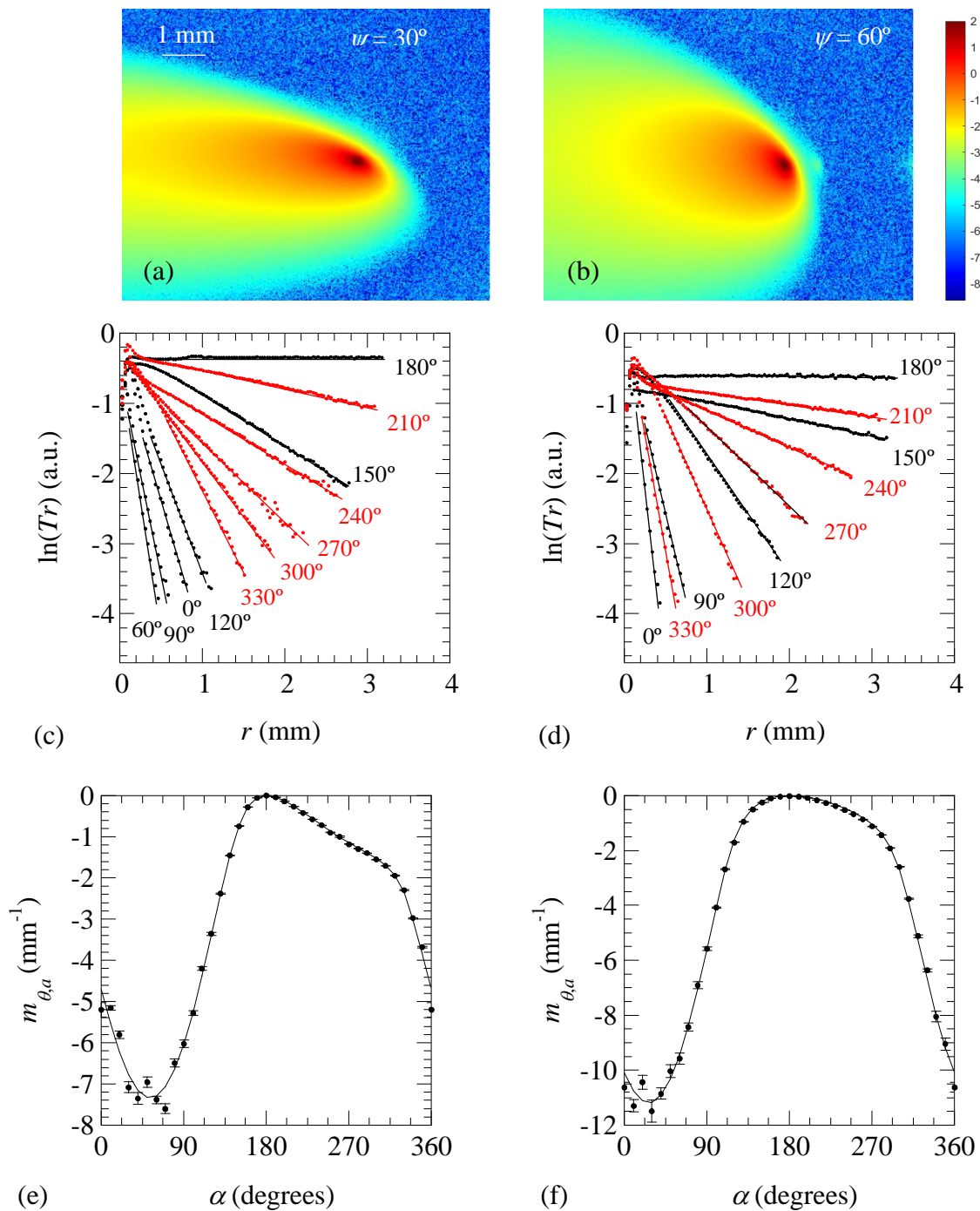
Figure 3.22: Upper row: averaged thermograms of ln(*T*) for a CFRP sample moving at 5.55 mm/s. The sample is moving along a direction making an angle (a) $\psi = 30°$ and (b) $\psi = 60°$ with respect to the fibers. Middle row: Experimental profiles of ln(*Tr*) as a function of the distance to the laser spot at several angles α with respect to the direction of the sample motion for (c) $\psi = 30°$ and (d) $\psi = 60°$. Dots are the experimental data and the straight lines are the linear fits. Lower row: Experimental slopes versus angle α corresponding to the linear fits of Figure 3.22c and 3.22d. The continuous line is the fit using equation (3.37).

The multi-linear fitting proposed in this work makes use of a very high percentage of the information gathered in the thermogram, which reduces eventual systematic errors associated to the evaluation of the thermal diffusivity from two single profiles. These profiles, typically horizontal and vertical, coincide with the structure of the Focal Plane Array of the IR camera, and are more likely to be affected by diffraction effects. Moreover, the proposed approach provides generality, as neither knowledge of the direction of the principal axes nor coincidence of the direction of motion with one of the principal directions is needed. The method is thus significantly more robust, general and powerful than the one described in [62].

Table 3.3: Obtained thermal diffusivity values for the three reference samples analyzed in this study.

Material	v (mm/s)	D (mm^2/s) This study	D (mm^2/s) Literature [58,59]
PEEK	0.49	0.22 ± 0.01	0.20
PEEK	1.00	0.21 ± 0.01	0.20
PEEK	4.30	0.22 ± 0.02	0.20
AISI-304	5.50	3.8 ± 0.2	4.0
AISI-304	10.9	4.1 ± 0.2	4.0
AISI-304	21.4	4.0 ± 0.2	4.0
AISI-304	41.2	3.8 ± 0.2	4.0
AISI-304	60.4	4.1 ± 0.3	4.0
AISI-304	81.6	4.2 ± 0.3	4.0
CFRP	2.35 (∥ fibers)	$D_{//} = 2.9 \pm 0.2$ $D_\perp = 0.39 \pm 0.04$	2.9 ± 0.1 0.40 ± 0.02
CFRP	2.35 (⊥ fibers)	$D_{//} = 2.8 \pm 0.5$ $D_\perp = 0.43 \pm 0.02$	2.9 ± 0.1 0.40 ± 0.02
CFRP	5.55 (∥ fibers)	$D_{//} = 2.8 \pm 0.2$ $D_\perp = 0.41 \pm 0.04$	2.9 ± 0.1 0.40 ± 0.02
CFRP	5.55 (⊥ fibers)	$D_{//} = 2.7 \pm 0.6$ $D_\perp = 0.42 \pm 0.03$	2.9 ± 0.1 0.40 ± 0.02

Table 3.4: Summary of the obtained principal thermal diffusivities and orientation of the principal thermal directions in CFRP moving at 5.55 mm/s for different angles of the fibers with the direction of motion, ψ.

ψ (true)	ψ (measured)	D (mm^2/s) This study	D (mm^2/s) Literature
0º	-0.45 ± 0.2º	$D_{//} = 2.8 \pm 0.2$ $D_{\perp} = 0.41 \pm 0.04$	2.9 ± 0.1 0.40 ± 0.02
30º	28.6 ± 1.4º	$D_{//} = 2.7 \pm 0.2$ $D_{\perp} = 0.40 \pm 0.04$	2.9 ± 0.1 0.40 ± 0.02
60º	61.0 ± 1.1º	$D_{//} = 2.9 \pm 0.4$ $D_{\perp} = 0.42 \pm 0.03$	2.9 ± 0.1 0.40 ± 0.02
90º	89.4 ± 1.1º	$D_{//} = 2.7 \pm 0.6$ $D_{\perp} = 0.42 \pm 0.03$	2.9 ± 0.1 0.40 ± 0.02

3.2.7.   Conclusions

As a summary, we have developed a general, robust and reliable method to measure the thermal diffusivity of samples moving at constant speed using laser-spot thermography with continuous illumination. We have presented analytical expressions of the surface temperature for both isotropic and anisotropic materials illuminated by a tightly focused, continuous-wave laser spot and we have shown that the natural logarithm of the radial temperature profiles (multiplied by the radial distance) fulfill linear relationships with the distance. We have obtained the analytical dependence of the slope of these straight lines with the thermal diffusivity, the speed and the orientation of the profile with respect to the sample motion. The proposed method involves the linear fitting of these radial profiles and the subsequent fitting of the slopes as a function of the orientation of the profile with the direction of motion.

The method is simple as it only involves linear fittings of the temperature profiles crossing the center of the laser spot and an additional simple nonlinear fit. On the other hand, it makes use of the whole surface temperature distribution, which provides robustness against systematic errors, improving the accuracy. Moreover, the signal-to-noise ratio can be enhanced by averaging a number of thermograms, thus improving the precision of the method. The principal diffusivities have been determined with high accuracy and uncertainties of about 5%. Only when the sample moves parallel to the

low diffusivity principal direction, the uncertainty in the high principal diffusivity reaches 20%.

However, the most significant contribution is the treatment of anisotropic materials. The restriction associated to previous methodologies, regarding the need of knowledge of the principal direction but especially the need of coincidence between the direction of the sample motion and one of the principal directions, are not compulsory requirements anymore. Actually, the method is able to identify the principal directions with accuracy of about 1º, which proves a remarkable reliability. This might be significantly useful for in-line quality control of anisotropic products in which the principal directions make arbitrary and unknown angles with the motion of the chain. For instance, the method could be useful for implementing fiber orientation control in CFRP, or for an accurate assessment of homogeneity of the thermal properties of the product.

3.3. Laser-spot Lock-in thermography on moving samples

3.3.1.   Introduction

In the last Section we have seen a method to measure the in-plane thermal diffusivity on moving samples using laser-spot continuous illumination. Now, in this section we will describe a method that uses a similar configuration, as we will also use a focused laser-spot at rest and the sample will be moving. However, now we switch from continuous to modulated illumination, so a lock-in processing can be applied.

The infrared camera measures the temperature oscillations on a sample surface while it is moving at a constant speed. As these oscillations occur at a constant and known frequency, the sequence recorded by the camera can be filtered through a lock-in module, which splits the information into the amplitude and phase components of the temperature and enhances the SNR. The longitudinal and transversal profiles of the amplitude and phase thermograms will be analyzed.

When an appropriate combination of the modulation frequency f and sample speed v is chosen, the thermal diffusivity can be extracted from the linear regions of the amplitude and phase profiles. We will show that the slope of the linear regions is directly related to the frequency, the speed and the in-plane thermal diffusivity.

Through laser-spot lock-in thermography measurements performed on calibrated samples, which cover a wide range of thermal diffusivities and other properties (opacity/transparency and thickness), the validity of these linear methods is confirmed.

3.3.2. Objectives

The main objectives of this work are:

- To design a method to measure in-plane thermal diffusivity of moving samples using laser-spot modulated illumination.

- To apply this method to a large set of calibrated samples, covering a wide range of thermal diffusivity, exploring thick and thin specimens and measuring both opaque and semitransparent materials.

- To study different combinations of sample velocities and modulation frequencies and their effect on the measurements.

- To validate the accuracy of the method comparing the measured diffusivities with tabulated values.

3.3.3. Theoretical analysis

We will start calculating the surface temperature of a homogeneous and isotropic sample moving along the *x*-axis at constant speed *v* when its surface is illuminated by a CW laser of Gaussian profile modulated at a frequency *f* (angular frequency $\omega = 2\pi f$). The geometry of the problem is shown in Figure 3.23.
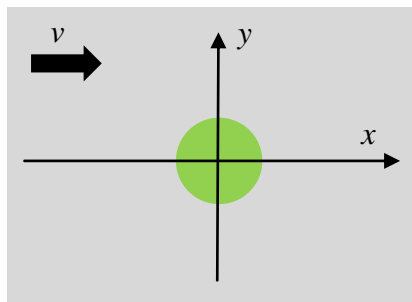

Figure 3.23: Front surface of a homogeneous and isotropic sample, which is illuminated by a Gaussian laser spot. The laser remains at rest at the origin of coordinates, while the sample is moving to the right at constant speed *v*.

We will begin with the expression of the surface temperature of a sample at rest, which is illuminated by a brief laser pulse [55].

$$T(r,t) = \frac{2P_o}{\pi} B(t) \frac{e^{-\frac{2r^2}{a^2+8Dt}}}{a^2+8Dt}, \tag{3.38}$$

where P_o is the laser power, a is the laser spot radius at $1/e^2$ of the maximum intensity and D is the thermal diffusivity. The factor $B(t)$ has a different expression for each case of interest: opaque and thermally thick sample (equation 3.39), opaque and thermally thin sample (equation 3.40) and semitransparent material (equation 3.41).

$$B(t) = \frac{1}{e}\left[\frac{1}{\sqrt{\pi t}} - \frac{h}{e} e^{(h/e)^2} Erfc\left(\frac{h}{e}\sqrt{t}\right)\right], \tag{3.39}$$

$$B(t) = \frac{1}{\rho c L} e^{-\frac{2ht}{\rho c L}}, \tag{3.40}$$

$$B(t) = \frac{\alpha}{\rho c}, \tag{3.41}$$

where e is the thermal effusivity, ρ is the density, c is the specific heat, h is coefficient of heat losses by convection and radiation, L is the sample thickness and α is the optical absorption coefficient at the laser wavelength.

A convolution product of equation (3.38) provides the surface temperature of a moving sample illuminated by a CW laser beam (equation 3.42).

$$T(x,y,t) = \frac{2P_o}{\pi} \int_{t_o}^{t} B(t-\tau) \frac{e^{-\frac{2\{[x-v(t-\tau)]^2+y^2\}}{a^2+8D(t-\tau)}}}{a^2+8D(t-\tau)} d\tau. \tag{3.42}$$

This equation is similar to equation (3.20) (Section 3.2) but for a generalized case. Equation (3.20) is the expression for the particular case of an opaque and thick material, without heat losses. Besides that, the equation only differs on the exponential term $(v\tau \rightarrow v(t-\tau))$, showing that now the sample is moving and the laser is at rest.

If the laser is modulated at a frequency f ($\omega = 2\pi f$), the oscillating component of the surface temperature (from now on, just surface temperature) is:

$$T(x,y,t,\omega) = \frac{P_o}{\pi} \int_{t_o}^{t} B(t-\tau) \frac{e^{-\frac{2\{[x-v(t-\tau)]^2+y^2\}}{a^2+8D(t-\tau)}}}{a^2+8D(t-\tau)} \, e^{i\omega\tau} d\tau \, . \qquad (3.43)$$

The temperature at the sample surface oscillates at the same frequency as the laser spot intensity, and, therefore, it can be expressed as follows:

$$T(x,y,t,\omega) = \theta(x,y)e^{i\omega t} = |\theta|e^{i\varphi}e^{i\omega t} \, , \qquad (3.44)$$

where $\theta(x,y)$ is the spatial distribution of the surface temperature, and it can be split in an amplitude $|\theta|$ with a phase φ. These amplitude and phase are the two magnitudes obtained once a lock-in processing is applied (see Chapter 2, Subsection 2.2.1). We will obtain the spatial distributions of $|\theta(x,y)|$ and $\varphi(x,y)$, and, from them, the different linearities of the temperature profiles will be studied.

3.3.4. Numerical calculations

Figure 3.24 shows the calculations of the contour plots of the natural logarithm of the amplitude (left) and phase (right) of the surface temperature for an opaque and thick AISI-304 stainless steel sample ($D = 4$ mm^2/s and $e = 7500$ Ws$^{0.5}$m^{-2}K^{-1}) that is moving to the right along the x-axis at $v = 30$ mm/s (using the $B(t)$ of equation (3.39), with no heat losses). The surface is heated by a laser spot that remains fixed, centered at the origin of the coordinates, with $P_o = 0.3$ W, $a = 0.2$ mm and $f = 10$ Hz. As can be observed, the amplitude shows the expected elongated shape corresponding to the dragging effect due to the sample movement. On the other hand, the isophases are concentric and equidistant circumferences, as it happens with static samples. This is the first study where such a mismatch between amplitude and phase is found in photothermal science. It was an unexpected behavior, and in the experimental section we will see if it is confirmed by the measurements.
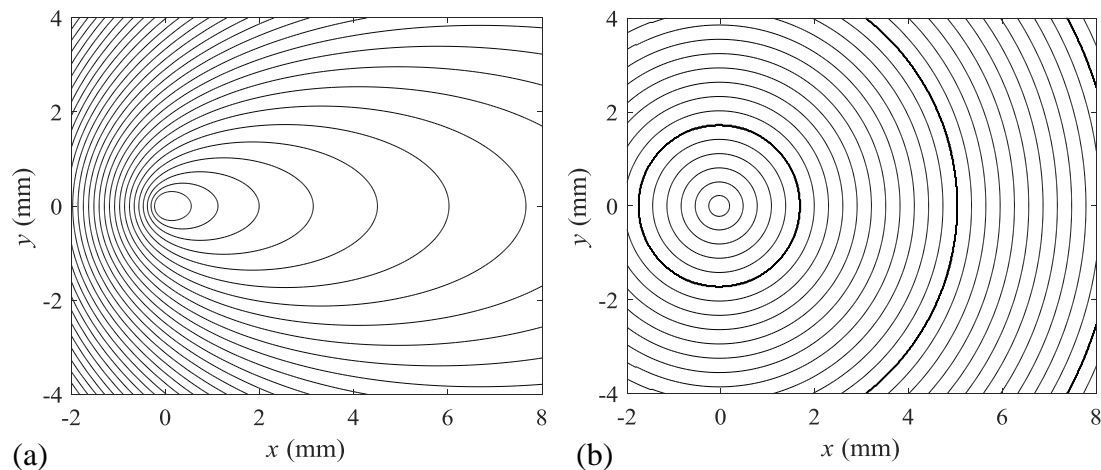
Figure 3.24: Contour plots of the natural logarithm of amplitude $|\theta|$ (a) and phase φ (b) for a semi-infinite AISI-304 sample, using a laser spot of $a = 0.2$ mm modulated at $f = 10$ Hz. The sample is moving to the right at $v = 30$ mm/s.

In order to compare the amplitude and phase profiles with the static case, we have also simulated the same data but with $v = 0$. Moreover, we computed the same calculations for both thermally thin and semitransparent cases. We can see all of these cases in Figure 3.25.

In the left column (Figure 3.25a) we have plotted the temperature and phase profiles along the *y*-axis that cross the center of the laser spot. In the right column (Figure 3.25b) we have plotted the profiles along the *x*-axis. The thermally thick case is shown in the two bottom figures, while the thermally thin and semitransparent cases (these two cases exhibit the same profiles) are shown in the two top figures. Note that to obtain straight lines the temperature amplitude is multiplied by the distance to the centre of the laser spot in the case of opaque and thermally thick samples, and by the square root of this distance in the case of opaque and thermally thin samples and also for semitransparent ones, and, after that, we have to apply the natural logarithm.
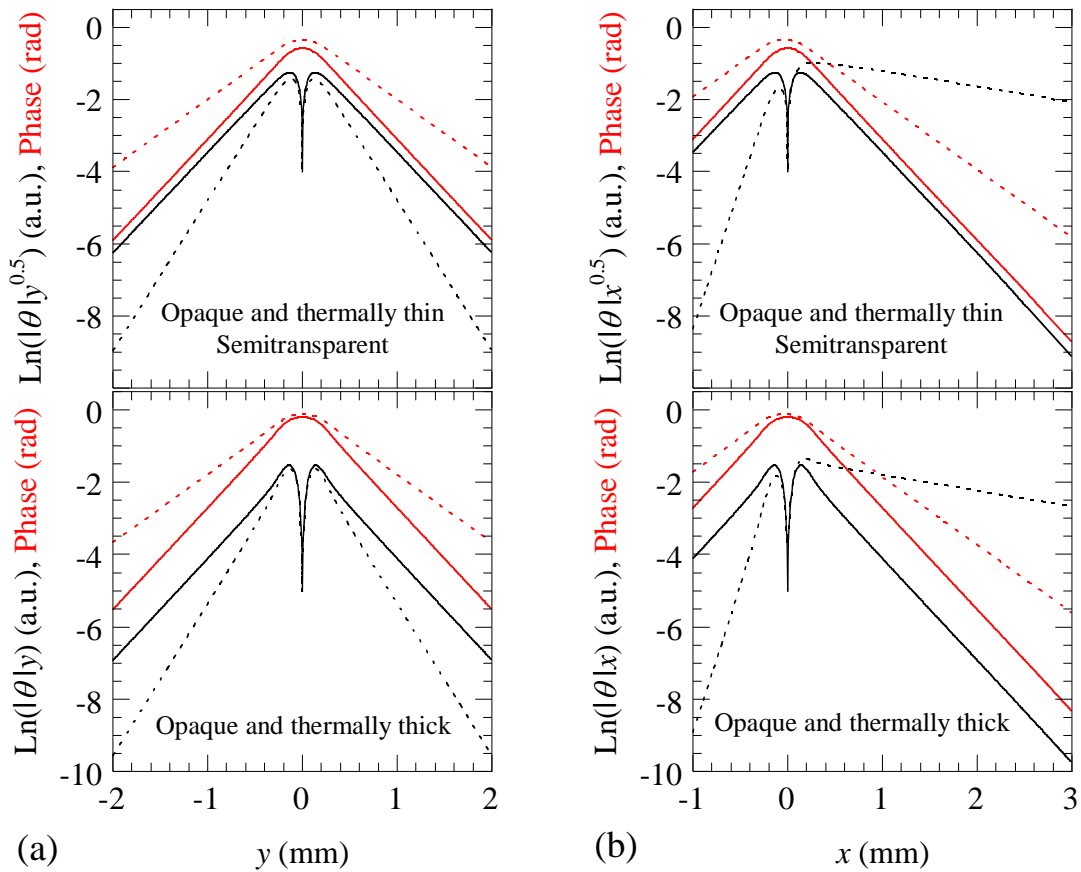
Figure 3.25: Calculations of the amplitude and phase profiles of the surface temperature along the *y*-axis (a) and *x*-axis (b). The bottom row corresponds to an opaque and thermally thick sample. The upper row corresponds to an opaque and thermally thin sample or to a semitransparent sample. Continuous lines: the sample is at rest; dotted lines: the sample is moving at *v* = 30 mm/s. Calculations have been performed for AISI-304 stainless steel (*D* = 4 mm^2/s and *e* = 7500 Ws$^{0.5}$m^{-2}K^{-1}) heated by a laser beam of radius *a* = 0.2 mm modulated at *f* = 10 Hz, in adiabatic boundary conditions (*h* = 0).

We will start analyzing Figure 3.25a. In this figure, continuous lines stand for the sample at rest and they are parallel straight lines whose common slope *m* is directly related to the thermal diffusivity of the sample:

$$m = \sqrt{\frac{\pi f}{D}} \ . \qquad (3.45)$$

These linearities have been used for years to measure the in-plane thermal diffusivity of solid samples [27,26]. On the other hand, dotted lines correspond to the calculations when the sample is moving at $v = 30$ mm/s. As can be seen, the sample movement produces a reduction of the absolute value of the phase slope together with an increase of the absolute value of the amplitude slope with respect to the static case. These differences in the slopes are more pronounced as the sample speed increases. Systematic calculations indicate that the product of both slopes is independent of the sample speed and satisfies:

$$m_{Ln(|\theta|y^n)} \cdot m_\varphi = \frac{\pi f}{D} \, ,$$

(3.46)

where $n = 1$ for opaque and thermally thick samples and $n = 0.5$ for opaque and thermally thin samples and also for semitransparent materials. This equation provides a simple method to measure the thermal diffusivity of moving samples in the transverse direction.

In Figure 3.25b, as we have mentioned, the plotted profiles correspond to the x-axis, which is the direction of the sample movement. As before, continuous lines correspond to the sample at rest and therefore they show the same behavior as the y-axis profiles. Dotted lines correspond to the sample moving at $v = 30$ mm/s. The sample movement produces the same effect on the phase slope as in the y-axis profile. However, the movement produces a reduction of the absolute value of the slope of the amplitude for $x > 0$, but an increase for $x < 0$, with respect to the sample at rest. Numerical calculations indicate that the phase slope satisfies the following expression, with an error smaller than 1%:

$$m_\varphi = \sqrt{\frac{\pi f}{D}} \sqrt{\frac{31.90}{31.90 + \left(\frac{v^2}{Df}\right)^{1.1813}}} \cdot$$

(3.47)

Furthermore, the slope of the right branch of the amplitude verifies the following equation, within the same uncertainty of 1%.

$$m_{Ln(|\theta|y^n)} = \sqrt{\frac{\pi f}{D}}\; e^{-\frac{\pi}{10}\left(\frac{v^2}{Df}\right)^{0.55}} \;.$$

(3.48)

The linear relations given in equations (3.46), (3.47) and (3.48) are obtained assuming that the sample has reached the steady state ($t = \infty$). In order to apply those linear relations to obtain the thermal diffusivity of moving samples, we have analyzed which is the minimum time after switching on the laser (t_{min}) required for the sample to reach the steady state. As t_{min} depends on the distance to the laser spot (the larger this distance, the longer t_{min}) we took as reference a distance ten times larger than the thermal diffusion length, 10μ, with $\mu = \sqrt{\frac{D}{\pi f}}$. We considered that the sample has reached the steady state when the temperature differs by less than 0.1% with respect to the temperature at $t = \infty$. In Figure 3.26 we show the numerical calculations of t_{min} as a function of the sample speed. We considered thermal diffusivity values covering a wide range from thermal insulators to good thermal conductors.

It is worth noting that for a given couple (D,v) t_{min} is independent of the modulation frequency. As can be observed, when the velocity is increased, a shorter t_{min} is needed. Actually, it is well known that for samples at rest, the laser must be switched on for several minutes before conducting modulated experiments. Moreover, the steady state is reached faster for thermal insulators than for good thermal conductors. Anyway, for speeds of several cm/s, which are those expected in real applications in in-line production in factories, the steady state is reached in few seconds.
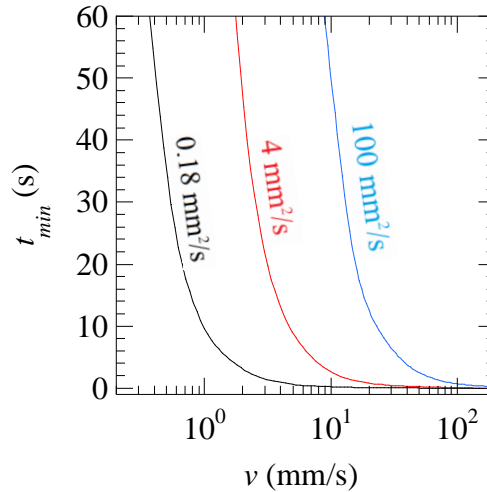
Figure 3.26: Numerical calculation of the minimum time needed for the sample to reach the steady state once the laser is switched on, as a function of the sample speed. Calculations are performed for three different thermal diffusivity values: 0.18 mm²/s (black curve), 4 mm²/s (red curve) and 100 mm²/s (blue curve).

In order to study the accuracy of the thermal diffusivity values obtained from the linear relations corresponding to equations 3.47 and 3.48, we analyzed the sensitivity of these equations to the thermal diffusivity. In particular, we evaluated how the error in the slope, Δm, is transmitted to an error in the estimated diffusivity, ΔD. The results for equation (3.47), corresponding to the phase slope, are shown in Figure 3.27a. Different calculations were performed for several values of the dimensionless factor v^2/Df. As can be observed, the best situation occurs when this factor is very small i.e. when the sample is at rest or moving at very low speed or the modulation frequency is very high. In this case $\Delta D = 2\ \Delta m$. As the factor increases, the error in diffusivity significantly increases. For instance, for $v^2/Df = 25$, $\Delta D \approx 6.5\ \Delta m$, but for $v^2/Df = 64$ then $\Delta D \approx 50\ \Delta m$. These results indicate that the reliability of the slope method to obtain D decreases as the dimensionless factor increases. Consequently, we established an upper limit for this factor: the method is valid provided $v^2/Df < 25$. According to this limit, reaching high speeds requires using high enough frequencies. This is easy to fulfill in the case of good thermal conductors, but in the case of thermal insulators the modulation frequency is limited by the spatial resolution, so for insulators it is difficult to work at $v > 10$ mm/s.

We performed the same analysis for equation 3.48, which corresponds to the amplitude slope. The results are shown in Figure 3.27b. As can be seen, even for very small values of the dimensionless factor the error in diffusivity is huge. Accordingly, we will not consider the amplitude slope to measure the thermal diffusivity of moving samples.
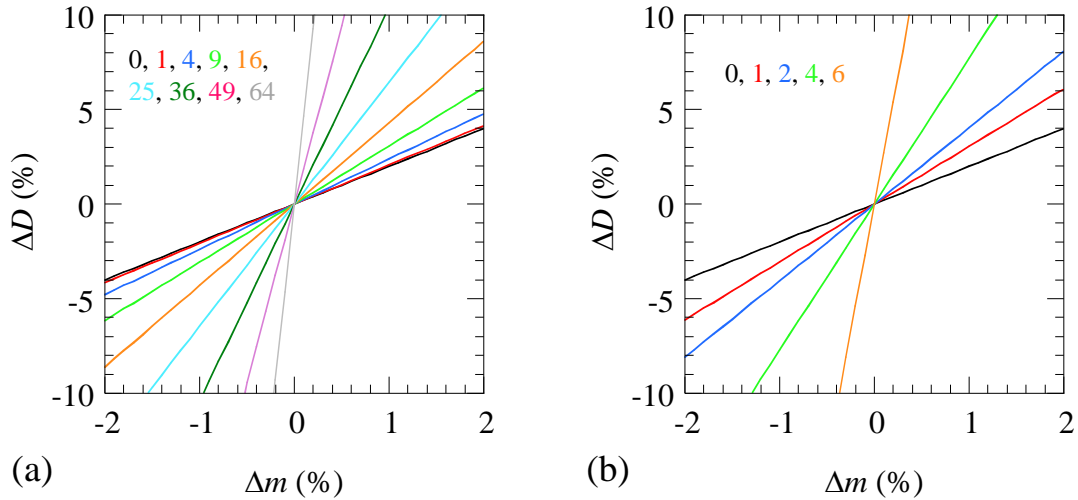

Figure 3.27: (a) Numerical calculation of the error transmission from phase slope to thermal diffusivity value according to equation 3.47. Calculations are performed for several values of the factor v^2/Df. (b) The same for equation 3.48, corresponding to the amplitude slope.

Finally, we studied the effect of heat losses due to convection and radiation on the linear relations we propose to measure the in-plane thermal diffusivity of moving samples. According to equation (3.39), which corresponds to opaque and thermally thick samples, the coefficient of heat losses is correlated to the sample effusivity. This means that the effect of heat losses is more pronounced for poor thermal conductors than for good thermal conductors, as is also the case in a static situation. On the other hand, the effect of heat losses increases at low frequencies and/or low sample speeds. Numerical calculations indicate that in the presence of heat losses the linearity of the amplitude and phase profiles is preserved, but the slopes given by equations (3.46), (3.47) and (3.48) are slightly modified. Anyway, for realistic values of the coefficient of heat losses at room temperature (h = 10 - 15 Wm^{-2}K^{-1}) [46] and sample speeds higher than 4 mm/s, the influence of heat losses on the retrieved thermal diffusivity is negligible.

In the case of opaque and thermally thin samples the coefficient of heat losses is correlated to the product $\rho c L$ (equation 3.40). As the heat capacity in solids (ρc) is bounded between 10^6 and 4×10^6 $Jm^{-3}K^{-1}$ [23], the effect of heat losses mainly depends on the sample thickness and therefore it could be significant in the case of very thin samples. However, numerical calculations show that heat losses reduce the phase slope and increase the amplitude slope, in such a way that the product of slopes still satisfies equation 3.46, as it also happens in the case of thin samples at rest [44,47]. Finally, in the case of semitransparent samples the surface temperature is not affected by heat losses as can be seen in equation 3.41.

3.3.5.   Experimental procedure and results

The experiments are performed using the setup described in Figure 2.4 (Chapter 2), making use of both the optical chopper and the moving cart. The laser is focused to a radius of $a \sim 200$ μm. The sample is mounted on the dynamic system, and the procedure explained in Subsection 2.2.2 is followed.

The camera records a sequence of frames as the sample is moving along the horizontal axis. First, one film for the moving sample with no excitation (background film) is recorded, and then another film for the same movement but with the laser switched on (excited film) is recorded. The background frames are subtracted from the excited frames, so any background contribution is eliminated (like the Narcissus effect or sample surface inhomogeneities) and only the temperature rise due to the laser illumination is left. A lock-in module processes the recorded film and transforms it into the two thermograms of interest: amplitude and phase.

For low velocities, we used the maximum FR available at full windowing (383 Hz). For high velocities, a window resizing was applied so the FR could be doubled up.

The samples have a typical length of 20-30 cm, and the modulated laser illuminates them at all times while they are moving. In order to guarantee that the steady state has been reached, only the frames recorded during the passage of the second half of the sample in front of the camera are analyzed in the lock-in process. In any case, we wait

approximately a time t_{min} (explained in the numerical calculations) since the beginning of excitation until we start to take the frames to ensure we are in the steady state regime.

As in Section 3.2, the sample speed is determined dividing the length of the sample by the time lapse between the entrance and the exit of one end of the sample in the FOV of the camera. Proceeding in this way, the sample speed is measured with an uncertainty of less than 0.2%, as the minimum used FR in this study is 383 Hz.

In Figure 3.28 we show an example of a measurement. It is the result of a lock-in analysis of a PEEK sample which is moving to the right at 9 mm/s while it is being illuminated by a laser beam modulated at a frequency of 6 Hz. As can be observed, the amplitude shows an elongated shape due to the dragging effect produced by the sample movement. The phase, on the contrary, exhibits a symmetric shape, i.e. the isophases are concentric and equidistant circumferences. This experimental result corroborates the unexpected result obtained in the numerical analysis.
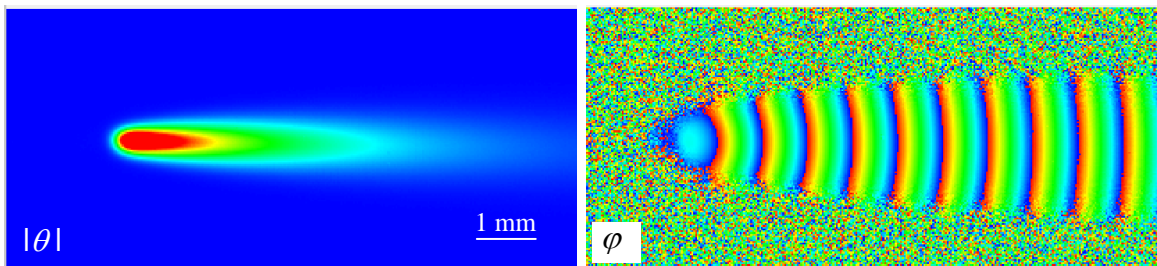

Figure 3.28: Experimental thermograms of the amplitude (left) and phase (right) of the surface temperature for a PEEK sample moving to the right at v = 9 mm/s when it is illuminated by a laser spot of radius a = 0.2 mm modulated at f = 6 Hz which remains at rest.

The parameters of the measurement shown in Figure 3.28 lead to a factor v^2/Df = 67.5, so this experiment is not used to retrieve the thermal diffusivity. In Figure 3.29 we show another example, in this case for an AISI-304 sample which is moving to the right at 10 mm/s while it is being illuminated by a laser beam modulated at a frequency of 2.7 Hz. The amplitude thermogram has an elongated shape, but not as exaggerated as in the PEEK measurement. In the phase thermogram we can clearly see the circular behavior. Here, the factor v^2/Df is 9.26, so the thermal diffusivity can be determined using equation (3.47).
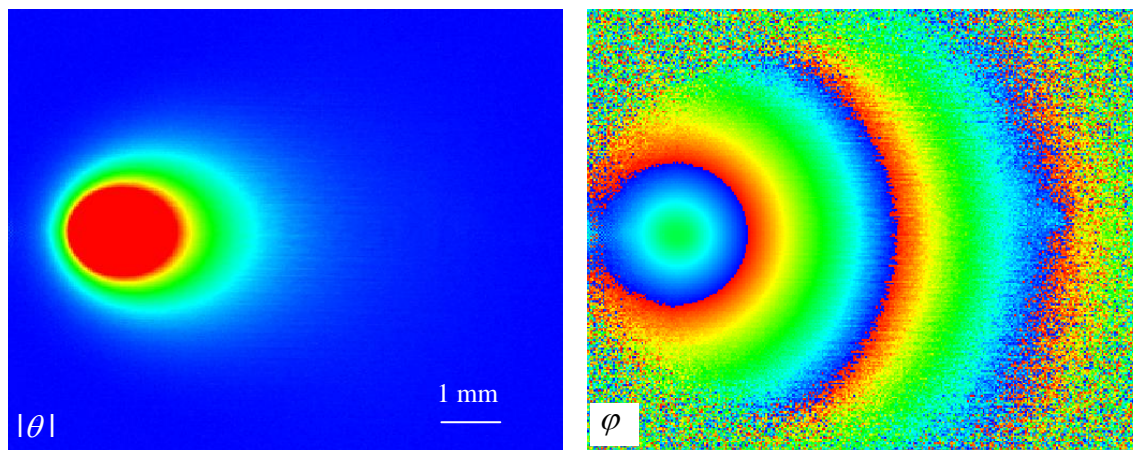
Figure 3.29: Experimental thermograms of the amplitude (left) and phase (right) of the surface temperature for a AISI sample moving to the right at *v* = 10 mm/s when it is illuminated by a laser spot of radius *a* = 0.2 mm modulated at *f* = 2.7 Hz which remains at rest.

The amplitude and phase profiles along the longitudinal and transverse directions will be analyzed for different samples, so the slope of the linear regions will be obtained in order to measure the thermal diffusivity.

3.3.6.   Thermal diffusivity measurements and discussion

Once the measurement procedure is explained, we will now show the diffusivity results and how they are obtained. In the laboratory, several samples covering a wide range of thermal diffusivities have been tested, from thermal insulators to good thermal conductors. Moreover, opaque, semitransparent, thick and thin samples have been analyzed. In the case of opaque samples, the illuminated surface is covered by a thin graphite layer to avoid heterogeneities in the surface emissivity. Also, this layer enhances the laser absorptivity and the infrared emissivity, improving the SNR.

Figure 3.30 shows the longitudinal phase profiles for an AISI-304 stainless steel sample with a thickness of 3 mm. Dots are the experimental data and the continuous lines the linear fits. To assess the robustness of the method we have performed several measurements varying the velocity and the frequency, but preserving the criterion previously established: $v^2/Df < 25$. For all the frequencies used in these cases, this

AISI-304 sample behaves as thermally thick. As can be observed, the linearity is very good and the retrieved thermal diffusivity values are the same within the experimental uncertainty ($D = 3.9 \pm 0.2$ mm^2/s) and in agreement with the reported value for this alloy (see Table 3.5).
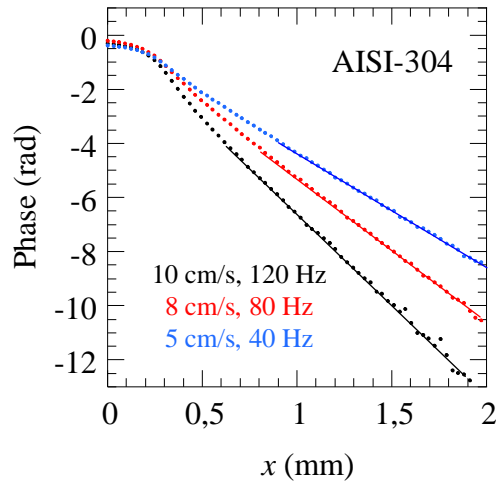

Figure 3.30: Experimental longitudinal phase profiles for AISI-304. Dots are the experimental data and the continuous lines the linear fits. Three couples (v, f) have been used to evaluate the robustness of the method.

In Figure 3.31 we plot the longitudinal phase profiles for seven samples covering a wide range of thermal diffusivities. Three of them are opaque and thermally thick samples (PEEK, AISI-304 and graphite), two are opaque and thermally thin (0.2 mm thick AISI-304 and 0.2 mm thick graphite) and two are semitransparent (orange Poly-Methyl-Methacrylate (PMMA) and amber PEEK).

As in the previous experiments, the couple speed and frequency is selected fulfilling the criterion $v^2/Df < 25$: opaque and thick PEEK (5 mm/s, 7 Hz), thick AISI-304 (80 mm/s, 80 Hz), thick graphite (100 mm/s, 18 Hz), orange PMMA (2.5 mm/s, 3 Hz), amber PEEK (3 mm/s, 4 Hz), thin AISI-304 (15 mm/s, 6 Hz) and thin graphite (100 mm/s, 13 Hz). It is interesting to note that the phase linearity extends for many radians (over more than 20 radians in the case of thermal insulators) due to the slow reduction of the temperature amplitude in the direction of the sample motion. The retrieved thermal diffusivity values are summarized in the third column of Table 3.5 and they agree very well with the literature values. In the case of graphite, we obtained different

values for the thick sample ($L = 9$ mm) and for the thin one ($L = 0.2$ mm). These results were confirmed by independent measurements performed by static laser spot lock-in thermography [27] and by laser flash technique [7].
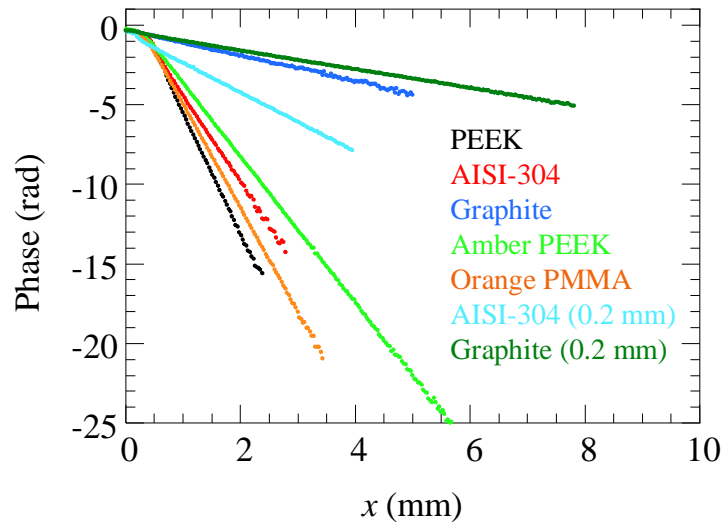

Figure 3.31: Experimental longitudinal phase profiles for the samples analyzed in this work.

We will finally show, in Figure 3.32, the transverse amplitude and phase profiles for AISI-304 and graphite. The transverse profiles for the other materials, the thermal insulators, are not plotted, as the curves are not usable for reliable thermal diffusivity measurements due to the lack of spatial resolution. Dots are the experimental data and the continuous straight lines are the linear fits. The thermal diffusivity values obtained using equation (3.46) are given in the second column of Table 3.5. They are consistent with the values obtained from the longitudinal profiles and agree with the literature values.
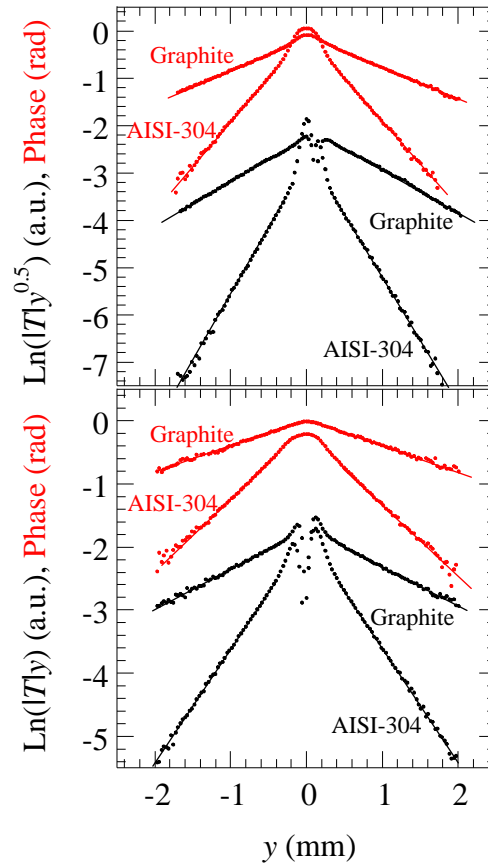
Figure 3.32: Experimental transverse amplitude and phase profiles for AISI-304 stainless steel and graphite. The upper figure corresponds to thermally thin samples (*L* = 0.2 mm) while the bottom figure is for thermally thick samples. Dots are the experimental data and the continuous lines are the linear fits.

It is important to mention that in the case of good thermal conductors, as metals or alloys, it is not difficult to obtain good results at speeds in the range 100 - 150 mm/s, which are realistic values for samples moving on a conveyor belt in in-line production. On the other hand, in the case of poor thermal conductors, the use of velocities above 10 mm/s requires frequencies higher than 20 Hz in order to fulfill the condition v^2/Df < 25. At those frequencies, due to the limited spatial resolution of our IR camera (30 μm/px), the amplitude and phase profiles may be too short and therefore the retrieved diffusivity lacks reliability.

Table 3.5: Retrieved thermal diffusivities using the linear methods. The first set corresponds to opaque and thermally thick samples, the second set to semitransparent samples and the third one to opaque and thermally thin samples.

Sample	D (mm^2/s) (Transverse)	D (mm^2/s) (Longitudinal)	D (mm^2/s) (Literature) [58-60]
PEEK	-	0.18 ± 0.01	0.2
AISI-304	4.0 ± 0.3	3.9 ± 0.2	4.0
Graphite	55 ± 3	60 ± 2	60[a,b]
Orange PMMA	-	0.105 ± 0.005	0.11
Amber PEEK	-	0.18 ± 0.01	0.2
AISI-304 ($L = 0.2$ mm)	3.8 ± 0.3	3.7 ± 0.2	4.0
Graphite ($L = 0.2$ mm)	76 ± 4	76 ± 2	74[a]

[a] Measured by a static lock-in thermography setup.
[b] Measured by the laser flash technique.

The concordance of the thermal diffusivity results with the literature values confirm the potential of laser spot lock-in thermography to be used in in-line inspection processes to measure the diffusivity without stopping the chain.

3.3.7.   Conclusions

For the first time it has been shown a decoupling of the surface temperature amplitude and phase behaviour in samples moving at constant speed while they are excited by a modulated laser beam.

We have proposed a method to measure the in-plane thermal diffusivity on isotropic samples based on simple linear relations found in the natural logarithm of the amplitude and in the phase along the longitudinal and transverse directions. The measurements were performed on samples covering a wide range of thermal diffusivities, from thermal insulators to good thermal conductors. The good agreement of the results with the reported diffusivity values confirms the validity of those linear methods.

One of the main advantages of this proposed method is that they are based on simple linear relations. They do not require complex multiparametric fittings, since the

linearity only depends on the velocity, the frequency and the diffusivity, and it is independent of other parameters like the laser radius or heat losses. Furthermore, this method does not need an absolute measurement of the surface temperature, which would be challenging as the surface emissivity should be known.

The use of a lock-in processing allows us to obtain very clean thermograms, with high SNR, so the thermal diffusivity values can be determined with high accuracy and precision.

4. Crack characterization

In the following sections we will see the contributions on crack characterization, both in calibrated samples and in real specimens. We will begin in Section 4.1 with a method based on infinite and vertical crack characterization to measure thermal conductivity of fluids. Section 4.2 presents the characterization of inclined infinite cracks. Finally, Section 4.3 will cover the measurements of the width and depth of cracks originated in real samples.

4.1. Infinite vertical crack evaluation. Calculation of fluids thermal conductivity

4.1.1. Introduction

The knowledge of the thermal conductivity of fluids is important from a point of view of basic research, and also it is essential in several technological applications where heat transfer is a common process, like, for instance, heat exchangers, thermal insulation and thermal refrigerant processes.

Different techniques have been proposed in order to measure the thermal conductivity in fluids, such as the parallel-plate, the steady-state cylindrical cell, the temperature

oscillation, the 3ω technique, the thermal comparator and the transient hot wire. In Paul et al. [68] a critical review of the methods mentioned above is given, and it is shown that the transient hot wire is the most accepted and extensively used technique at present. This is due to the high accuracy it provides and its capacity to eliminate the errors that arise from convective effects that are always present in the samples, caused by the existence of buoyancy forces. The transient hot wire [69] is a direct method of thermal conductivity measurement in which a very thin metal wire is immersed in the fluid sample and acts as both a heating unit and a temperature sensor. The thermal conductivity is evaluated directly from the slope of the linear region of the curve relating the temperature rise of the wire to the logarithm of time.

Nevertheless, this method has some limitations. One of them is the difficulty to select the linear interval of the mentioned curve that matches the conditions imposed by the theoretical model that describes the technique [70]. Moreover, a relatively high volume of the tested fluid is required, and also the electronic components that are used in the technique are complex. To all this, it is added the fact that the thin wire is very delicate, thus limiting the commercial progress of hot wire instrumentation [71].

Laser spot lock-in infrared thermography has proven to be an efficient non-contact method to measure thermal transport properties of solids, but its use for thermal characterization of gases and liquids is less extended.

However, an application of this laser-spot technique has been used to characterize vertical semi-infinite cracks, which allows the measurement of thermal contact resistance at the interface between two blocks [72]. This work has served as inspiration to propose a new method for thermal conductivity measurements in fluids that fill the interfacial cavity, as the thermal resistance is related to the interface width and the thermal conductivity of the material filling the gap. In this section, we describe the theoretical and experimental details behind this method, whose usefulness is confirmed by measurements of the thermal conductivity of air, water and ethylene-glycol, some of the most common fluids.

4.1.2.   Objectives

The main objectives of this study are:

- ▪ To design a non-contact method based in laser spot thermography to measure the thermal conductivity of fluids.

- ▪ To implement the method in an experimental configuration built in the laboratory.

- ▪ To assess the validity of the method using fluids with known conductivity values.

4.1.3.   Theoretical analysis

We consider a semi-infinite and opaque material, with thermal conductivity K and thermal diffusivity D, which is heated by a focused laser beam of power P_o and radius a. An infinite vertical crack of width w is located at the plane $y = 0$. The laser intensity is periodically modulated at an angular frequency $\omega = 2\pi f$, where f is the modulation frequency. The distance between the laser spot and the crack is l, and the thermal contact resistance of the crack is R_{th}. Figure 4.1 shows the geometry of the problem. We assume adiabatic boundary conditions at the surface, i.e. heat losses to the surrounding air are neglected.
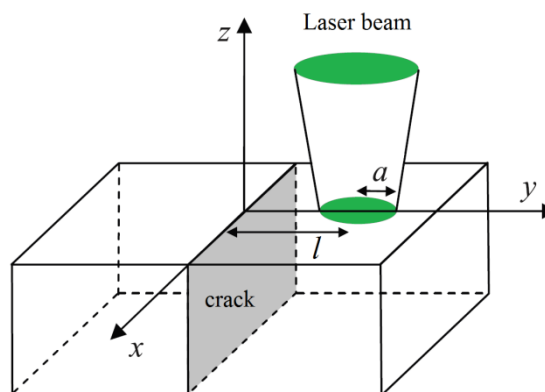

Figure 4.1: Scheme of the infinite vertical crack (grey) inside a semi-infinite sample.

We will consider the surface temperature profile along the *y*-axis, i.e. perpendicular to the crack and crossing the centre of the laser spot. The analytical expression of the amplitude surface temperature at *(0,y,0)*, calculated in [72], is

$$
T_{\pm}(0,y,0) = \frac{\eta P_o}{4\pi K} \int_0^{\infty} \delta J_o(|y-l|) \frac{e^{-\frac{(\delta a)^2}{8}}}{\beta} d\delta
$$

$$
\pm \frac{\eta P_o}{4\pi K} KR_{th} \int_0^{\infty} e^{-\frac{(\delta a)^2}{16}} I_o\left[\frac{(\delta a)^2}{16}\right] \frac{e^{\left(\frac{a^2\beta^2}{8}-\beta l-\beta|y|\right)}}{2+KR_{th}\beta} \tag{4.1}
$$

$$
\times \left[1 - erf\left(\frac{a^2\beta - 4l}{2\sqrt{2}a}\right) - e^{2\beta l} erfc\left(\frac{a^2\beta + 4l}{2\sqrt{2}a}\right)\right] \delta d\delta,
$$

where η is the power fraction absorbed by the sample, J_o is the zero order Bessel function, δ is the conjugated variable of radial coordinate in the Hankel space, $\beta = \sqrt{\delta^2 + \frac{i\omega}{D}}$, I_o is the modified Bessel function of order zero, *erf* is the error function and *erfc* is the complementary error function. The first term of the expression corresponds to the amplitude distribution when there is no crack, and the second term represents the contribution of the thermal waves scattered by the crack. The temperature of the material at $y > 0$ is given by T_+, and the temperature at $y < 0$ is given by T_-.

If the experimental temperature profile along the *y*-axis is fitted to the above analytical expression, the value of R_{th} can be retrieved. The thermal resistance is related to the width of the interface, *w*, and the thermal conductivity of the fluid that fills the interface, k_f, through the following relation [21]

$$
R_{th} = \frac{w}{k_f}. \tag{4.2}
$$

Accordingly, the width of a gap can be retrieved from the value of R_{th} obtained from a fit if we know which fluid fills the gap (its thermal conductivity, specifically), that can be air or any other gas or liquid. This relation has been used to determine the width of a crack filled with air, using air thermal conductivity [72].

However, in this section we are interested in the opposite situation, where we know the width of the interface and the thermal resistance associated to it, which is retrieved from the fitting of the experimental data to equation (4.1). Therefore, the unknown parameter is the fluid thermal conductivity.

We will make use of a "measurement cell", which is a configuration composed by two parallelepiped blocks with well known properties placed very close to each other, leaving a micrometric air gap of width w between them, which is filled with the sample fluid. The thermal conductivity k_f can be obtained using experimental measurements taken at different widths w, through a simple linear fit using the relation in equation (4.2).

4.1.4. Numerical calculations

In this subsection we analyze three different solids that may be candidates of composing the measurement cell. We will consider PEEK ($K = 0.25$ Wm^{-1}K^{-1} and $D = 0.2$ mm^2/s), AISI-304 ($K = 15$ Wm^{-1}K^{-1} and $D = 4$ mm^2/s) and aluminum ($K = 238$ Wm^{-1}K^{-1} and $D = 93$ mm^2/s) [22,58-60] so a wide range of thermal diffusivities (and conductivities) is covered. For all calculations, the following parameters are used: $a = 150$ μm, $l = 300$ μm and $f = 0.5$ Hz. Different power values P_o were chosen in each configuration to guarantee a maximum temperature amplitude of approximately 30 K as a good practical case.

Firstly, we begin analyzing the temperature profiles for a measurement cell made of AISI-304. Figure 4.2 shows computer calculations of the natural logarithm of the temperature amplitude profiles in the y-axis for a measurement cell composed of two pieces of AISI-304 stainless steel. We consider two different fluids, air and water, that fill the interfacial layer. Calculations were performed for four different widths of gap corresponding to realistic values of the measurement cell: 5, 10, 20 and 40 μm. As can be observed in Figure 4.2, an abrupt jump, ΔT, is observed in the temperature at the interface, which increases with the gap width.

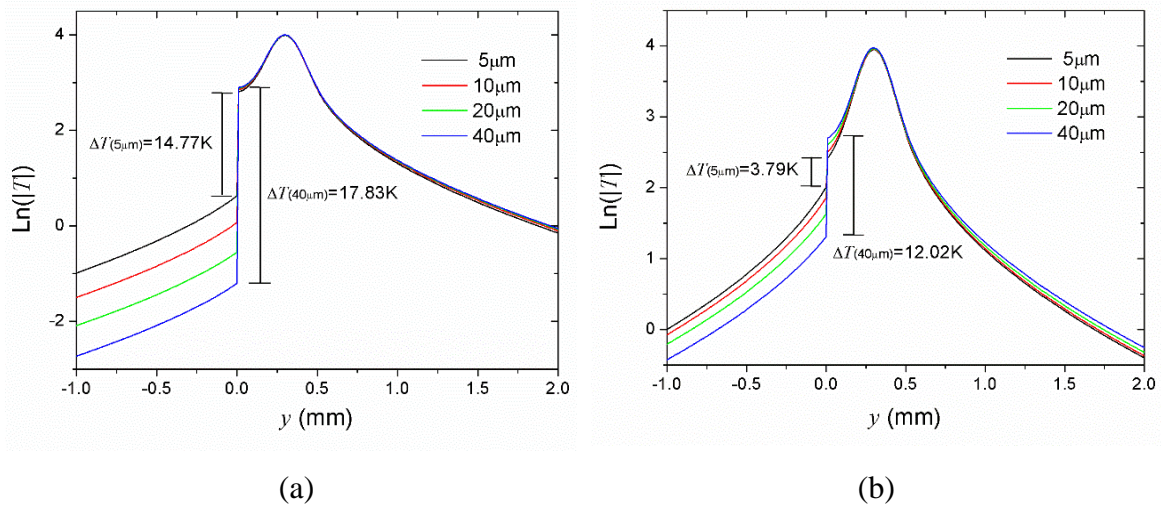(a)   (b)

Figure 4.2: Numerical calculations of the temperature amplitude curves, in a logarithmic scale, as a function of the distance *y*, for a system composed of two pieces of AISI304 stainless steel with (a) air ($k_{air} = 0.025$ Wm^{-1}K^{-1} [22]), and (b) water (k_w=0.6 Wm^{-1}K^{-1} [73]) as the fluid filling the gap layer, for different gap thicknesses. The experimental parameters are $a = 150$ μm, $l = 300$ μm, $f = 0.5$ Hz and $P_o = 0.3$ W.

It is important to notice that for the same interface width, the temperature jump at the discontinuity is higher for air than for water. This result is related to the fact that ΔT depends on R_{th}: the higher the thermal resistance, the higher the jump. According to equation (4.2), R_{th} is the ratio w/k_f, so for the same gap width, the higher the fluid conductivity the smaller the temperature jump at the interface. On the other hand, the difference in the temperature jumps between the 40 μm gap and the 5 μm gap is larger for water (8.23 K) than for air (3.06 K). Consequently, there are lots of possibilities to select a large range of gap thicknesses.

The use of the amplitude instead of the phase component of the temperature is due to the fact that the phase is less sensitive to width changes, as it can be seen in Figure 4.3, where the same parameters as in Figure 4.2a have been used. Note that the same vertical scale has been used in both amplitude and phase figures to clearly show that a much larger discontinuity is produced in amplitude than in phase and therefore the amplitude is more appropriate to size the width of the crack. Accordingly, in the remainder of Chapter 4 we will focus only on temperature amplitude data.
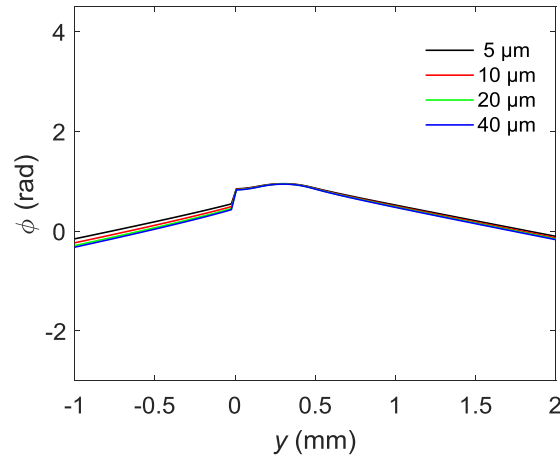
Figure 4.3: Numerical calculations of the phase curves (ϕ) as a function of the distance y, for a system composed of two pieces of AISI304 stainless steel with air as the fluid filling the gap layer, for different gap thicknesses. The experimental parameters are $a = 150$ μm, $l = 300$ μm, $f = 0.5$ Hz and $P_o = 0.3$ W.

In order to select the best solid material to build the measurement cell, we perform a sensitivity analysis of the dependence of the temperature jump ΔT on k_f. In Figure 4.4 we show the calculations of ΔT as a function of k_f for the three solids that we are interested in: AISI-304, PEEK and Al, and the same gap widths as in Figure 4.2 (between 5 and 40 μm). The parameters a, l and f are the same than before. The laser power P_o is set to 6.8 mW for PEEK, 0.3 W for AISI-304, and 4.7 W for Al.

We can see that the curves for different widths decrease with increasing k_f. Moreover, for a very low fluid thermal conductivity, the ΔT is nearby its maximum value, but is practically the same for any gap width. On the contrary, for very high fluid conductivity, the ΔT tends to 0 for any width. The region we are interested in is where the ΔT has a significant change as the k_f varies. It is interesting to note that the curves shift in the direction of increasing k_f when the width of the gap rises.

As can be seen, the region of highest sensitivity (largest change of ΔT when varying k_f) is different for each solid. In particular, the k_f value with the highest sensitivity increases with the thermal conductivity of the solid: for PEEK, a poor thermal conductor, the highest sensitivity is at around $k_f = 10^{-2}$ Wm^{-1}K^{-1}; for AISI-304, an

intermediate conductor, the highest sensitivity is at around $k_f = 10^{-1}$ Wm^{-1}K^{-1} and for Al, a good thermal conductor, the highest sensitivity is at around $k_f = 2$ Wm^{-1}K^{-1}.
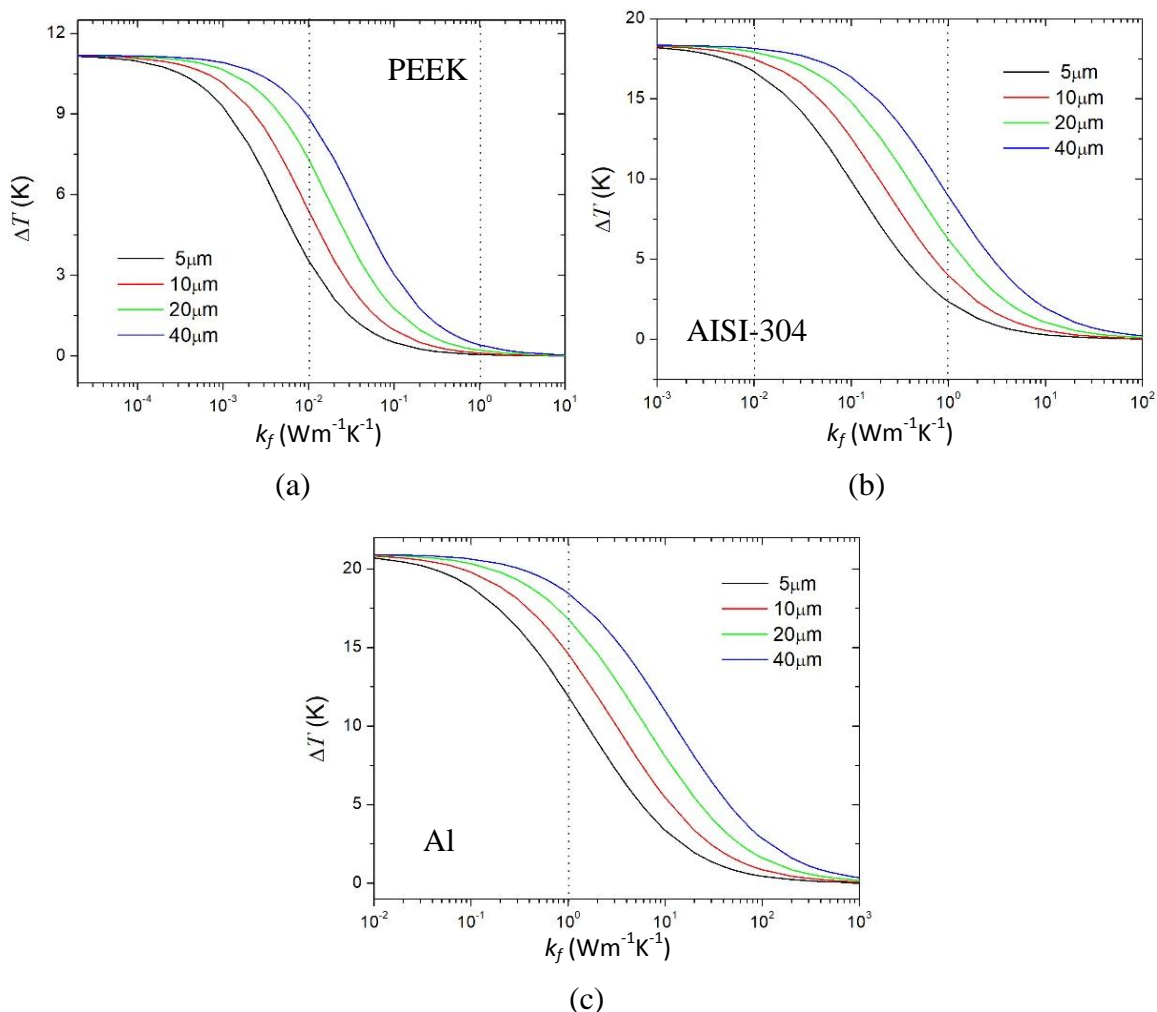

(a)

(b)

(c)

Figure 4.4: Numeric calculations of ΔT as a function of fluid conductivity k_f for different gap widths in a system composed of (a) PEEK, (b) AISI-304 and (c) Al. Dotted lines represent the limits of k_f values of interest in this work, from 1×10^{-2} to 1 Wm^{-1}K^{-1}, which includes liquids and gases. The experimental parameters are $a = 150$ μm, $l = 300$ μm, $f = 0.5$ Hz and $P_o = 0.3$ W.

However, in the case of Al it is important to note that the power required to obtain amplitude values at the surface like those of PEEK and AISI 304 is very high (several W), and therefore this option is not suitable for practical cases. As all fluids and gases are in the thermal conductivity range from 10^{-2} to 1 Wm^{-1}K^{-1}, AISI-304 is the best

choice for building the measurement cell, using the parameters a = 150 μm, f = 0.5 Hz and l = 300 μm, which are considered the typical values used in the experiments.

4.1.5.   Experimental procedure

The experimental set-up is depicted in Figure 4.5. The laser is modulated using the optical chopper, and falls on the surface of one of the two blocks perpendicularly. The windowing of the IR camera is set to full frame, and the FR is set to 383 Hz (the maximum value at maximum windowing). The camera records approximately 15,000 images and they are processed in the lock-in module so, according to equation 2.12, the average noise in the amplitude of the temperature is reduced down to ∼ 0.3 mK.
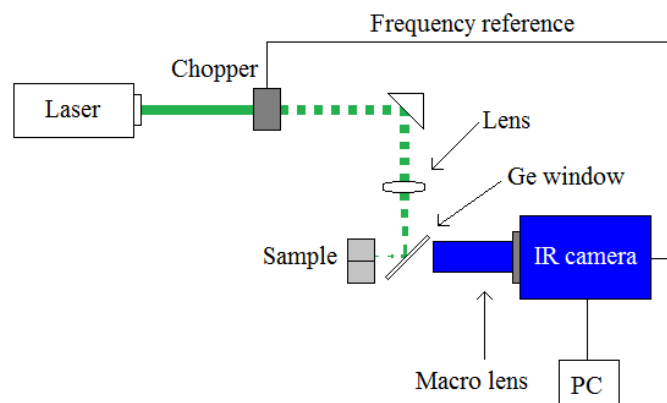

Figure 4.5: Scheme of the experimental set-up

The chosen test fluids are air, a low thermal conductivity gas (k_a = 0.026 Wm^{-1}K^{-1}) [22]; water, considered a high thermal conductivity liquid (k_w = 0.6 Wm^{-1}K^{-1}) [73]; and ethylene glycol (k_e = 0.258 Wm^{-1}K^{-1}) [74], an intermediate conductivity liquid.

In accordance with the sensitivity study of the previous subsection, the measurement cell is made of two AISI-304 stainless steel cubes of 3 cm side, whose contact surfaces are polished. By placing them very close to each other a micrometric air gap is left between them, which has a constant width (within the possible uncertainty due to irregularities on the blocks edges). A simple way to achieve different widths of the interficial layer using a single cell is to incline one of the blocks so the gap width changes progressively. Figure 4.6 shows the diagram of this measurement cell

configuration, showing the wedged gap between two blocks of stainless steel, which is obtained by sandwiching two metallic sheets of different thicknesses (denoted as w_A and w_B), between the blocks, close to the ends. In this way, the nominal values of the gap width along the *x*-axis are known.
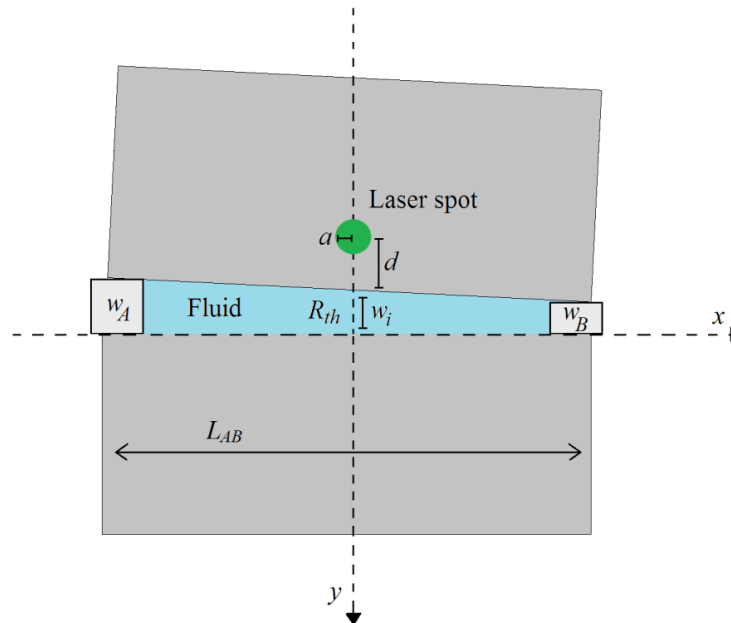

Figure 4.6: Schematic representation of the measurement cell showing the separation sheets used to construct the wedged gap between the two AISI-304 stainless steel blocks. The horizontal and vertical axes are not scaled.

A moderate pressure is applied to the blocks to maintain the different parts together. The laser and the camera positions are fixed, while the sample can be displaced using a micrometer stage along the *x*-axis with a 2 mm step. Due to the wedged shape of the cavity, for each position of the sample the interface width at the location of the laser spot is different. Even if the theoretical model describes a perpendicular interface, the effect of the wedge angle is negligible as it is smaller than 0.1° in all data sets. Moreover, the temperature data used for quantification of the thermal resistance is restricted to the profile that crosses the center of the laser spot, so only a vertical array of 1 pixel width is taken.

The sample surface is kept perpendicular to the optical axis of the camera. The temperature amplitudes along the transverse y-profile crossing the gap through the center of the laser spot are recorded for different widths w_i of the gap. These gap widths

were determined by measuring the thicknesses w_A and w_B, the distance between the metallic sheets (L_{AB}) and the position i of the laser spot on the *x-axis* ($i = 0$ when we are located at w_A, and $i = L_{AB}$ when we are located at w_B). The width at each position, therefore, is

$$w_i = w_A - i \cdot \frac{w_A - w_B}{L_{AB}}. \tag{4.3}$$

The used values of laser power, radius and distance to the interface are $P_o = 300$ mW, $a = 180$ μm and $d = 390$ μm, respectively. A very thin graphite layer, about 5 μm thick, was sprayed on the surface of the blocks to enhance and homogenize the infrared emissivity over the entire surface, besides of increasing the absorption of the excitation beam.

4.1.6.   Experimental results and discussion

In Figure 4.7 we show the results when the filling fluid is air. Measurements have been performed at $f = 0.3$ Hz. The top figures show the amplitude thermograms when the laser excites the surface at a position where the water nominal thickness is $w = 10.4$ μm (Figure 4.7a) and $w = 5.6$ μm (Figure 4.7b). The two thermograms have a distinct shape. In the thermogram belonging to a larger width gap a high asymmetry can be observed between the top and the bottom parts, showing a big temperature jump caused by a large gap. On the other hand, in the thermogram belonging to the lowest width gap, the asymmetry is least noticeable (although it is still present) as the thermal barrier is smaller. The white arrows mark the pixel array taken as the temperature profile.

In Figure 4.7c we plot the natural logarithm of the temperature amplitude profiles along the *y-axis* for four different nominal widths ($w = 10.4, 8.5, 7.5$ and 5.6 μm). Note that the curves are shifted along the vertical axis to better appreciate the jumps at the interface, which is placed at $y = 0$. Dots are the experimental data and the continuous lines are the multiparametric fitting curves to equation (4.1) using a least-square fitting based on a Levenberg-Maquard algorithm with four free parameters, that can be grouped like this: $\eta P_o/K$, l, a, and KR_{th}. The retrieved R_{th} values are inserted in the figure (left branch of the curves), together with the confidence intervals of the nonlinear

regression, in units of 10^{-4} Km^{2}W^{-1}. The corresponding nominal widths are also inserted for clarity (right branch of the curves).

The values of parameters l, a, and $\eta P_o/K$ are of less interest, as they are set by the user. However, their fitting allows us to verify the quality and consistency of the fits as they are in excellent agreement with the preset experimental conditions. The rough values of these parameters previously determined experimentally are introduced as initial values in the multiparametric fitting to avoid possible inadequate convergence. Note that, despite using a model that neglects heat losses by convection and radiation, the quality of the fittings is very high, which indicates that the approximation is valid.
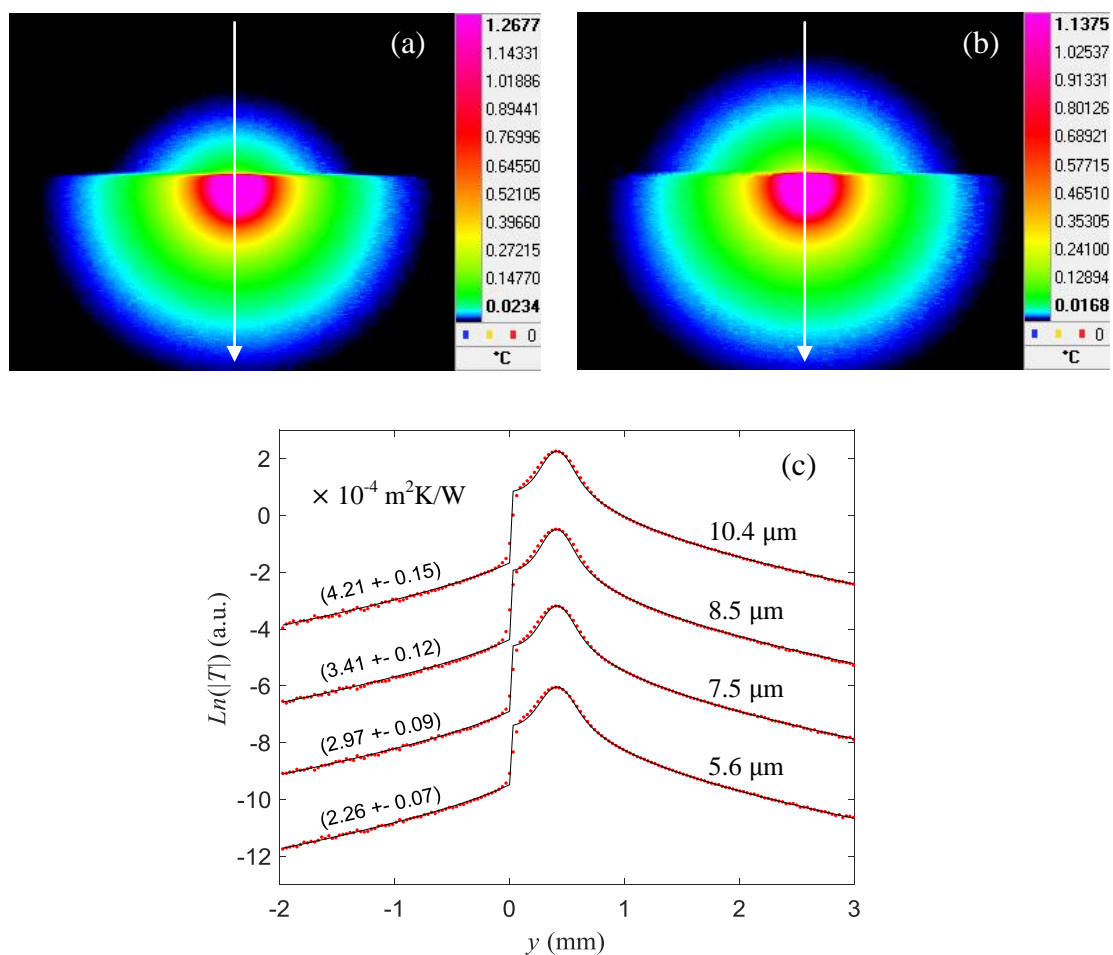

Figure 4.7: Top figures: Amplitude thermograms for an air sample for widths $w = 10.4$ µm (a) and $w = 5.6$ µm (b) at a modulation frequency of $f = 0.3$ Hz. Bottom figure: (c) Natural logarithm of the temperature amplitude profiles along the y-axis for four nominal widths ($w = 10.4$, 8.5, 7.5 and 5.6 µm), using the same modulation frequency. The inserted values are the thermal resistances in units of 10^{-4} Km^{2}W^{-1}.

Figure 4.8 shows the results for water. Measurements have also been performed at $f =$ 0.3 Hz. The top figures show the amplitude thermogram obtained at $w = 70$ μm (a) and $w = 26$ μm (b). Figure 4.8c shows the natural logarithm of the temperature amplitude profiles along the y-axis for four widths ($w = 70, 56, 41$ and 26 mm). Dots are the experimental data and the continuous lines are the fittings to equation (4.1). The retrieved R_{th} values are inserted in the figure, as are the nominal widths.
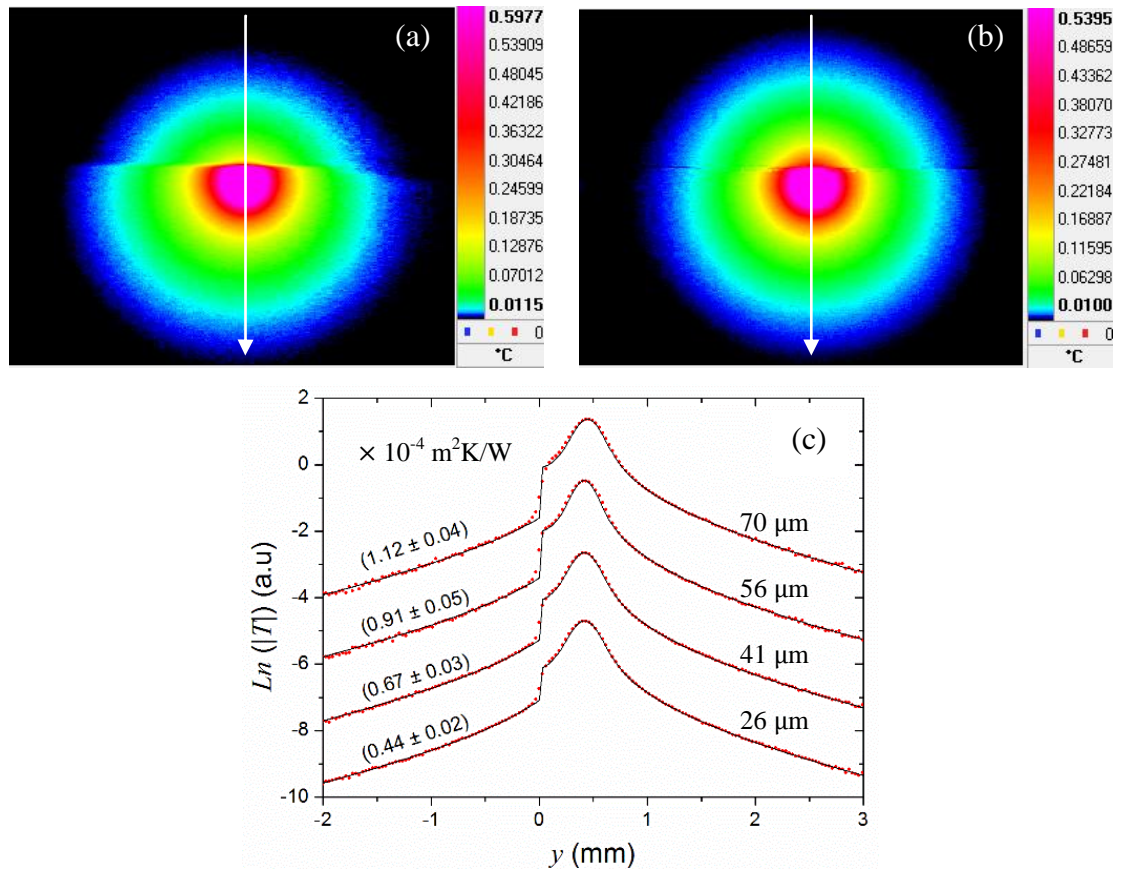

Figure 4.8: Top figures: Amplitude thermograms for a water sample for widths $w = 70$ μm (a) and $w = 26$ μm (b) at a modulation frequency of $f = 0.3$ Hz. Bottom figure: (c) Natural logarithm of the temperature amplitude profiles along the y-axis for four nominal widths ($w = 70, 56, 41$ and 26 μm), using the same modulation frequency. The inserted values are the thermal resistances in units of 10^{-4} Km^{2}W^{-1}.

In Figure 4.9 we can see the results for ethylene glycol, using the same frequency ($f = 0.3$ Hz). The top figures show the amplitude thermogram obtained at $w = 43$ μm (a) and $w = 24$ μm (b). Figure 4.8c shows the natural logarithm of the temperature amplitude profiles along the y-axis for four widths ($w = 43, 35, 31$ and 24 mm), where dots are the

experimental data and the continuous lines are the fittings to equation (4.1). The retrieved R_{th} values are inserted in the figure, as are the nominal widths.
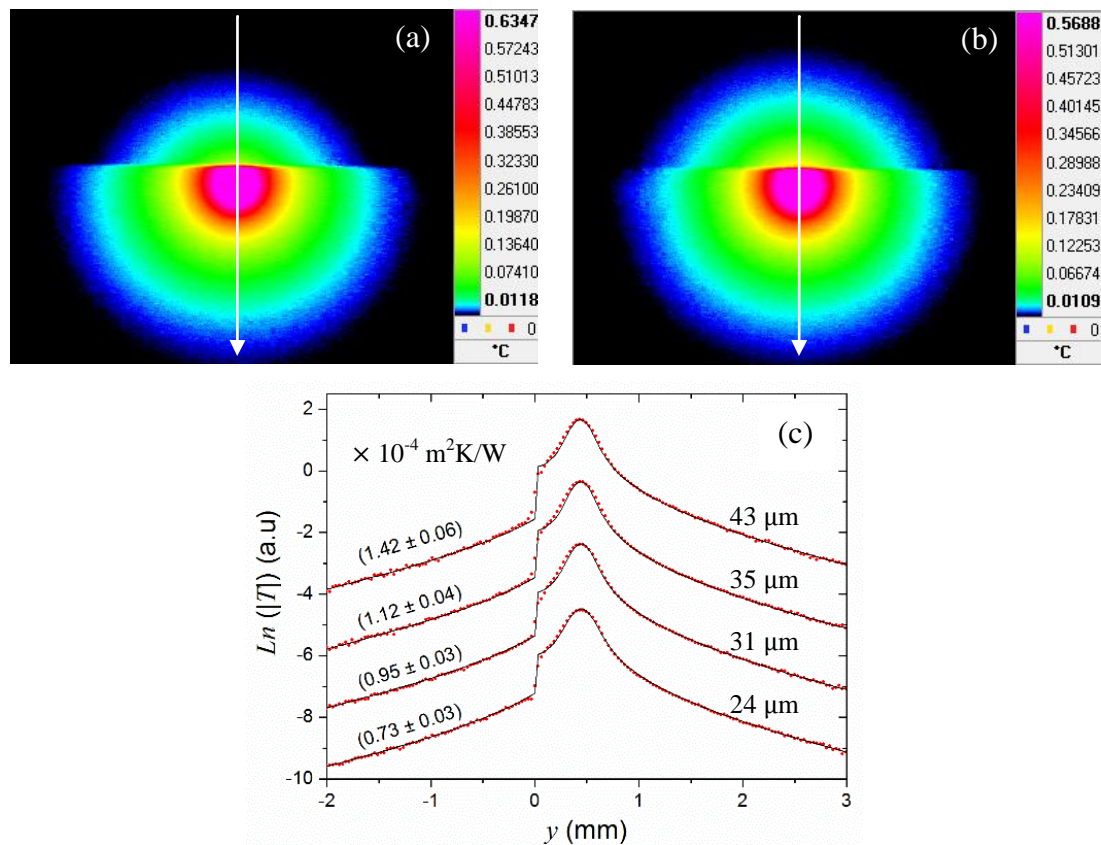

Figure 4.9: Top figures: Amplitude thermograms for an ethylene glycol sample for widths $w = 43$ μm (a) and $w = 24$ μm (b) at a modulation frequency of $f = 0.3$ Hz. Bottom figure: (c) Natural logarithm of the temperature amplitude profiles along the *y*-axis for four nominal widths ($w = 43, 35, 31$ and 24 μm), using the same modulation frequency. The inserted values are the thermal resistances in units of 10^{-4} Km^2W^{-1}.

In Figures 4.10 to 4.12 the nominal w values are plotted as a function of the retrieved thermal resistance R_{th} for the experiments performed with air, water and ethylene-glycol. The horizontal and vertical error bars correspond to the uncertainties in R_{th} and w, respectively.

The uncertainty in the thermal resistance is the one corresponding to the fitting procedure of the temperature profiles to equation (4.1). The uncertainty in the nominal width is obtained analyzing equation 4.3, and it arises from the second term, because

the absolute value of w is not relevant as what matters is the change of w with i, so $\left|\frac{dw_i}{di}\right| = \frac{w_A - w_B}{L_{AB}}$. Therefore, $\Delta w_i = \frac{w_A - w_B}{L_{AB}} \cdot \Delta i$. The value of $\frac{w_A - w_B}{L_{AB}}$ is around 1.5×10^{-3} in the worst scenario, and the possible error of measuring i is around 2-3 pixels ($\sim$75 µm). Consequently, the resulting uncertainty in the estimation of the interface widths w_i is around 0.1 µm.

The solid curves are the best linear fits of the data and the slope values give the thermal conductivity of the fluid: $k_a = 0.026 \pm 0.002$ Wm^{-1}K^{-1}, $k_w = 0.61 \pm 0.02$ Wm^{-1}K^{-1}and $k_e = 0.27 \pm 0.02$ Wm^{-1}K^{-1}. They are in good agreement with the literature values [22,73,74]. As we can see, the measurement uncertainty in the fittings obtained with this configuration is very low, with values between 3.5% and 7%, demonstrating the accuracy of the method.

Figure 4.10: Interface width as a function of the retrieved thermal resistance for air (red dots with error bars). The solid line is the result of the best linear least squares fit performed considering the uncertainties in both the interface thermal resistance and width.
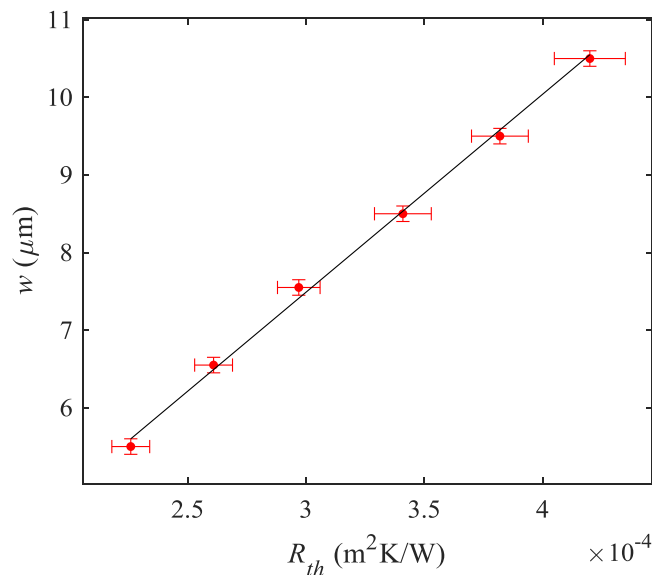
Figure 4.11: Interface width as a function of the retrieved thermal resistance for water (red dots with error bars). The solid line is the result of the best linear least squares fit performed considering the uncertainties in both the interface thermal resistance and width.

Figure 4.12: Interface width as a function of the retrieved thermal resistance for ethylene glycol (red dots with error bars). The solid line is the result of the best linear least squares fit performed considering the uncertainties in both the interface thermal resistance and width.
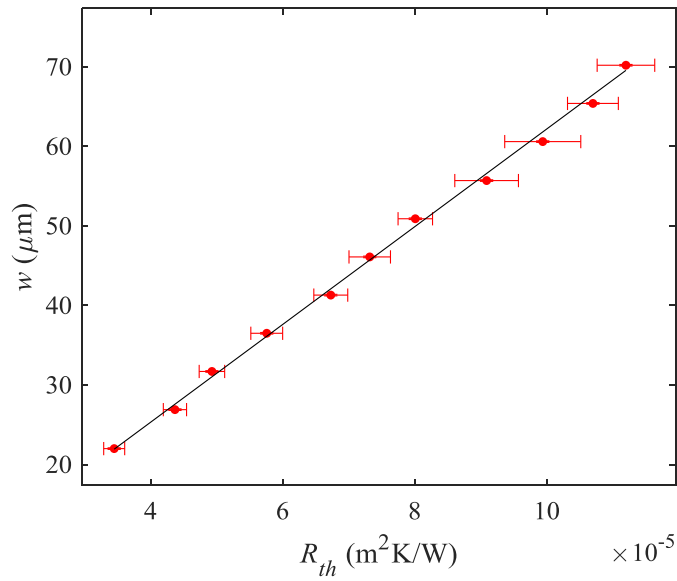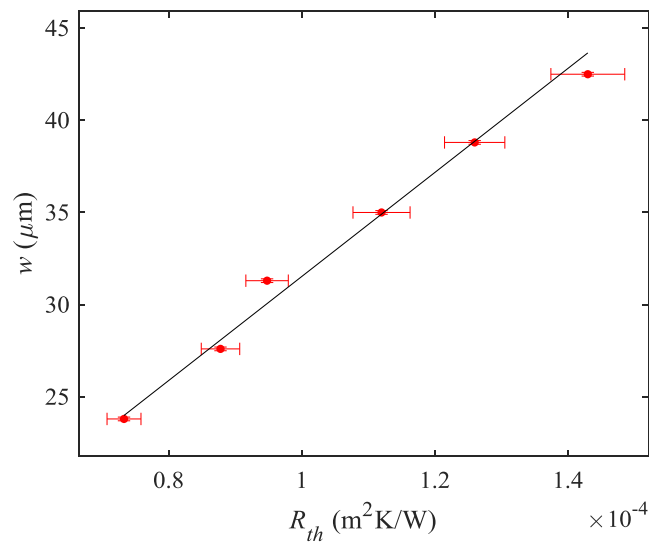
4.1.7.   Conclusions

We have presented a new method that allows thermal conductivity measurements in gases and liquids. It uses lock-in infrared thermography with laser spot heating for very straightforward measurement of the thermal conductivity of gases and liquids that fill the gap layer between two blocks, when this separation is known and variable. This is an accurate method, as the measurement uncertainty lies at around 5%.

One of the advantages of the method is that each set of measurements (the series of measurements from small to large w) takes only some minutes to be performed, so it is a relatively fast technique. Another advantage is that it is a non-contact method: both thermal excitation and detection involve radiation, with no damage on the samples. Moreover, it requires very small quantity of sample (about 1-2 mm^3). Consequently, it offers significant benefits if we compare it to conventional techniques for thermal characterization of fluids, such as the hot wire method.

4.2. Characterization of infinite inclined surface-breaking cracks

4.2.1. Introduction

In this section the characterization of the width and angle of tilted infinite surface-breaking cracks will be addressed. As it has been shown in the previous section, when a laser beam is focused at the sample surface the excitation induces a lateral heat flux, which is disturbed by the presence of a surface breaking crack. As a result, an abrupt temperature discontinuity appears in the thermogram along the length of the fissure.

In the case of infinite vertical cracks, as it has been indicated in Section 4.1, an analytical expression of the surface temperature profile can be obtained, and fitting the theoretical expression of the surface temperature to the experimental data the width of the crack can be retrieved.

However, when a crack has a different geometry rather than being a surface-breaking, infinite in depth and vertical crack, there is not an analytic solution to the problem, and the surface temperature must be obtained numerically. In a most general case, it is possible that the crack does not lie perpendicular to the surface, but inclined with an angle. This is the case of defects in rolling or forging laps [75-78]. Rolling contact fatigue cracks develop from the surface and usually propagate at their early stage making a small angle with the surface [79,80].

In this study we address the challenge of sizing the width and angle of tilted infinite cracks using laser-spot lock-in thermography, with the aim of covering different crack orientations and generalize the characterization of fatigue cracks beyond vertical fissures. We make use of Finite Element Methods (FEM) to solve the heat diffusion equation to simulate the surface temperature of a sample containing an infinite tilted crack, with the purpose of fitting the numerical temperature to experimental data obtained from calibrated tilted cracks.

4.2.2.   Objectives

The main objectives of this study are:

- To simulate the temperature of a sample containing a tilted planar infinite fissure making an arbitrary angle with the surface when a modulated laser beam hits the sample surface close to the crack.

- To perform a sensitivity analysis to verify if the crack width and angle are uncorrelated so they can be obtained simultaneously from the same amplitude thermogram.

- To verify the validity of the method by performing laser-spot lock-in thermography experiments on samples containing artificial calibrated inclined infinite cracks.

4.2.3.   Theoretical analysis

In this section we describe the method to calculate the temperature of a sample that contains an infinite in depth inclined crack, which is illuminated by a harmonically modulated laser spot. In Figure 4.13 the configuration is depicted, where l is the distance between the center of the laser spot and the crack, w is the width of the crack and θ is the angle of the crack with respect to the illuminated part of the surface.
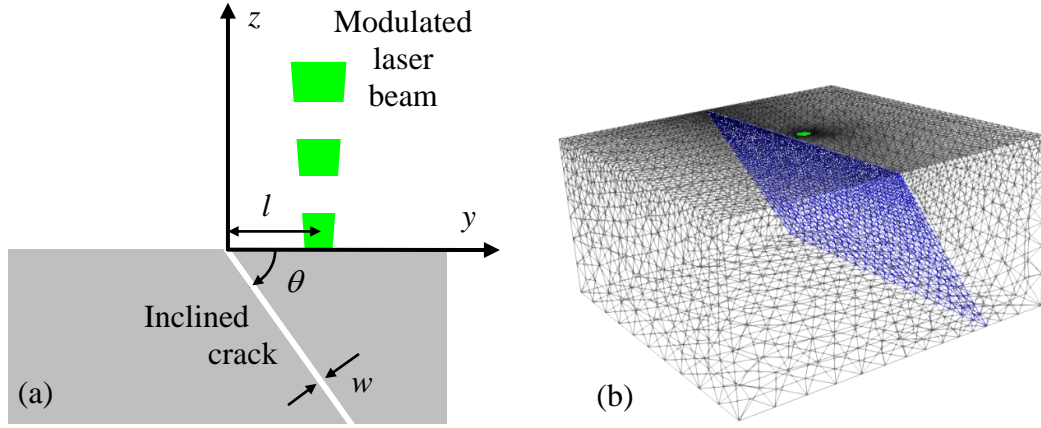
Figure 4.13: (a) Cross section of the sample containing an infinite inclined crack. (b) Triangulation of the sample domain. The crack is depicted in blue as a 2-D interface, whereas the laser heat supply is depicted as a green circle. Only the surface mesh is represented for the sake of clarity.

We consider a laser beam with a Gaussian profile that it is focused to a radius a at $1/e^2$ of the maximum intensity and its center is located on the y-axis $(0,l,0)$. The laser power is P_o and its amplitude is modulated at a frequency f ($\omega = 2\pi f$), so $P = P_o(1+\cos(\omega t))/2$.

In general, the sample temperature is the superposition of the room temperature, a stationary temperature rise and an oscillating temperature at the same frequency f as the illumination. In lock-in thermography we are interested only in the temperature oscillation (from now on T) which satisfies the heat diffusion equation

$$\nabla^2 T(\vec{r}, t) - \frac{1}{D} \frac{\partial T(\vec{r}, t)}{\partial t} = 0 \tag{4.4}$$

The temperature T also satisfies the heat flux continuity condition at the sample surface (equation 4.5) and at the crack surface (equation 4.6)

$$-K \left.\frac{\partial T(\vec{r}, t)}{\partial z}\right|_{z=0} = \frac{\eta P_o}{2\pi a^2} e^{-\frac{2r^2}{a^2}} \cos(\omega t), \tag{4.5}$$

$$[\![K \nabla T(\vec{r}, t)]\!]|_{crack} = 0 \tag{4.6}$$

where η is the power fraction absorbed by the sample, and K is the thermal conductivity of the material. The [[ ]] operator stands for the change on the flux over the crack. Moreover, T satisfies the equation regarding the temperature discontinuity at the crack position

$$\Delta T(\vec{r},t)|_{crack} = R_{th}K\,\nabla T(\vec{r},t). \qquad (4.7)$$

Furthermore, as it was shown in the previous section (equation 4.2), the thermal resistance R_{th} is directly related to the crack width and the air thermal conductivity ($R_{th} = w / k_{air}$).

In the equations above, heat losses by convection and radiation have been neglected. This assumption is valid if the amplitude of the temperature oscillation of the sample is small. In this way, adiabatic boundary conditions are taken for the remaining sample surfaces.

For the set of equations (4.4) to (4.7), T has an analytical solution only for an infinite vertical crack (the angle $\theta = 90°$), as it has been shown in Section 4.1. In the case of an inclined crack, there is no analytical solution, so we have to proceed numerically using Finite Element Methods (FEM). FEM provide a solution to the model equations over a spatial triangulation of the studied domain. This configuration is usually modeled as a transmission problem in a material consisting of two domains, the bulk material and the air filling the crack, and it requires the meshing of the full domain, including the crack, which implies very fine spatial discretization inside the crack volume. Therefore, for very thin cracks, this model requires extremely fine meshes, which leads to a dramatic increase of memory resources and computing time.

A clever way to overcome this drawback is to model the crack as a two dimensional thin boundary layer with fixed thermal resistance. Therefore, the FEM are carried out considering the crack as a surface characterized by a thermal resistance. This modelling strategy avoids the need of using extremely fine meshes in the crack region usually required when the problem is addressed as a transmission problem through the air that fills the crack, and the crack is narrow.

As can be seen in Figure 4.12b, the centered and densely discretized area corresponds to the iluminated zone around the center of the laser spot, where the boundary condition

equation (4.5) is applied in a circle of a radius $2a$ in the numerical discretization. The election of this distance guarantees that outside this circle the intensity of the gaussian excitation is negligible.

The amplitude depends on different parameters, which we can group in three categories: the thermal properties of the sample (D and K), the laser characteristics (η, P_o, a and f) and the crack parameters (l, θ and R_{th}).

According to equation (4.5), the dependence of T on the ratio $\eta P_o/K$ indicates that for a given laser power the amplitude of the temperature oscillation is high for poor thermal conductors, and vice versa. Moreover, according to Eq. (4.7) the temperature discontinuity at the crack depends on the product $KR_{th} = Kw/k_{air}$, indicating that for a given crack width the temperature jump at the crack is large for good thermal conductors or equivalently, it is much easier to detect narrow cracks in good thermal conductors than in thermal insulators.

We have already seen these mentioned effects in Section 4.1 for the vertical crack case. In the next subsection, we will analyze numerically the effect of changing the angle and the width of the crack. We will make use of a code developed in our research group that uses FEM to solve the set of equations (4.4) to (4.7).

4.2.4.   Numerical simulations

The solution of equations (4.4) to (4.7) gives the temperature oscillation T, which depends on the time harmonically. However, we are interested in the amplitude of this oscillation, $|T|$, which is the quantity recorded in experiments that is obtained after a lock-in processing. Moreover, according to the numerical calculations performed in 4.1.4, the phase component will not be used.

First of all, we ensure that the amplitude obtained from the FEM using $\theta = 90º$ is the same as the one obtained from the analytical equation (4.1), using the infinite vertical crack configuration in Section 4.1.

The amplitude profiles along the *y*-axis for both models are compared using the same parameters ($a = 0.2$ mm, $l = 0.4$ mm, $P_o = 0.1$ W, $\eta = 1$, $f = 0.8$ Hz and $w = 5$ μm). In Figure 4.14 the profiles are plotted at the top, while the residuals, $\ln(|T_{analytical}|)$ - $\ln(|T_{FEM}|)$, are depicted at the bottom.
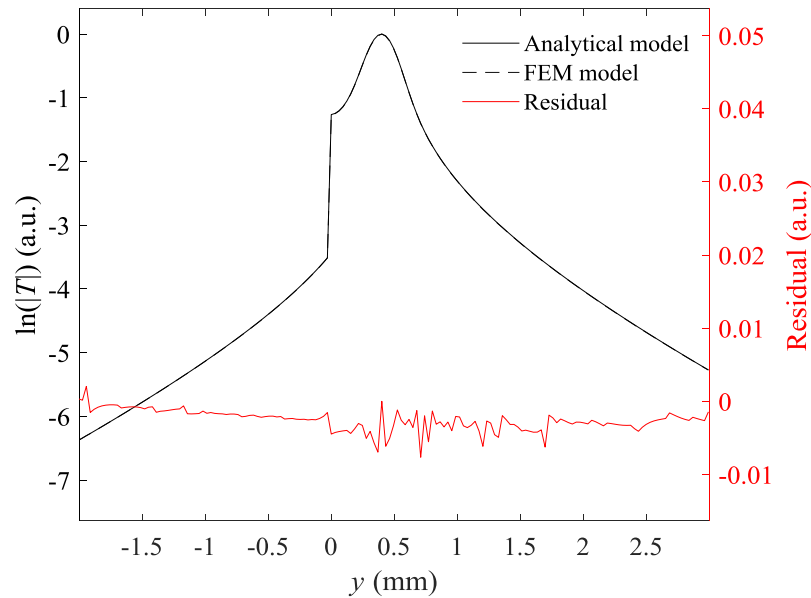

Figure 4.14: Analytical model (continuous black line) and FEM profile (dashed black line) of the temperature amplitude using $a = 0.2$ mm, $l = 0.4$ mm, $P_o = 0.1$ W, $\eta = 1$, $f = 0.8$ Hz and $w = 5$ μm. The residuals between the two profiles, $\ln(|T_{analytical}|)$ - $\ln(|T_{FEM}|)$, are plotted at the bottom in red.

It can be seen that both curves are indistinguishable, and the residuals between the two profiles are lower than 6×10^{-3}. As this validation is done, it is assumed that the FEM model works properly for any other inclination.

In Figure 4.15a we plot the simulations of the amplitude of the temperature profile along the *y*-axis, which is a profile perpendicular to the crack and that crosses the center of the laser spot, for a sample made of stainless steel AISI-304 ($D = 4$ mm^2/s, $K = 15$ Wm^{-1}K^{-1}). The sample is illuminated by a Gaussian laser beam of radius $a = 0.2$ mm, whose center is located at a distance $l = 0.4$ mm from the crack. The laser power is $P_o = 0.1$ W (with $\eta = 1$) and the modulation frequency is $f = 0.8$ Hz. The values of all of these parameters lie within the typical values used in the laboratory. In all cases, the crack width is the same, $w = 5$ μm, and seven different crack angles are analyzed.

As we are used to, the natural logarithm of the amplitude is plotted, rather than the amplitude itself, to better resolve the curves far away from the excitation, where the temperature features low values, like the ones at the non-illuminated side of the crack.

It can be observed that varying the crack angle produces a small change on the temperature profile. In particular, for $\theta < 90°$ the effect is concentrated at the illuminated side of the sample ($y > 0$), while the non-illuminated branch of the profile ($y < 0$) remains insensitive. On the contrary, for $\theta > 90°$ the effect is more pronounced at the non-illuminated side of the sample ($y < 0$), while the illuminated branch of the profile ($y > 0$) remains almost unchanged.
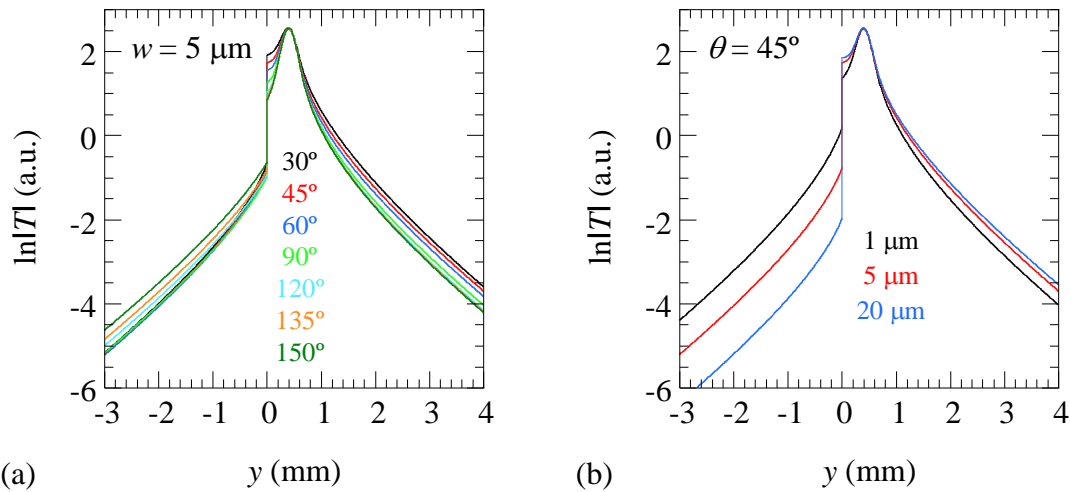

Figure 4.15: Simulated profiles of $\ln|T|$ as a function of the transverse distance to a crack, located at $y = 0$. (a) Same crack width, $w = 5$ μm, and different inclinations (from 30° to 150°). (b) Same angle with the surface, $\theta = 45°$, and three different widths. Simulations have been performed for AISI-304 with the following experimental parameters: $\eta = 1$, $P_o = 0.1$ W, $f = 0.8$ Hz, $a = 0.2$ mm and $l = 0.4$ mm.

In Figure 4.15b we show the effect of varying the crack width while the angle is kept constant ($\theta = 45°$). The calculations have been performed using the same thermal and geometrical parameters as in Figure 4.15a. As can be observed, changing the crack width considerably affects the temperature discontinuity at the crack position. The differences between Figures 4.15a and 4.15b indicate that $\ln|T|$ is more sensitive to w

than to θ. Consequently, it is expected that using a laser-spot lock-in thermography setup w will be obtained with a higher precision than θ.

However, as we are interested in measuring both the width and inclination of the crack at the same time, we have to verify that they are not correlated: only a single (w, θ) couple can reproduce a given temperature profile, so w and θ can be determined univocally from the same amplitude thermogram.

In order to address this issue, we have calculated the sensitivity of $\ln|T|$ to w and θ:

$$S_j = j\,\frac{\partial\ln(|T|)}{\partial j}\ , \ \ j = w,\theta \tag{4.8}$$

In Figure 4.16 we plot the simulation of the sensitivity of $\ln|T|$ along the y-axis profile to both parameters in the case of a typical crack: $w = 5$ μm and $\theta = 45°$. The sensitivity to the width (S_w) is shown in black and the sensitivity to the angle (S_θ) in red. These simulations have been performed for AISI-304 with the same experimental parameters as in Figure 4.13: $\eta = 1$, $P_o = 0.1$ W, $f = 0.8$ Hz, $a = 0.2$ mm and $l = 0.4$ mm.
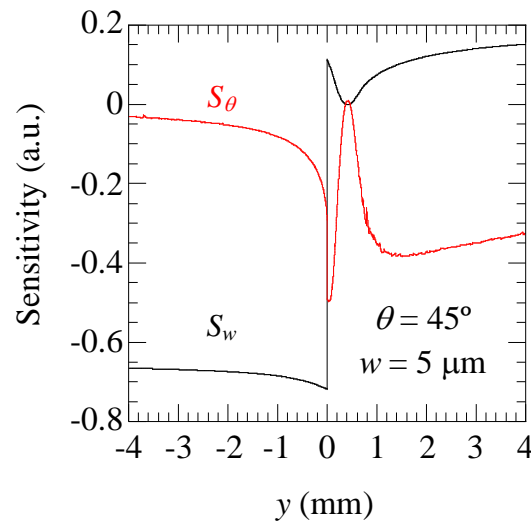

Figure 4.16: Simulation of the sensitivity of $\ln(|T|)$ to the width, S_w, and to the angle, S_θ, for a 5 μm wide crack making an angle $\theta = 45°$ with the surface. Simulations have been performed for an AISI-304 sample with the same experimental parameters as in Figure 4.15, only varying the crack parameters w and θ.

As can be observed, both *w* and θ are not correlated since their sensitivities are not proportional, and, therefore, they can be obtained univocally from only one temperature profile. Note that, for the *w* = 5 μm and θ = 45º case, the sensitivity to the width is concentrated at the non-illuminated side of the crack, whereas the sensitivity to the angle appears at the illuminated side.

4.2.5.   Experimental procedure

To carry out the experiments we used the same experimental set-up than in the previous section 4.1 (which is depicted in Figure 4.4). The laser is modulated using the optical chopper, and falls on the surface of one of the two blocks perpendicularly. The windowing of the IR camera is set to full frame, and the FR is set to 383 Hz (the maximum value at maximum windowing). The camera records approximately 15,000 images and they are processed in the lock-in module, so the average noise in the amplitude of the temperature is reduced down to $\sim$ 0.3 mK (see equation 2.12).

To test the validity of laser-spot lock-in thermography to measure the width and angle of tilted cracks we have manufactured inclined cracks with calibrated width and angle by sandwiching two metallic tapes of the same thickness (5, 10 and 20 μm) between two stainless steel AISI-304 wedged blocks (see Figure 4.17). Three block couples have been prepared with three wedge angles: 30º, 45º and 60º. Angles higher than 90º are obtained illuminating the other side of the crack, so the angle that is measured is the supplementary angle of 30º, 45º and 60º (150º, 135º and 120º). All surfaces in contact were polished to guarantee a good thermal coupling in the absence of tapes. Some pressure was applied to the blocks in contact to assure that the fissure width is close to the tapes thickness. A very thin graphite layer was deposited at the front surface of the coupled blocks to reduce the laser reflectivity and to enhance the infrared emissivity. Moreover, this graphite layer reduces surface heterogeneities, which disturb the amplitude profiles.
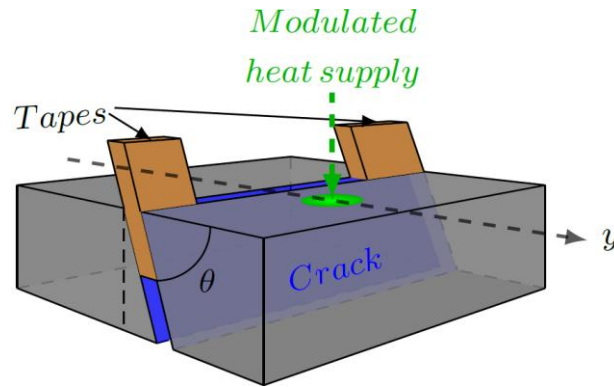
Figure 4.17: Diagram of the inclined crack used in the experiments: two thin metallic tapes of thickness *w* are sandwiched between two wedge blocks of AISI-304 stainless steel.

In order to retrieve the values of the crack width and angle, we fit the numerical model to the experimental temperature profiles along the *y*-axis, i.e. the straight-line perpendicular to crack and crossing the center of the laser spot. As it has been explained in Subsection 4.2.3, this temperature profile depends on the following parameters: D, $\eta P_o/K$, KR_{th}, a, f, l and θ. The thermal properties of the sample are known. The laser radius and the distance between the laser and the crack are measured optically, and the modulation frequency is selected by the researcher. Moreover, all experimental temperature profiles are normalized to the value at the center of the laser spot: $T_n(y)= T(y)/T(l)$, leading to $\eta P_o/K$ independent results.

Accordingly, the remaining two free parameters for the fitting procedure are: R_{th} and θ. Furthermore, R_{th} can be replaced by w (see equation 4.3), whose value is easier to quantitatively comprehend than that of the thermal resistence. The experimental profiles of the temperature amplitude are fitted to the model using a least-squares fitting procedure. For different values of w and θ, the root-mean-square error (RMSE) between the experimental data and the fitted curve is computed, and the pair (w, θ) which has the minimum value is taken as the result.

4.2.6.   Experimental results and discussion

In Figure 4.18 we represent the normalized experimental temperature profiles for the three angles (30º, 45º and 60º, left column) and their supplementary (150º, 135º and 120º, right column). For each angle four nominal crack widths (0, 5, 10 and 20 µm) have been studied. The case of 0 µm is obtained putting the two blocks directly in contact. Experiments have been performed at $f = 0.8$ Hz. For the sake of clarity, the normalized temperature profiles have been shifted vertically. Dots are the experimental results and the continuous lines are the fittings to the model.

The retrieved values of both parameters w and θ are shown in Table 4.1. As can be observed in Figure 4.18, using a nominal width $w = 0$ µm there is a clear jump in temperature for all angles, indicating that the thermal contact is not perfect, even though the two blocks are in direct contact.

The retrieved widths for $w = 0$ µm lie in the range 1.5 - 3 µm. These values are higher than those obtained for vertical cracks ($\theta = 90$º), which are typically lower than 1 µm [72]. This overestimation is caused by the fact that in the manufacturing process it is more difficult to keep the parallelism in wedge blocks than in orthogonal ones. In fact, this offset is kept for wider cracks: for nominal $w = 5$ the obtained values are in the range 6 - 9 µm, and for nominal $w = 10$ µm, the retrieved values are in the range 12 - 15 µm. Notice that the uncertainty in w is about 5% for angles smaller than 90º, which is remarkably low for this quantity. On the other hand, for $\theta > 90$º the uncertainty in w grows as the angle increases from 120º to 150º.

Regarding the angle, as can be observed in Table 4.1, all retrieved angles suffer from a deviation from the nominal value. For $\theta < 90$º there is a slight systematic overestimation, whereas for $\theta > 90$º the angle is underestimated. This deviation must be ascribed to the measurement procedure itself since, unlike the case of the width, the angle of the wedged blocks is manufactured with a precision better than 0.1º. Moreover, the uncertainty in θ is higher than the uncertainty in w, as it was predicted by the sensitivity analysis performed in subsection 4.2.4.
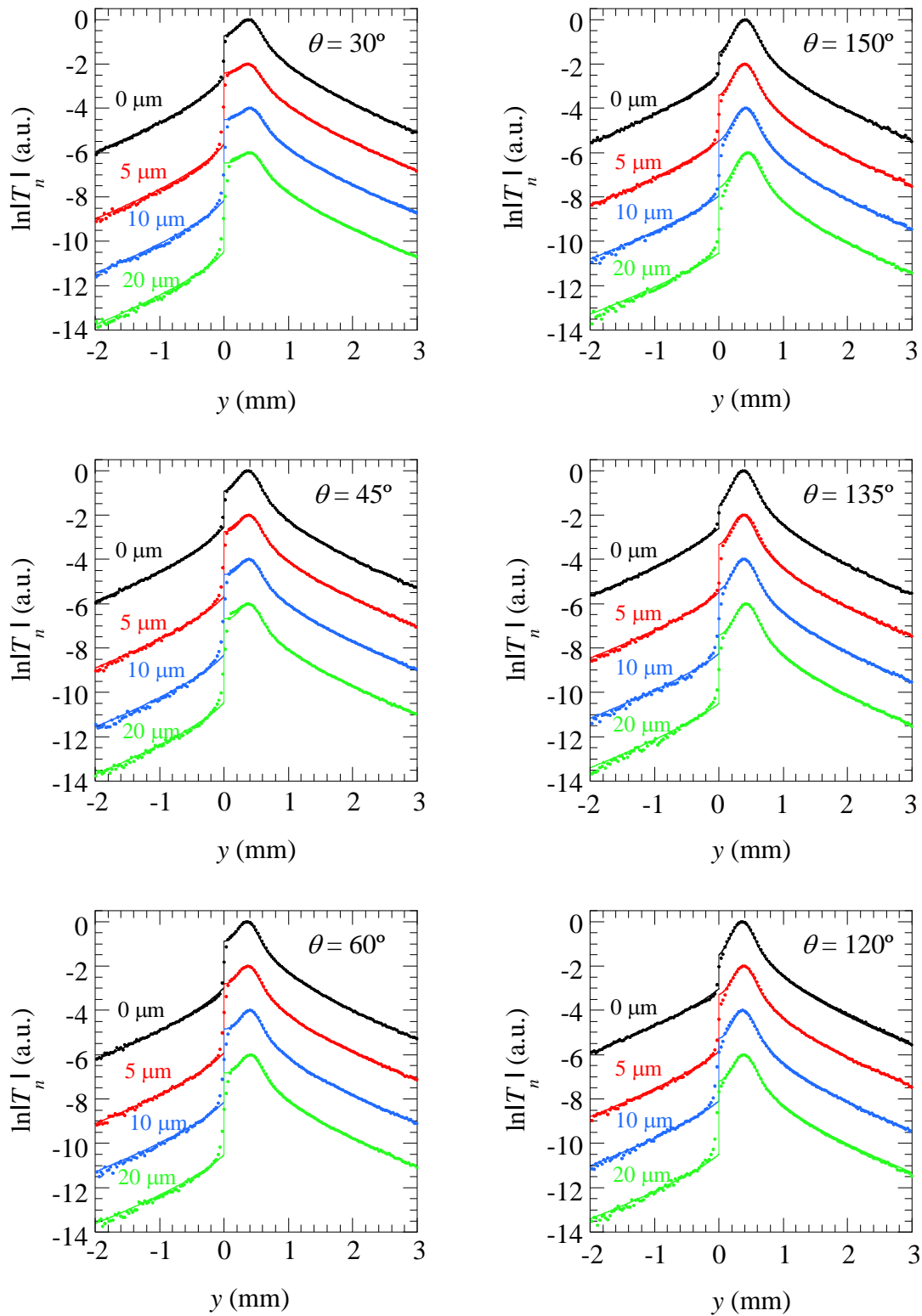
Figure 4.18: Normalized experimental $\ln|T_n|$ profiles at $f = 0.8$ Hz. Dots are the experimental results and the continuous line is the fitting to the model. For the sake of clarity, the profiles for different widths have been shifted. The values of the width and angle are the nominal ones.

Table 4.1: Summary of the obtained values of width and angle (w, θ) of the artificial inclined cracks dealt with in this work.

Angle	Nominal width			
	0 μm	5 μm	10 μm	20 μm
30°	$w = 2.2 \pm 0.2$ μm $\theta = 35 \pm 5°$	$w = 9.2 \pm 0.4$ μm $\theta = 30 \pm 3°$	$w = 15.2 \pm 0.6$ μm $\theta = 35 \pm 5°$	$w = 22.0 \pm 0.8$ μm $\theta = 35 \pm 5°$
45°	$w = 1.7 \pm 0.2$ μm $\theta = 50 \pm 3°$	$w = 7.7 \pm 0.3$ μm $\theta = 49 \pm 5°$	$w = 15.1 \pm 0.4$ μm $\theta = 48 \pm 5°$	$w = 18.5 \pm 0.8$ μm $\theta = 51 \pm 5°$
60°	$w = 3.1 \pm 0.2$ μm $\theta = 66 \pm 5°$	$w = 9.5 \pm 0.4$ μm $\theta = 62 \pm 3°$	$w = 12.2 \pm 0.6$ μm $\theta = 60 \pm 3°$	$w = 18.6 \pm 0.8$ μm $\theta = 62 \pm 3°$
120°	$w = 3.2 \pm 0.4$ μm $\theta = 150 \pm 6°$	$w = 8.7 \pm 0.4$ μm $\theta = 110 \pm 7°$	$w = 11.7 \pm 0.5$ μm $\theta = 110 \pm 7°$	$w = 18.0 \pm 1.0$ μm $\theta = 100 \pm 10°$
135°	$w = 2.3 \pm 0.5$ μm $\theta = 150 \pm 10°$	$w = 6.3 \pm 0.7$ μm $\theta = 120 \pm 10°$	$w = 13.9 \pm 1.3$ μm $\theta = 120 \pm 10°$	$w = 16 \pm 3$ μm $\theta = 110 \pm 15°$
150°	$w = 1.2 \pm 0.5$ μm $\theta = 130 \pm 10°$	$w = 7 \pm 4$ μm $\theta = 130 \pm 20°$	$w = 12 \pm 8$ μm $\theta = 135 \pm 15°$	$w = 20 \pm 11$ μm $\theta = 135 \pm 20°$

In order to visualize the origin of the higher uncertainty of the obtained values of w and θ for inclinations larger than 90°, we have plotted in Figure 4.19 the RMSE corresponding to two different fittings in Figure 4.18. Two cases are depicted, using the same width, $w = 10$ μm, and two angles: 45° and its supplementary, 135°.

In the case of $\theta = 45°$ we have plotted the RMSE values (black dots) obtained by fixing the value of the angle (taking values from 35° to 65°), and fitting the crack width. We proceed in the same way for $\theta = 135°$, plotting the RMSE values (red dots) obtained for fixed angle values (from 100° to 150°) and fitting the width as the only fitting parameter. As can be observed, for both angles there is a minimum corresponding to the couple (w, θ) which produces the best fitting of the experimental data. In the case of $\theta = 45°$ the minimum is sharp and well-defined, indicating a low uncertainty in the retrieved values of w and θ. On the other hand, for $\theta = 135°$ the minimum is located at a flat region, leading to a higher uncertainty in w and θ.

These evidences bring us to conclude that the optimum configuration to determine the crack inclination and width consists in exciting the side that is above the inclined crack. In these conditions, reliable and precise values of both the width and angle with the surface can be retrieved, although the value of the angle is slightly overestimated.
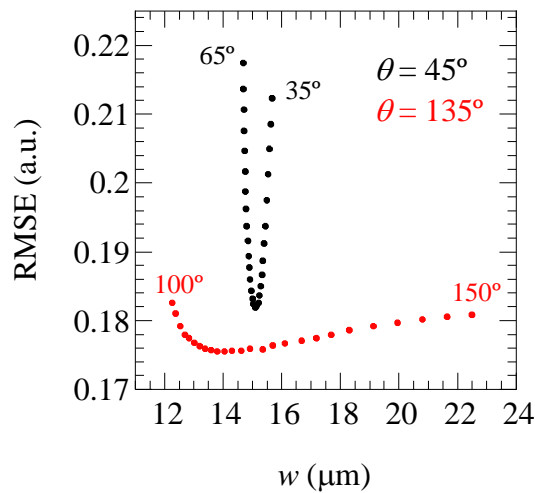

Figure 4.19: RMSE values corresponding to the fittings in Figure 4.16 for $w = 10$ µm and two complementary angles: 45º (black dots) and 135º (red dots).

4.2.7.   Conclusions

The presented method has been proven as an efficient contactless and quantitative tool to determine the width and inclination of infinite surface breaking cracks. This methodology involves the fitting of the amplitude of the surface temperature oscillation obtained using FEM to experimental laser-spot lock-in thermography data.

The sensitivity analysis based on FEM confirms that, using the amplitude profile perpendicular to the crack that crosses the center of the laser spot, the width and inclination of the crack are not correlated, and therefore both parameters can be obtained simultaneously from a single amplitude thermogram. We have tested the validity of the method by making laser-spot lock-in thermography measurements on

samples containing artificial and calibrated tilted cracks, making different angles with the surface, with values between 30º and 150º. The results show that the crack width is retrieved with high accuracy and, as predicted by the sensitivity analysis, the uncertainty in the retrieved width is smaller than in the angle.

The uncertainty in the retrieved width is small (less than 5%) for angles smaller than 135º, although for angles above 135º the uncertainty increases. On the other hand, the uncertainty in the retrieved angle is more affected by the value of the angle: it is about 5º for angles smaller than 90º (when the laser beam is located above the crack) and it increases for increasing angles above 90º. Furthermore, the value of the angle is retrieved accurately when the inclination with the surface is less than 90º, but it is underestimated if the crack is tilted towards the non-excited side.

In conclusion, in order to determine the width and orientation of the crack accurately it is advisable to excite the sample surface region that is above the crack, so the angle with the surface is smaller than 90º. The orientation of the crack might be unknown before any inspection, so the proposed protocol is the following: excite one side of the crack and, if the retrieved angle is higher than 90º, repeat the procedure exciting the other side of the crack. By proceeding this way, accurate and precise values of the crack width and inclination can be obtained.

Finally, we have to state that the FEM code used in this study can be implemented to deal with more realistic situations, including finite tilted cracks and/or dealing with heat losses by convection and radiation that might be significant when analyzing cracks in low conductivity materials. In fact, the next section will be centered in the case of finite in depth cracks in a real metallic plate, and FEM will also be used.

4.3. Cracks in real samples: detection and sizing the width and depth

4.3.1. Introduction

As it has been observed in the two previous sections, when laser spot thermography is used in the case of surface-breaking cracks, an abrupt temperature discontinuity along the length of the fissure appears in the thermogram, revealing the presence of the crack.

A challenging task is the evaluation of the width and depth of the detected crack. A convenient simplification to model the surface temperature is to consider an infinite vertical crack, for which the surface temperature can be calculated analytically. For this ideal case, the width of the crack can be determined by fitting the prediction of the analytical model to experimental temperature data obtained by using a modulated [72] (which is the approach used in Section 4.1), a pulsed [81] or a continuously moving laser spot [82].

In the more realistic case of an in-depth finite vertical crack the surface temperature must be obtained numerically. Finite Elements Methods (FEM) have been used to solve the heat diffusion equation to simulate the surface temperature of a sample containing a finite crack [83-93]. However, the requirement of applying sufficiently fine meshes in the crack and the surrounding material to obtain reliable solutions to the transmission problem through the air filling the crack has limited the application of laser-spot thermography to cracks wider than about 40 μm.

As it has been introduced in the previous Section 4.2, for narrow cracks the FEM can be

carried out considering the crack as a surface characterized by a thermal resistance. The same methodology will be applied to size the width and depth of finite cracks.

In this section, we show that by combining FEM and laser spot lock-in thermography it is possible to determine the distribution of the width and depth of very narrow surface breaking fatigue cracks along its length. These early-stage cracks are very challenging flaws, even at the pure detection stage, for any nondestructive testing technique. With the aim of achieving not only the detection but, most interestingly, the characterization of very narrow cracks, we will use lock-in thermography due to the ability of the lock-in procedure to reduce the noise level far below the thermal sensitivity of any state of the art infrared camera (20 mK).

4.3.2.   Objectives

The main objectives of this section are:

- To detect the presence of cracks in a real metallic part, revealing its position, length and surface trace, using laser-spot lock-in thermography.

- To perform a sensitivity analysis to verify if the crack width and depth are uncorrelated, and therefore they can be obtained simultaneously from the same unique measurement.

- To fit the FEM model to experimental data obtained from laser-spot lock-in thermography experiments performed on a real plate containing a finite in-depth fatigue crack

- To achieve a complete characterization of the crack by retrieving the values of crack width and depth at different positions of the crack.

4.3.3.   Theoretical analysis and numerical calculations

As it has been stated in the previous sections, a very convenient configuration to detect and characterize a surface breaking crack is to focus a modulated laser beam close to the crack and record the surface temperature oscillation using an IR video camera (laser-spot lock-in thermography). Figure 4.20 shows the configuration, where *l* is the distance between the center of the laser spot and the crack, *w* and *d* are the width and depth of the crack, respectively.
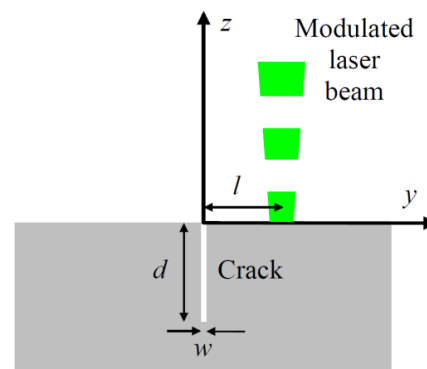

Figure 4.20: Cross section of the sample with a vertical surface breaking crack.

As in previous sections, the laser beam has a Gaussian profile, it is focused down to a radius *a* , with power P_o and modulated at a frequency f ($\omega = 2\pi f$). The center of the laser spot is located on the *y*-axis (0,*l*,0).

Accordingly to the definition of the thermal diffusion length $\left(\mu = \sqrt{\dfrac{D}{\pi f}} \right)$, two cases can be considered:

- if $\mu < d$, the crack acts as infinite in depth and only the width of the crack can be retrieved

- if $\mu \geq d$, the crack behaves as finite in depth and, therefore, both *d* and *w* can be obtained

As, for a given specimen, the thermal diffusion length depends on the modulation frequency, an appropriate selection of *f* allows the crack to be studied as infinite or finite.

A.   In-depth infinite vertical cracks

Regarding the infinite in depth case, when adiabatic boundary conditions at the sample surface are assumed, an analytical expression for the surface temperature can be obtained. The temperature at both sides of the crack is given by equation (4.1) in Section 4.1. It is important to remark that in that section we have demonstrated the excellent quality of the fittings of this analytic model to experimental data.

In Figure 4.21 we show the calculations of the natural logarithm of the amplitude of the temperature profile along the *y*-axis for an Al- alloy sample ($D = 42$ mm^2/s, $K = 100$ Wm^{-1}K^{-1}), which is illuminated by a Gaussian laser beam of radius $a = 0.2$ mm, whose center is located at a distance $l = 0.4$ mm from the crack. The laser power is $P_o = 1$ W and the modulation frequency is $f = 5$ Hz. As we are interested in the early detection and characterization of fatigue cracks, we focus our analysis on very narrow cracks, and these three crack widths are analyzed: $w = 0.1$, 1 and 2 μm. Note that a crack as narrow as 0.1 μm produces a measurable temperature jump. This is due to the high thermal conductivity of the Al-alloy.
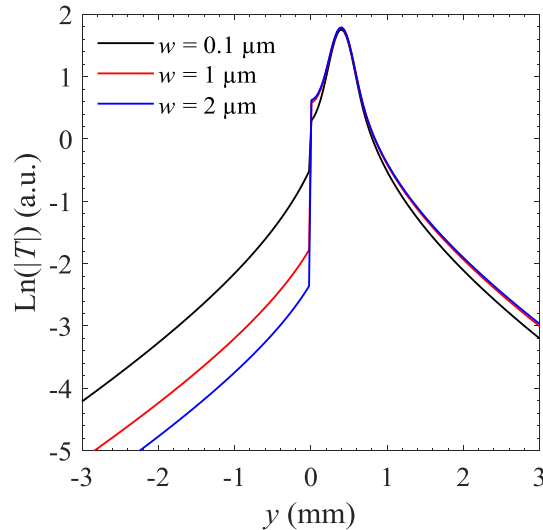

Figure 4.21: Calculations of ln|*T*| as a function of the transverse distance to the crack, which is located at *y* = 0, for an infinite in depth crack. Calculations have been performed for an Al-alloy sample ($D = 42$ mm^2/s, $K = 100$ Wm^{-1}K^{-1}) with $P_o = 1$ W, $f = 5$ Hz, $a = 0.2$ mm and $l = 0.4$ mm. Three widths are analyzed (0.1, 1 and 2 μm).

B.   In-depth finite vertical cracks

As it has been explained, real cracks behave as infinite in-depth when high frequencies are used, but in that case it is not possible to retrieve the depth. To quantify the crack penetration, low frequencies are needed, but the crack does not behave as infinite anymore, so numerical calculus has to be used.

We have already studied in Section 4.2 a particular case of infinite cracks that have a certain inclination with respect to the surface plane. Now, we will make use of a code elaborated in our research group to analyze vertical cracks with finite depth, solving equations (4.4.) to (4.7) for this geometry. In Figure 4.22 we show a schematic view of the domain where the FEM are applied, where the vertical finite crack can be seen colored in blue.
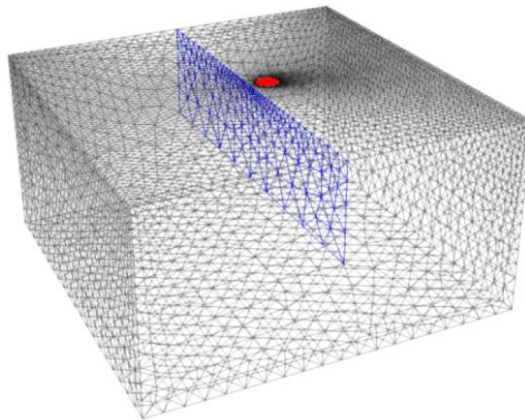

Figure 4.22: Triangulation of the investigated sample domain. The crack is depicted in blue as a 2-D interface, whereas the laser heat supply is depicted as a red circle. For the sake of clarity, only the surface mesh is represented.

In order to illustrate the effect of a crack of finite penetration on the surface temperature, in Figure 4.23 we show simulations of $\ln(|T|)$ along the y-axis for the same aluminum sample, ($D = 42$ mm^2/s, $K = 100$ Wm^{-1}K^{-1}), which contains an in-depth finite crack. We used the same experimental parameters than the infinite case ($P_o = 1$ W, $f = 5$ Hz, $a = 0.2$ mm and $l = 0.4$ mm). Three different couples (w, d) are analyzed.

First of all, we compute the simulation for a 1 μm wide surface-breaking crack penetrating 0.5 mm vertically (black curve). In order to analyze the impact of variations

of both parameters on ln(|T|), we change the depth, doubling its value, while keeping fixed the width (w = 1 μm, d = 1 mm), which corresponds to the red curve. As can be observed, doubling the depth produces a displacement of ln|T| downwards at the non-illuminated side of the crack, almost parallel to the black curve.

Then we come back to the initial depth while doubling the width of the crack (w = 2 μm, d = 0.5 mm), which corresponds to the blue curve. Note that doubling the width of the crack only produces a small deviation downwards of the curve at the non-illuminated side, close to the crack, whereas further away the blue and black lines remain almost indistinguishable. These results indicate that ln|T| is more sensitive to d than to w for narrow cracks. Accordingly, it is expected that the depth will be quantified with higher precision than the width.
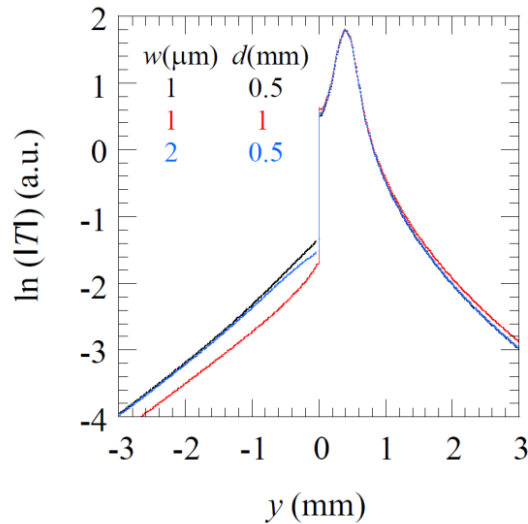
Figure 4.23: Simulations of ln|T| as a function of the transverse distance to the crack, which is located at y = 0. Simulations have been performed for an Al-alloy sample (D = 42 mm^2/s, K = 100 Wm^{-1}K^{-1}) with P_o = 1 W, f = 5 Hz, a = 0.2 mm and l = 0.4 mm. Three couples (w, d) are plotted.

Nevertheless, it remains the question of whether both magnitudes, w and d, are correlated, i.e. whether the same temperature profile can be reproduced by several couples (w, d). In order to address this issue, we have calculated the sensitivity of ln|T| to w and d according to the following expression (already used in Section 4.2):

$$S_j = j \ \frac{\partial \ln(|T|)}{\partial j} \ , \ \ j = w, d \tag{4.9}$$

In Figure 4.24 we plot the sensitivity of the *y*-profile to both parameters in the case of a crack with $w = 1$ μm and $d = 0.5$ mm. The black curve is the sensitivity to the width (S_w) and the red curve is the sensitivity to the depth (S_d).

As can be observed, the sensitivity to both parameters is very low at the illuminated side of the crack ($y > 0$), but it is noticeable at the non-illuminated side. Moreover, it can be observed that both quantities are not correlated, because their sensitivities are not proportional. Consequently, *w* and *d* can be obtained univocally from only one temperature profile. Furthermore, it is confirmed that $|S_d| > |S_w|$, as it could be observed in Figure 4.23.
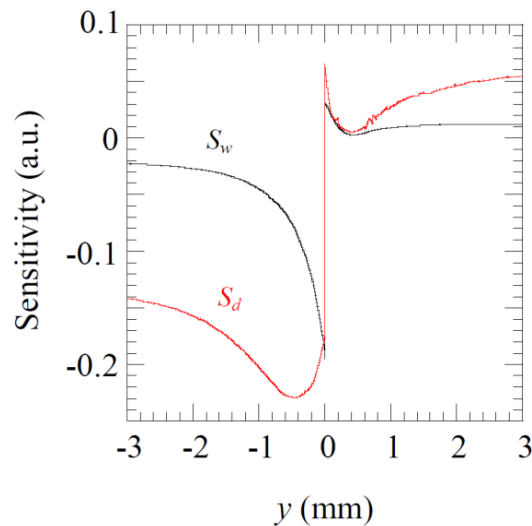
Figure 4.24: Simulation of the sensitivity of $\ln(|T|)$ to *w* and *d* for the same parameters used in Figure 4.23, for $w = 1$ μm and $d = 0.5$ mm.

4.3.4.   Experimental procedure and crack detection

In order to perform the experiments we used the same experimental set-up than in the previous two Sections 4.1 and 4.2, which is depicted in Figure 4.25 for the sake of remembering. The laser is modulated using the optical chopper, and it illuminates the surface of the sample near the crack. The windowing of the IR camera is set to full

frame, and the FR is set to 383 Hz. The camera records approximately 15,000 images and they are processed in the lock-in module, so the average noise in the amplitude of the temperature is reduced down to ~ 0.3 mK (see equation 2.12).

Figure 4.25: Scheme of the experimental set-up

The sample is a dog bone plate 2 mm thick made of an aluminum alloy named Al-2034, which thermal properties are $D = 42$ mm^2/s, measured in the laboratory using lock-in thermography, and $K = 100$ Wm^{-1}K^{-1}, a value obtained from the alloy density and specific heat of similar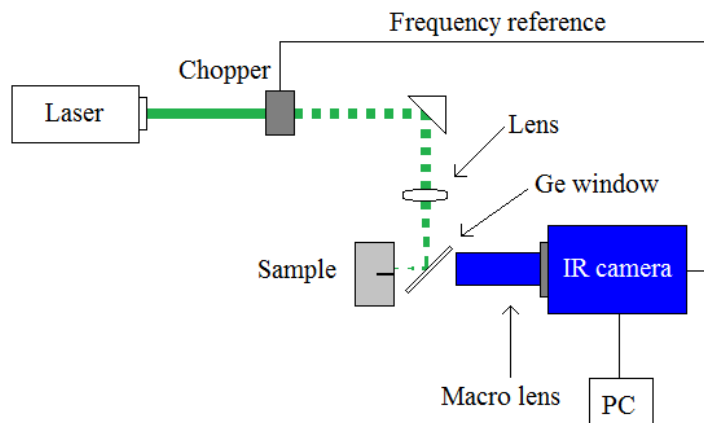 aluminum alloys. In the middle of the sample there is a 5 mm diameter drilled hole, as it can be seen in Figure 4.26a. Before its acquisition in our laboratory, this plate was subjected to successive compression and tension cycles to test its mechanical resistance to fatigue. Therefore, it was expected that some fissures were produced around the hole during this process.

A close-up photograph of the sample is shown in Figure 4.26b. It is a close-up of the region of the hole and it is rotated 90º to the right with respect to Figure 4.26a. As can be seen, there are many lines at the surface and it is difficult to distinguish whether they are just surface scratches or surface breaking cracks that could affect the integrity of the piece. Accordingly, the first goal is to assess which of those lines are cracks and the second, more challenging one, is to size their width and depth. A very thin graphite layer is deposited at the illuminated surface of the plate to enhance both the laser light absorption and the IR emissivity.
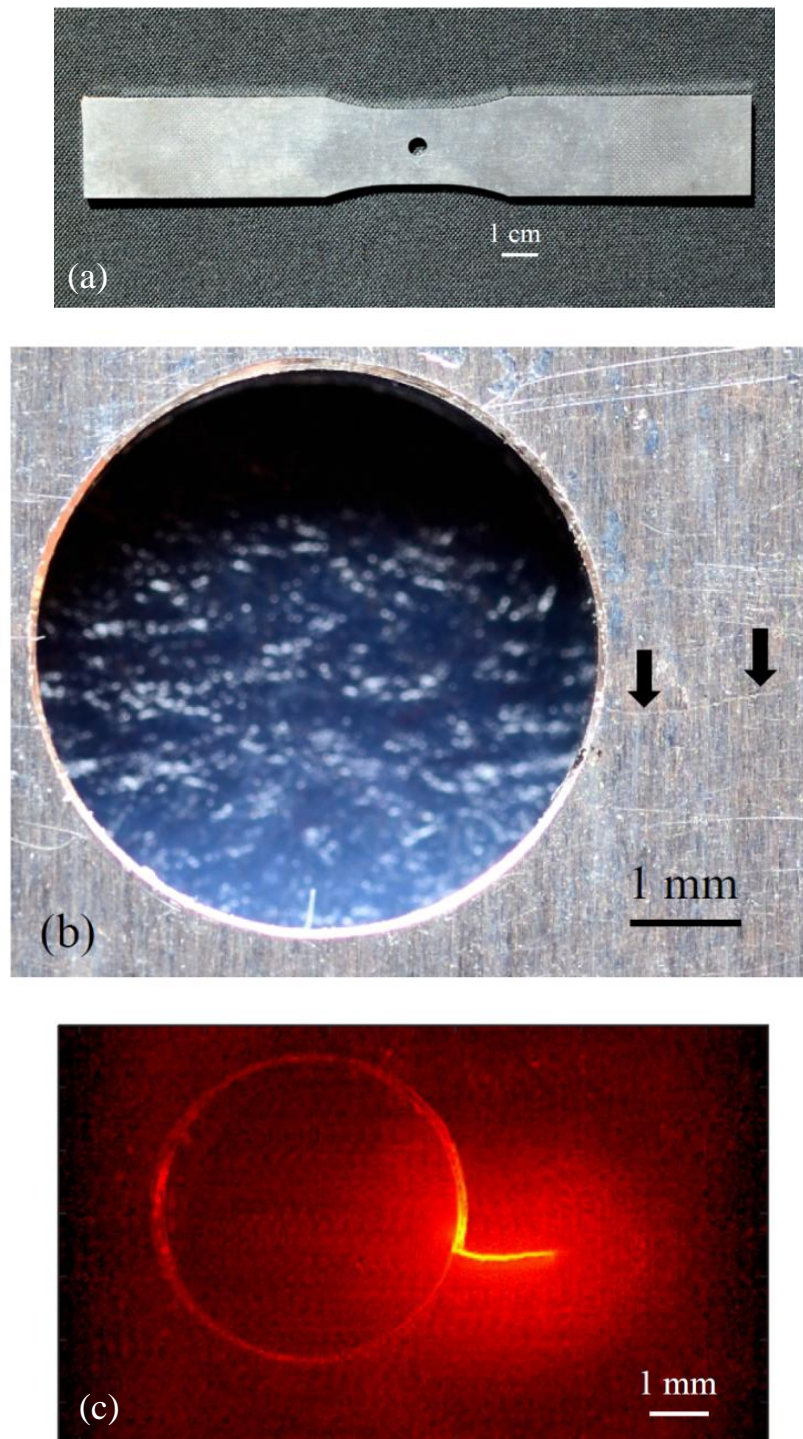
Figure 4.26: (a) Photograph of the dog bone Al-alloy plate. (b) Close-up picture of the sample around the hole. Arrows indicate the position of the crack. (c) Combined first derivative thermal image of the crack.

In order to detect the crack and to obtain a qualitative image of it, we follow a similar methodology than the one proposed by Almond and coworkers in 2011 [94,95]. First, we obtain several temperature amplitude thermograms at different positions of the laser spot, keeping fixed the modulation frequency in all of them. Then, we compute the first spatial derivative along the *x*-axis and along the *y*-axis of each amplitude thermogram. For each position of the laser we generate a new image by adding the squares of the first derivative images in *x* and *y* directions to show the derivative information in both directions simultaneously. Finally, we combine all the first derivative images obtained at different positions of the laser spot (Figure 4.26c). It can be observed that, apart from the hole perimeter, which is technically a thermal barrier, only one of the surface lines is confirmed as a crack. It is the one marked by arrows in the optical picture in Figure 4.26b. Therefore, the other lines are mere surface scratches with no depth penetration, as none of them appears as bright regions in the thermogram of derivatives in Figure 4.26c.

To size the depth and width of the confirmed crack we focus the laser spot close to the crack ($\approx$ 0.4 mm) at seven positions covering the whole length of the fissure. For each position, we record the temperature amplitude and the vertical profile is selected, as it is shown in Figure 4.27.

In the next section, these profiles will be evaluated using both the infinite (analytic) and the finite in-depth (numerical) models explained in the theoretical calculations subsection, considering that we have no knowledge of the penetration of the crack.
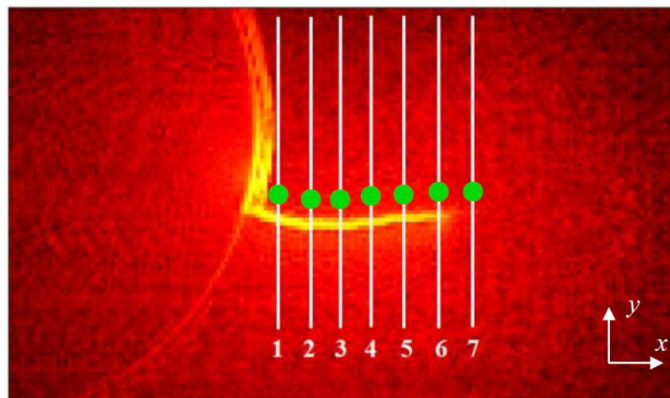

Figure 4.27: Position of the seven profiles that have been fitted to obtain the width *w* and the depth *d* of the crack. The green dots show the successive positions of the laser spot.

4.3.5. Crack sizing and discussion

Figure 4.28 shows by dots the temperature amplitude *y*-profile corresponding to position 1 (see Figure 4.27) for two modulation frequencies: 53.8 Hz (a) and 11.2 Hz (b). As a first attempt, the crack is assumed to be an infinite in-depth fissure, so we fitted the profiles to equation 4.1, which involves less computational cost and time. The results of the fittings are the continuous lines in Figure 4.28.

Figure 4.28: Experimental ln|T| profiles corresponding to position 1 in Figure 4.27 for two modulation frequencies. Dots are the experimental results and the continuous line is the fitting to equation 4.1.

As it has been done in section 4.1, in this procedure we consider a, l, P_o and R_{th} as the free parameters to be fitted. The first three are set by the user and can be measured optically, but their fitting allows us to verify the consistency of the fit. From the fitted R_{th}, the air gap width of the crack w is obtained using the relation $R_{th} = w / k_{air}$ (equation 4.2).

As can be observed, the quality of the fit is very good for 53.8 Hz, leading to a retrieved crack width $w = 1.5 \pm 0.2$ μm. On the other hand, if we observe the left branch of the profile at 11.2 Hz, it is clear that the model does not follow the data trend: the temperature jump is underestimated, the model curve has a convex shape and the experimental data follow a more concave trend. Here, the estimated width is 0.6 ± 0.2 μm.

This behavior can be understood by analyzing the thermal diffusion length for each frequency: μ = 0.5 mm at the higher frequency and μ = 1.1 mm at the lower frequency. At 53.8 Hz the fitting is very good indicating that the actual depth of the crack is higher than 0.5 mm, and thus the crack behaves as infinitely deep at this frequency. On the contrary, the bad fitting at 11.2 Hz indicates that the depth of the crack verifies $d \leq 1.1$ mm, and the infinite crack model does not describe the effect of the crack on the surface temperature. According to this, relatively low frequencies will be used, so the thermal diffusion length is larger than the crack depth.

In order to obtain both the width and depth of the crack, we use FEM to fit the amplitude profiles. These profiles depend on the following parameters: D, $\eta P_o/K$, KR_{th}, a, f, l and d. The thermal properties of the sample are known. The laser radius and the distance between the laser and the crack are measured optically, and the modulation frequency is selected by the researcher. Moreover, all experimental temperature profiles are normalized to the value at the center of the laser spot: $T_n(y)= T(y)/T(l)$, leading to $\eta P_o/K$ independent results. Accordingly, the remaining two free parameters for the fitting procedure are: R_{th} and d. Furthermore, R_{th} can be replaced by w (see equation 4.2), whose value is easier to quantitatively comprehend than that of the thermal resistence.

In Figure 4.29 we show the temperature profiles corresponding to position 1 in Figure 4.24 at three modulation frequencies fulfilling the mentioned criterion: 11, 5 and 2 Hz, for which the thermal diffusion lengths are 1.1, 1.6 and 2.6 mm, respectively. The same vertical scale has been used for a better comparison of the profiles at different frequencies. Dots are experimental data and the red lines are the best fitting curves. For the three frequencies we obtained the same values of the parameters: w = 1.5 ± 0.3 μm and d = 0.70 ± 0.05 mm. Note that, as predicted by the sensitivity analysis, the uncertainty in depth ($\approx$ 7%) is smaller than the uncertainty in width ($\approx$ 20%).
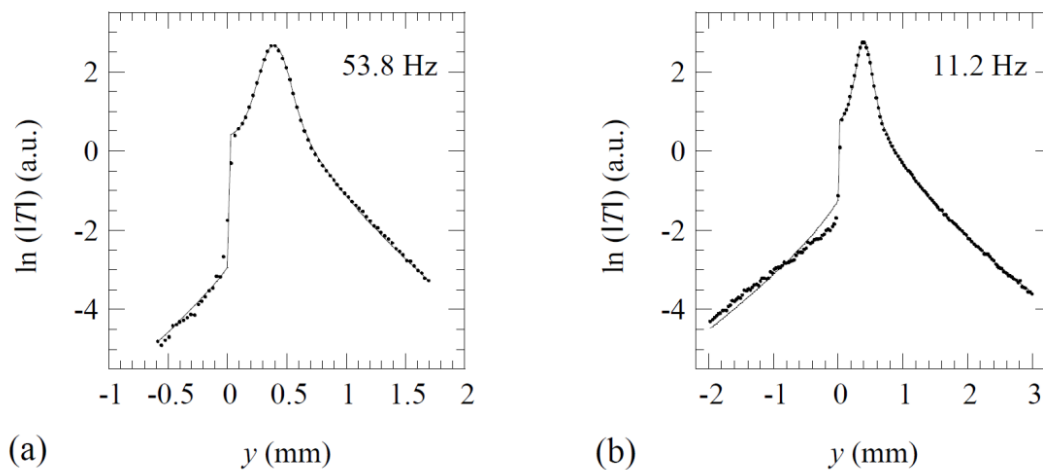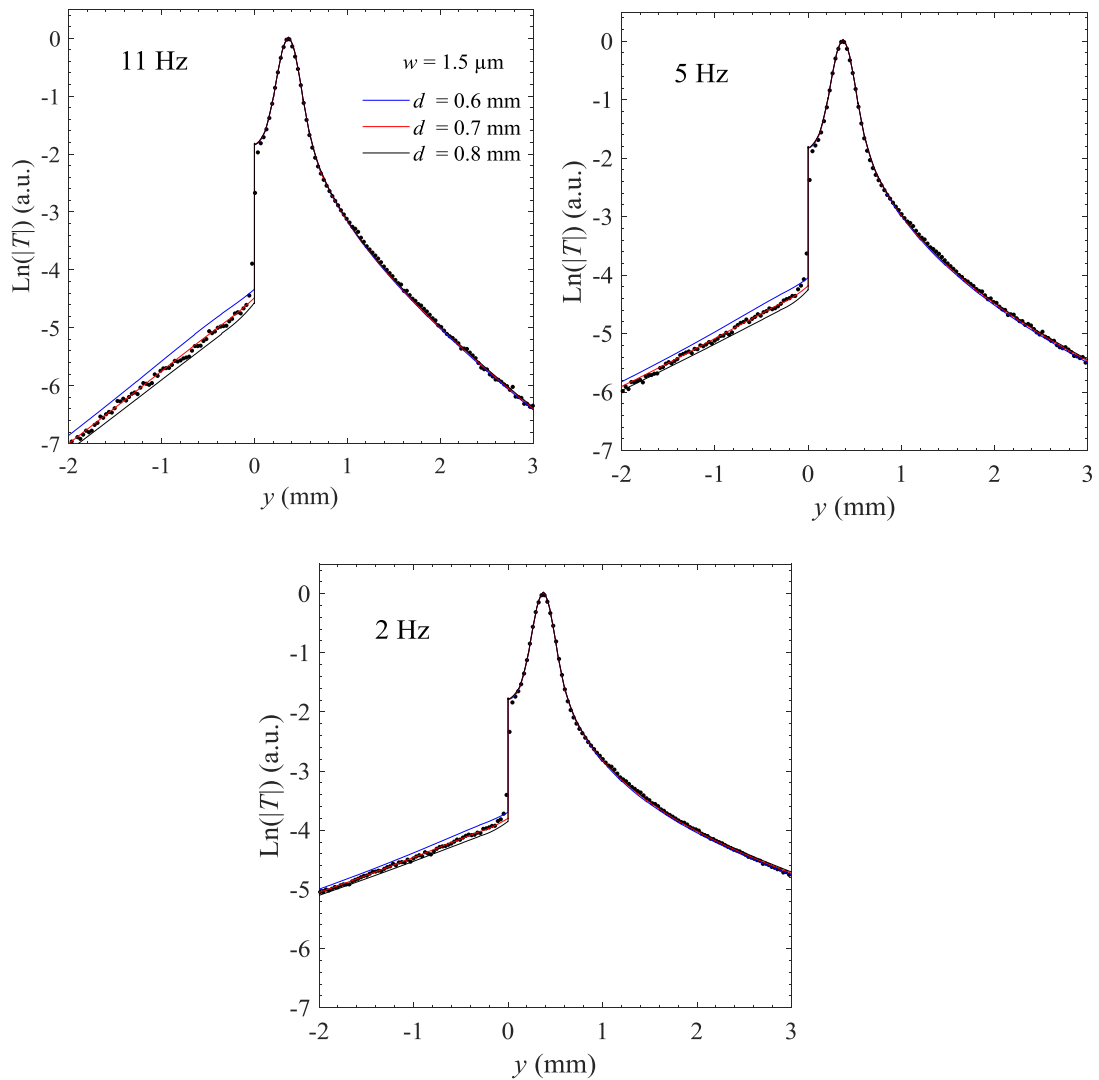
Figure 4.29: Experimental ln|T| profile corresponding to position 1 in Figure 4.24 for low modulation frequencies. Dots are the experimental results and the continuous red line is the fitting to FEM. The vertical scale is kept fixed for a better comparison of the profiles.

Moreover, for each frequency we have plotted the temperature profiles for two depths covering the range of the uncertainty: $d = 0.8$ (black curve) and 0.6 mm (blue curve) to better appreciate the resolution of the method. As can be observed, when reducing the modulation frequency the signal to noise ratio is increased, but the sensitivity is reduced: the profiles are less distinguishable. Consequently, the recommended procedure to measure w and d is to avoid high frequencies, for which the crack behaves as infinitely deep, and also avoid low frequencies, for which $\mu \gg d$, since the resolution is notably reduced. Actually, the best tradeoff is to select a frequency verifying $\mu \approx d$.

The same analysis has been performed for the remaining of the positions in Figure 4.27 (positions 2 to 7). The results are plotted in Figure 4.30, indicating that for the first 0.7 millimeters in the *x* direction (following the length of the fissure) the depth and width of the crack have a nearly constant value and then both are reduced until the fissure vanishes at $\approx$ 1.7 mm.
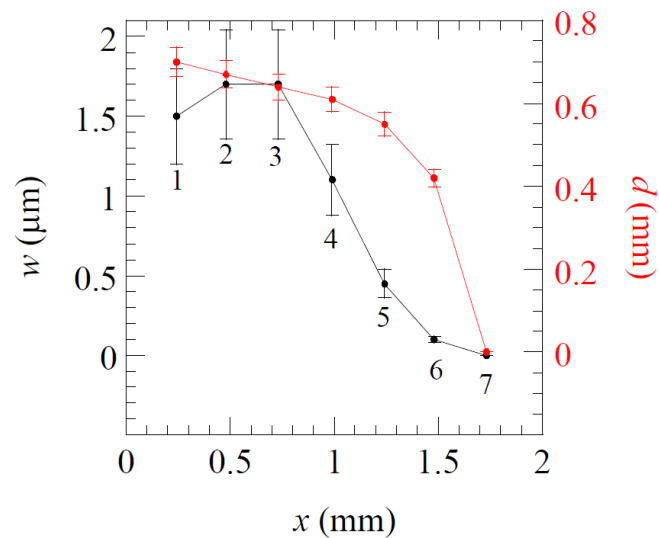
Figure 4.30: Fitted values of the width and depth of the crack for each of the seven positions marked in Figure 4.24. The variable *x* corresponds to the distance to the hole. The lines are a guide for the eye.

As a final remark, the crack growth could be studied by repeating this IR thermography technique as the number of cycles of compression and expansion is increased, obtaining the relation between crack size and number of cycles, which can be of interest for industrial applications to assess the condition of the metallic part.

4.3.6.   Conclusions

In this section, we have shown that laser spot lock-in thermography features a high enough sensitivity to image narrow early-stage fatigue cracks, and distinguish between real cracks and superficial scratches.

Moreover, we have experimentally demonstrated that combining calculations based on discontinuous finite elements and laser spot lock-in thermography it is possible to determine values of the crack width and depth locally, at different positions along the crack length, for cracks as narrow as $\approx$ 1 µm in an aluminum alloy sample. The simulations show that even 0.1 µm wide cracks can be analyzed in this material.

The results yielded maximum values of the crack width and depth of 1.5 µm and 0.7 mm, respectively. To the best of our knowledge, this is the first time that the distribution of the width and depth of a real crack is determined, and that cracks as narrow as 1.5 µm are sized.

This technique provides the full characterization of the length, width and depth of the crack, and therefore it provides an opportunity to analyze the growing of the crack in fatigue tests by performing the study at several stages during the test.

Finally, the efficiency of the method could be improved if the inspection time is reduced. This can be achieved by scanning the laser spot along the sample surface (flying-spot thermography). Therefore, the next step in this study would be to combine calculations of the surface temperature by means of finite elements with flying spot thermography to detect and characterize narrow finite cracks in a fast way.

5. Conclusions and future work

The most important conclusions of the work developed and presented in this thesis are summarized in this chapter.

Regarding the research on new configurations used to measure the thermal diffusivity:

- It has been demonstrated that the thermal diffusivity can be measured using a non-expensive system and applying a very simple processing. A low cost configuration, ideated to be composed by an entry level IR camera and a low-end laser, was proposed to measure D in all kinds of materials (thick and thin samples, and opaque and transparent materials) using continuous illumination. A wide range of diffusivities was investigated. A simple circular average applied to the raw thermograms allowed to clean the noise almost like in lock-in post-processing. D has been measured with very low uncertainty (3-5%).

- We have demonstrated that D can be measured using continuous illumination for moving samples, taking advantage of the whole amplitude thermograms. A direct application of this method allowed us to measure the diffusivities along the principal directions of an anisotropic material, together with determining the angle between the sample principal axes and the movement direction when it is an unknown parameter. The diffusivity has been measured with very low uncertainty, (around 5-10%). The orientation of the principal directions in anisotropic samples was determined with high accuracy ($\pm$ 1°). This might be significantly useful for in-line quality control of anisotropic materials in which the principal directions make arbitrary and unknown angles with the motion of the chain.

- Thermal diffusivity was measured in moving samples using laser-spot modulated illumination and lock-in post-processing. The slope values retrieved from the longitudinal and transverse profiles led to reliable and precise values of *D*, with an uncertainty lower that 10%, covering a wide range of sample properties: from thin to thick, from opaque to semitransparent, and from poor to good thermal conductors.

- Comparing the last two methods, which involve laser-spot illumination in moving samples, the continuous illumination procedure offers more generality, a simpler post-processing (no use of a lock-in module) and the ability to measure the *D* and the principal directions of anisotropic materials. Therefore, it may be more appropriate than the modulated illumination procedure, although the last one also delivered very good results, as well as it showed for the first time a decoupling between amplitude and phase.

Concerning the crack characterization:

- A new procedure was proposed to measure thermal conductivity of fluids applying the infinite in-depth crack analytical model, using laser-spot modulated illumination. Taking different calibrated gaps between two blocks and applying the relation $R_{th} = w/k_{fluid}$, three fluids (air, water and ethylene glycol) have been tested, obtaining excellent results, with an uncertainty of about 5%. A great advantage of this method is the small quantity of fluid that is needed: around 1-2 mm^3.

- Surface-breaking infinite in-depth tilted cracks were characterized using calibrated stainless steel blocks. Lock-in post-processing was applied to the measurements obtained from laser-spot modulated illumination. Both parameters of interest, the width of the crack and the inclination angle, were measured with low uncertainty, proving the validity of the method.

- We have demonstrated that the width and depth of real cracks can be determined locally. In particular, a narrow crack, indistinguishable from superficial scratches at plain sight, was detected and imaged for a real metallic part. Moreover, its width and depth were sized accurately using FEM fitted to the experimental data obtained from laser-spot lock-in thermography.

In conclusion, in this thesis we have presented contributions to active IRT research in the particular field of thermal diffusivity measurement, proposing new procedures and revisiting or improving other methods, and also in terms of defect detection and characterization, offering new tools to characterize surface-breaking cracks, especially in the case of sizing narrow cracks.

These conclusions lay the grounds for future research. Interests now focus, on one hand, on characterization of a real crack as it evolves through time, that is, follow the progression of the crack as it is put under fatigue cycles, so its length, width and penetration can be measured as it changes in real time. This could be achieved by placing the measuring system (laser + camera) near the sample that is being tested in the fatigue procedure. This combination would be of important interest for industrial applications.

On the other hand, the crack characterization issue can be complemented by using a flying-spot configuration, so the sample is at rest and the laser-spot scans it. A flying-spot mechanism is expected to be acquired in the laboratory, so a fast characterization of cracks and fissures could be accomplished.

Moreover, other future projects derived directly from this thesis involve the characterization of cracks with a more general shape, starting with the quantification of width, angle and depth simultaneously, and continuing with arbitrary shapes and positions. Furthermore, although in Chapter 4 we have focused on cracks and fissures, other defects in materials may be studied, like it is the case of delaminations, cavities or corrosion.

List of publications

Research activity for this thesis has resulted in the publications below:

- A. Salazar, L. Zamanillo, M. Colom, A. Mendioroz, U. Galietti, A. Sommier, J.C. Batsale and C. Pradere, "Lock-in thermography on moving samples: amazing mismatch between amplitude and phase", *QIRT J.* **17**, 279 (2020).

- A. Bedoya, M. Colom, A. Mendioroz, A. Salazar and E. Marín, "Measurement of the thermal conductivity of fluids using active lock-in thermography", *Measurement* **158**, 107740 (2020).

- M. Colom, A. Bedoya, A. Mendioroz and A. Salazar, "Measuring the in-plane thermal diffusivity of moving samples using laser spot lock-in thermography", *Int. J. Therm. Sci.* **151**, 106277 (2020).

- M. Colom, J. Rodriguez-Aseguinolaza, A. Mendioroz and A. Salazar, "Imaging real cracks: evaluation of the depth and width of narrow fatigue cracks in and Al-alloys using laser-spot lock-in thermography", *Proc. of SPIE*, **11743F** (2021).

- A. Salazar, M. Colom and A. Mendioroz, "Determining the thermal diffusivity and the principal directions on anisotropic moving samples with laser-spot thermography", *Int. J. Heat Mass Transf.* (in press, 2021).

Publications pending acceptance:

- M. Colom, J. Rodríguez-Aseguinolaza, A. Salazar and A. Mendioroz, "Sizing the depth and width of narrow cracks in metallic parts by laser spot lock-in thermography", *NDT&E Int.* (submitted).

- J. Rodríguez-Aseguinolaza, M. Colom, J. Gonzalez, A. Mendioroz and A. Salazar, "Quantifying the width and angle of inclined cracks using laser-spot lock-in thermography", *NDT&E Int.* (submitted).

- A. Salazar, M. Colom and A. Mendioroz, "Laser-spot step-heating thermography to measure the thermal diffusivity of solids", *Int. J. Therm. Sci.* (submitted).

In addition, the work has been presented in the conferences below:

- A. Salazar, L. Zamanillo, M. Colom and A. Mendioroz, "Unexpected mismatch between amplitude and phase in lock-in thermography on moving samples", 20th International Conference on Photoacoustic and Photothermal Phenomena, Moscow (Russia), 2019. Invited conference.

- M. Colom, J. Rodríguez-Aseguinolaza, A. Mendioroz and A. Salazar, "Sizing the width and depth of real cracks using laser spot lock-in thermography", 15th Conference on quantitative infrared thermography, Porto (Portugal), 2020. Oral.

- M. Colom, J. Rodríguez-Aseguinolaza, R. Celorrio, A. Mendioroz and A. Salazar, "Evaluation of the length, penetration and width of early stage fatigue cracks in light metals using laser spot lock-in thermography", 12th International Symposium on NDT in Aerospace, Williamsburg, Virginia (USA), 2020. Oral.

- M. Colom, J. Rodriguez-Aseguinolaza, A. Mendioroz and A. Salazar, "Imaging real cracks: evaluation of the depth and width of narrow fatigue cracks in and Al-alloys using laser-spot lock-in thermography", SPIE Defense and Commercial sensing. Thermosense Thermal Infrared Applications XLIII, Orlando, Florida (USA), 2021. Oral.

References

[1]   W. Herschel, "XIV Experiments on the refrangibility of the invisible rays of the sun", *Phil. Trans. R. Soc.* **90**, 284 (1800).

[2]   X. P. V. Maldague, *Nondestructive Evaluation of Materials by Infrared Thermography*. Springer-Verlag, London, (1993).

[3]   X.P.V. Maldague, *Theory and practice of infrared technology for nondestructive testing*. John Wiley & Sons, New York, (2001).

[4]   P. Vernotte, "Simultaneous Determination of Specific heat and Thermal Conductivity of Insulators", *R. Acad. Sci. URSS.* **204**, 563 (1937).

[5]   E. Hendler, R. Crosbie, and J.D. Hardy, "Measurement of heating the skin during exposure to infrared radiation", *J. Appl. Physiology* **12**, 177 (1958).

[6]   R.D. Cowan, "Proposed method of measuring thermal diffusivity at high temperatures", *J. Appl. Phys.* **32**, 1363 (1961).

[7]   W.J. Parker, R.J. Jenkins, C.P. Butler, and G.L. Abbott, "Flash method of determining thermal diffusivity, heat capacity, and thermal conductivity", *J. Appl. Phys.* **32**, 1679 (1961).

[8]   V. Vavilov, "Thermal NDT: historical milestones, state-of-the-art and trends", *QIRT. J.* **11**, 66 (2014).

[9]   C. Meola and G. M. Carlomagno, "Recent advances in the use of infrared

thermography", *Meas. Sci. Technol.* **15**, 27 (2004).

[10]   R. Mulaveesala and S. Tulition, "Theory of frequency modulated thermal wave imaging for nondestructive subsurface defect detection", *Appl. Phys. Lett.* **89**, 191913 (2006).

[11]   N. Tabatabaei and A. Mandelis, "Thermal-wave radar: A novel subsurface imaging modality with extended depth-resolution dynamic range", *Rev. Sci. Instrum.* **80**, 034902 (2009).

[12]   N Tabatabaei and A Mandelis, "Thermal Coherence Tomography Using Match Filter Binary Phase Coded Diffusion Waves", *Phys. Rev. Lett.* **107**, 165901 (2011).

[13]   W. Minkina and S. Dudzik, *Infrared Thermography: Errors and Uncertainties*. John Wiley & Sons, U.K., (2009).

[14]   J. D. Jackson, *Classical Electrodynamics*. 3rd edition, John Wiley & Sons, U.S.A., (1998).

[15]   C. Ibarra-Castanedo and X. P. V. Maldague, "Infrared Thermography", *in Handb. Tech. Diagn.*, H. Czichos, Ed. Springer, Berlin (2013).

[16]   A. Rogalski, "Infrared detectors: status and trends", *Prog. Quantum Electron.* **27**, 59 (2003).

[17]   R. Rogalski and K. Chrzanowski, "Infrard devices and techniques", *Opto-electronics Rev.* **10**, 111 (2002).

[18]   J. H. Lienhard IV and J.H. Lienhard V, *A Heat Transfer Textbook*. 3rd Edition, Phlogiston Press, U.S.A., (2006).

[19]   Y.A. Çengel, *Introduction to Thermodynamics and Heat Transfer*. McGraw-Hill, 2nd Ed., (2008).

[20]   J. Fourier, *Theorie Analytique de La Chaleur*. Chez Firmin Didot, père et fils,

Paris, (1822).

[21] H. S. Carslaw and J. C. Jaeger, *Conduction of Heat in Solids*. Oxford University Press, (1959).

[22] D.P. Almond and P.M. Patel, *Photothermal Science and Techniques*. Chapman & Hall, London, (1996).

[23] A. Salazar, "On thermal diffusivity", *Eur. J. Phys* **24**, 351 (2003).

[24] E. Marín, "Thermal Physics Concepts: The Role of the thermal Effusivity", *The Physics Teacher* **44**, 432 (2006).

[25] R.N. Bracewell, *The Fourier transform and its applications*. McGraw-Hill (2nd edition), New York (1986), p. 244.

[26] B. Zhang and R. E. Imhof, "Theoretical analysis of the surface thermal wave technique for measuring the thermal diffusivity of thin slabs", *Appl. Phys. A* **62**, 323 (1996).

[27] L. Fabbri and P. Fenici, "Three-dimensional photothermal radiometry for the determination of the thermal diffusivity of solids", *Rev. Sci. Instrum* **66**, 3593 (1995).

[28] FLIR SC7000 Series. State-of-the-art infrared technology for R&D / Science. http://www.flirmedia.com/MMC/THG/Brochures/RND_017/RND_017_US.pdf (2014)

[29] E. Marin and R. Ivanov, "LIA in a nut shell: How can trigonometry help to understand Lock-in Amplifier operation?", *Lat. Am. J. Phys. Educ.* **3**, 544 (2009).

[30] M. Langenkamp, W. Warta, and O. Breitenstein, *Lock-in thermography: basics and use for functional diagnostics of electronic components*. Springer Series in Advanced Microelectronics, Second Edition (2010), p. 41.

[31] J.-C.Krapez and G. Gardette, "Characterization of anisotropic materials by

steady-state and modulated thermal ellipsometry", *High Temp. High Press.* **30**, 567 (1998).

[32]   J.F. Bisson and D. Fournier, "Influence of diffraction on low thermal diffusivity measurements with infrared photothermal microscopy", *J. Appl. Phys.* **83**, 1036 (1998).

[33]   J.F. Bisson and D. Fournier, "The coupled influence of sample heating and diffraction on thermal diffusivity estimate with infrared photothermal microscopy", *J. Appl. Phys.* **84**, 38 (1998).

[34]   H.G. Walther and T. Kitzing, "Systematic errors of locally resolved photothermal radiometry measurements", *J. Appl. Phys.* **84**, 1163 (1998).

[35]   F. Cernuschi, A. Russo, L. Lorenzoni, and A. Figari, "In-plane thermal diffusivity evaluation by infrared thermography", *Rev. Sci. Instrum.* **72**, 3988 (2001).

[36]   S. Paoloni and D. Fournier, "Spectral dependence of signal distortions in spatially resolved photothermal radiometry", *J. Appl. Phys.* **92**, 5950 (2002).

[37]   S. Paoloni and D. Fournier, "Semi-empirical approach for the analysis of infrared photothermal microscopy", *J. Appl. Phys.* **92**, 5955 (2002).

[38]   C. Boué and D. Fournier, "New set-up to measure the thermal diffusivity with an infrared camera", *J. Phys. IV France* **125**, 101 (2005).

[39]   L. Perez and L. Autrique, "Robust determination of thermal diffusivity values from periodic heating data", *Inverse problems* **25**, 045011 (2009).

[40]   T. Ishizaki and H. Nagano, "Measurement of 3D thermal diffusivity distribution with lock-in thermography and application for high thermal conductivity CFRPs", *Infrared Phys. Technol.* **99**, 248 (2019).

[41]   C.S. Welch, D.M. Heath, and W.P. Winfree, "Remote measurement of in-plane diffusivity components in plates", *J. Appl. Phys.* **61**, 895 (1987).

[42] M. Oksanen, R. Scholz, and L. Fabbri, "On the longitudinal thermal diffusivity of SiC-based fibres", *J. Mat. Sci. Lett.* **16**, 1092 (1997).

[43] H. Kato, T. Baba, and M. Okaji, "Anisotropic thermal diffusivity measurements by a new laser-spot-heating technique", *Meas. Sci. Technol.* **12**, 2074 (2001).

[44] A. Wolf, P. Pohl, and R. Brendel, "Thermophysical analysis of thin films by lock-in thermography", *J. Appl. Phys.* **96**, 6306 (2004).

[45] C. Pradere, J.M. Goyhénèche, J.C. Batsale, S. Dilhaire, and R. Pailler, "Thermal diffusivity measurements on a single fiber with microscale diameter at very high temperature", *Int. J. Therm. Sci.* **45**, 443 (2006).

[46] A. Salazar, A. Mendioroz, and R. Fuente, "The strong influence of heat losses on the accurate measurement of thermal diffusivity using lock-in thermography", *Appl. Phys. Lett.* **95**, 121905 (2009).

[47] A. Mendioroz, R. Fuente-Dacal, E. Apiñaniz, and A. Salazar, "Thermal diffusivity measurements of thin plates and filaments using lock-in thermography", *Rev. Sci. Instrum.* **80**, 074904 (2009).

[48] A. Salazar, A. Mendioroz, R. Fuente, and R. Celorrio, "Accurate measurements of the thermal diffusivity of thin filaments by lock-in thermography", *J. Appl. Phys.* **107**, 043508 (2010).

[49] P.W. Nolte, T. Malvisalo, F. Wagner, and S. Schweizer, "Thermal diffusivity of metals determined by lock-in thermography", *QIRT J.* **14**, 218 (2017).

[50] A. Philipp, N.W. Pech-May, B.A.F. Kopera, A.M. Lechner, S. Rosenfeldt, and M. Retsch, "Direct measurement of the in-plane thermal diffusivity of semitransparent thin films by lock-in thermography: an extension of the slopes method", *Anal. Chem.* **91**, 8476 (2019).

[51] J. Hahn, T. Reid, and A. Marconnet, "Infrared microscopy enhanced Angström's method for thermal diffusivity of polymer monofilaments and films", *J. of Heat*

Transfer **141**, 081601 (2019).

[52] C.L. Choy, G.W. Yang, and Y.W. Wong, "Thermal diffusivity of polymer films by pulsed photothermal radiometry", *J. Polym. Sci. B: Polym. Phys.* **35**, 1621 (1997).

[53] P. Bison, F. Cernuschi, and S. Capelli, "A thermographic technique for the simultaneous estimation of in-plane and in-depth thermal diffusivities of TBCs", *Surface & Coating Technology* **205**, 3128 (2011).

[54] H. Dong, B. Zheng, and F. Chen, "Infrared sequence transformation technique for in situ measurement of thermal diffusivity and monitoring of thermal diffusion", *Infrared Phys. Technol.* **73**, 130 (2015).

[55] N. W. Pech-May, A. Mendioroz, and A. Salazar, "Simultaneous measurement of the in-plane and in-depth thermal diffusivity of solids using pulsed infrared thermography with focused illumination", *NDT&E Int.* **77**, 28 (2016).

[56] L. Gaverina, A. Sommier, J. L. Battaglia, J. C. Batsale, and C. Pradere, "Pulsed Flying Spot Elliptic method for the estimation of the thermal diffusivity field of orthotropic materials", *Int. J. Therm. Sci.* **125**, 142 (2018).

[57] A. Salazar, A. Oleaga, and A. Mendioroz, "How far and fast does heat propagate?", *Lat. Am. J. Phys. Educ.* **13**, 2307 (2019).

[58] Y.A. Çengel, *Heat Transfer: A practical Approach*. McGraw-Hill, Boston, (2003).

[59] Goodfellow catalogue. http://www.goodfellow.com

[60] Y.S. Touloukian, R.W. Powell, C.Y. Ho, and M.C. Nicolaou, *Thermal Diffusivity*. IFI/Plenum, New York (1973).

[61] M. Colom, A. Bedoya, A. Mendioroz, and A. Salazar, "Measuring the in-plane thermal diffusivity of moving samples using laser spot lock-in thermography", *Int. J. Therm. Sci* **151**, 106277 (2020).

[62]   A. Bedoya, J. González, J. Rodríguez-Aseguinolaza, A. Mendioroz, A. Sommier, J.C. Batsale, C. Pradere, and A. Salazar, "Measurement of in-plane thermal diffusivity of solids moving at constant velocity using laser spot infrared thermography", *Measurement* **134**, 519 (2019).

[63]   A. Bedoya, J. González, A. Mendioroz, C. Pradere, A. Sommier, J. C. Batsale, and A. Salazar, "Flying-spot thermography: measuring the in-plane (an)isotropic thermal diffusivity of large and complex parts", *Proceedings of SPIE* **11004J** (2019).

[64]   A. Salazar, L. Zamanillo, M. Colom, A. Mendioroz, U. Galietti, A. Sommier, J.C. Batsale, and C. Pradere, "Lock-in thermography on moving samples: amazing mismatch between amplitude and phase", *QIRT J.* **17**, 179 (2020).

[65]   L. Gaverina, J.C. Batsale, A. Sommier, and C. Pradere, "Pulsed flying spot with logarithmic parabolas method for the estimation of on-plane thermal diffusivity fields on heterogeneous and anisotropic materials", *J. Appl. Phys.* **121**, 115105 (2017).

[66]   A. Sommier, J. Malvaut, V. Delos, M. Romano, T. Bazire, J.C. Batsale, A. Salazar, A. Mendioroz, A. Oleaga, and C. Pradere, "Coupling Pulsed Flying Spot technique with robot automation for industrial thermal characterization of complex shape composite materials", *NDT&E Int.* **102**, 175 (2019).

[67]   L. Gaverina, M. Bensalem, A. Bedoya, J. González, A. Sommier, J.L. Battaglia, A. Salazar, A. Mendioroz, A. Oleaga, and J.C. Batsale and C. Pradere, "Constant Velocity Flying Spot for the estimation of in-plane thermal diffusivity on anisotropic materials", *Int. J. Therm. Sci.* **145**, 106000 (2019).

[68]   G. Paul, M. Chopkar, and P. K. Das I. Manna, "Techniqques for measuring the thermal conductivity of nanofluids: A review", *Renew. Sustain. Energy Rev.* **14**, 1913 (2010).

[69]   M. J. Assael, K. D. Antoniadis, and W. H. Wakeham, "Historical evolution of the

transient hot-wire technique", *Int. J. Thermophys.* **31**, 1051 (2010).

[70] M. Khayet and J. M. Ortiz de Zárate, "Application of the multi-current transient hot-wire technique for absolute measurements of the thermal conductivity of glycols", *Int. J. Thermophys.* **26**, 637 (2005).

[71] J. G. Webster and H. Eren, *Measurement, Instrumentation, and Sensors Handbook*. CRS Press (2018), p. 66.

[72] N. W. Pech, A. Oleaga, A. Mendioroz, A. J. Omella, R. Celorrio, and A. Salazar, "Vertical cracks characterization using lock-in thermography: I infinite cracks", *Meas. Sci. Technol.* **25**, 115601 (2014).

[73] M.L.V. Ramires, C.A. Nieto de Castro, Y. Nagasaka, A. Nagashima, M.J. Assael, and W. A. Wakeham, "Standard reference data for the thermal conductivity of water", *J. Phys. Chem. Ref. Data* **24**, 1377 (1995).

[74] H. Xie, J. Wang, T. Xi, Y. Liu, F. Ai, and Q. Wu, "Thermal conductivity enhancement of suspensions containing nanosized alumina particles", *J. Appl. Phys.* **91**, 4568 (2002).

[75] Y. Kadin and A.V. Rychahivskyy, "Modeling of surface cracks in rolling contact", *Mater. Sci. Eng. A.* **541**, 143 (2012).

[76] U. Netzelmann, G. Walle, A. Ehlen, S. Lugin, M. Finckbohner, and S. Bessert, "NDT of Railway Components Using Induction Thermography", *AIP Conf. Proc.* **1706**, 150001 (2016).

[77] B. Oswald-Tranta, "Induction thermography for surface crack detection and depth determination", *Appl. Sci.* **8**, 257 (2018).

[78] J. Peng, J. Bai, L. Feng, and Z. He, "The eddy current pulsed thermography detection of fatigue crack closure", *AIP Conf. Proc.* **2102**, 120002 (2018).

[79] Y. Fan, S. Dixon, R.S. Edwards, and X. Jian, "Ultrasonic wave propagation and interaction with surface defects on rail track crack", *NDT&E Int.* **40**, 471 (2007).

[80] I.Z. Abidin, G.Y. Tian, J. Wilson, S. Yang, and D. Almond, "Quantitative evaluation of angular defects by pulsed eddy current thermography", *NDT&E Int.* **43**, 537 (2010).

[81] N.W. Pech-May, A. Oleaga, A. Mendioroz, and A. Salazar, "Fast characterization of the width of vertical cracks using pulsed laser spot infrared thermography", *J. Nondestruct. Eval.* **35**, 22 (2016).

[82] J. González, A. Mendioroz, A. Sommier, J.C. Batsale, C. Pradere, and A. Salazar, "Fast sizing of the width of infinite vertical cracks using constant velocity Flying Spot Thermography", *NDT&E Int.* **103**, 166 (2019).

[83] J. Schlichting, Ch. Maierhofer, and M. Kreutzbruck, "Defect sizing by local excitation thermography", *QIRT J* **8**, 51 (2011).

[84] J. Schlichting, Ch. Maierhofer, and M. Kreutzbruck, "Crack sizing by laser excited thermography", *NDT&E Int.* **45**, 133 (2012).

[85] M. Streza, Y. Fedala, J.P. Roger, G. Tessier, and C. Boué, "Heat transfer modelling for surface crack depth evaluation", *Meas. Sci. Technol.* **24**, 045602 (2013).

[86] Y. Fedala, M. Streza, J.P. Roger, G. Tessier, and C. Boué, "Open crack depth sizing by laser stimulated infrared lock-in thermography", *J. Phys. D: Appl. Phys.* **47**, 465501 (2014).

[87] C. Bu, Q. Tang, Y. Liu, X. Jin, Z. Sun, and Z. Yan, "A theoretical study on vertical finite cracks detection using pulsed laser spot thermography (PLST)", *Infrared Phys. Technol.* **71**, 475 (2015).

[88] J. Qiu, C. Pei, H. Liu, and Z. Chen, "Quantitative evaluation of surface crack depth with laser spot thermography", *Int. J. Fatigue* **101**, 80 (2017).

[89] C. Boué and S. Holé, "Open crack depth sizing by multi-speed continuous laser stimulated lock-in thermography", *Meas. Sci. Technol.* **28**, 065901 (2017).

[90] A. Scalbi, R. Olmi, and G. Inglese, "Evaluation of fractures in a concrete slab by means of laser-spot thermography", *Int. J. Heat Mass Transf.* **141**, 282 (2019).

[91] T. Ishizaki, T. Igami, and H. Nagano, "Measurement of local thermal contact resistance with a periodic heating method using microscale lock-in thermography", *Rev. Sci. Instrum.* **91**, 064901 (2020).

[92] J. Qiu, C. Pei, Y. Yang, R. Wang, H. Liu, and Z. Chen, "Remote measurement and shape reconstruction of surface-breaking fatigue cracks by laser-line thermography", *Int. J. Fatigue* **142**, 105950 (2020).

[93] C. Boué and S. Holé, "Comparison between multi-frequency and multi-speed laser lock-in thermography methods for the evaluation of crack depths in metal", *QIRT* **17**, 223 (2020).

[94] T. Li, D.P. Almond, and D.A.S. Rees, "Crack imaging by scanning laser-line thermography and laser-spot thermography", *Meas. Sci. Technol.* **22**, 035701 (2011).

[95] T. Li, D.P. Almond, and D.A.S. Rees, "Crack imaging by scanning pulsed laser spot thermography", *NDT&E Int.* **44**, 216 (2011).